An examination of the use of the chemotherapy drug doxorubicin, gold nanoparticles, and radiation in combined cancer therapy.

by

Sarah Eaton
B.Sc., University of Victoria, 2019

A Thesis Submitted in Partial Fulfillment of the
Requirements for the Degree of

MASTER OF SCIENCE

in the Department of Physics and Astronomy

We acknowledge and respect the Lək̓ʷəŋən (Songhees and Esquimalt) Peoples on whose territory the university stands, and the Lək̓ʷəŋən and W̱SÁNEĆ Peoples whose historical relationships with the land continue to this day.

An examination of the use of the chemotherapy drug doxorubicin, gold nanoparticles, and radiation in combined cancer therapy.

by

Sarah Eaton
B.Sc., University of Victoria, 2019

Supervisory Committee

Dr. Devika Chithrani, Supervisor
(Department of Physics and Astronomy)

Dr. Wayne Beckham, Departmental Member
(Department Physics and Astronomy)

Abstract

The chemotherapy drug doxorubicin (DOX) is a widespread and effective treatment for many different types of cancer. However, it is known for causing significant and dangerous side effects due to high cardiotoxicity. Gold nanoparticles (GNPs) are a promising field of nanomedicine due to their stability, customizability, and radiosensitization properties as demonstrated using in vitro and mice models. They accumulate preferentially in tumours due to the enhanced permeability and retention effect. The combination of GNP mediated radiotherapy and DOX has the potential to deliver highly targeted and effective therapeutics while sparing surrounding healthy tissue.

This work used GNPs conjugated with PEG and RGD, DOX, and radiotherapy in combination to investigate possible synergistic cancer therapeutics. MDA-MB-231 cells were dosed for 48 hours with GNPs at a clinically relevant concentration of 7.5 μg/mL. DOX was dosed at the measured IC50 concentration of 144.4 nM for a 48 hour exposure. Radiation doses of 2 Gy and 5 Gy were used, as 2 Gy is commonly used for fractionated radiotherapy and recent clinical trials have also shown 5 Gy to be an effective fractionated radiation dose.

A cytotoxicity assay was conducted to determine the IC50 of DOX which was used as the dosing concentration for all other assays. Live cell images were taken to demonstrate the internalization of DOX and GNPs in the cells. To quantify if DOX affected the uptake of GNPs into the cells, a cellular uptake study was conducted. As previous research has indicated that DOX causes cell cycle arrest, a cell cycle assay was conducted. To assess the cytotoxicity and radiosensitization properties of GNPs and DOX, a cellular proliferation study and a clonogenic assay were conducted. Additionally, a DNA double strand break assay was conducted to assess the amount of DNA damage caused.

The cellular uptake study revealed that DOX caused an increase in GNP uptake, with $(1.27\pm0.16)\times10^6$ GNPs per cell when treated with DOX, and $(0.76\pm0.05)\times10^6$ GNPs per cell when untreated. DOX showed evidence of radiosensitization in the proliferation assay with the combination of DOX and radiation causing a (54±2)% reduction in cell growth when 2 Gy was administered, and a (69±8)% reduction in cell growth when 5 Gy was administered. However, this effect was not synergistic. In the other assays conducted, DOX caused cell cycle arrest, extensive DNA damage, and no clonogenic growth. It was concluded that DOX was inducing senescence at the given dose.

GNPs showed some radiosensitization in the proliferation assay at 2 Gy, with (24±2)% reduction in growth after 3 days in the 2 Gy GNP sampled compared to (15±2)% reduction in growth in the 2 Gy control sample. No other significant differences in growth due to

GNPs were seen in the proliferation assay. The clonogenic assay showed that 2 Gy radiation caused a (67±5)% decrease and 5 Gy caused a (97.9±0.6)% decrease in clonogenic survival of cells treated with radiation only when compared to the unirradiated control. The GNP incubated sample demonstrated some radiosensitivity in the clonogenic assay as it had a (78±3)% lower surviving fraction when irradiated with 2 Gy then the unirradiated control. The GNPs also showed toxicity in the unirradiated sample, with (30±11)% lower surviving fraction than the control in the clonogenic assay. A Bliss independence test found the GNPs and 2 Gy radiation to have independent effects. There was no significant difference between the GNP and control cells in the clonogenic assay when irradiated with 5 Gy. The DNA double strand break assay showed that 2 Gy radiation caused an increase in DNA damage foci from 2.0±0.2 to 5.1±0.5 foci per cell. No significant difference in foci was seen between the control and the GNP incubated cells.

While the results from this work did not demonstrate a conclusive benefit from the combined therapy of doxorubicin, GNPs, and radiation, the system is still of interest. Future experiments could be performed using a reduced doxorubicin concentration such as the IC20, to reduce the toxicity while still causing an effect. If a synergistic effect can be observed, it could be exploited to significantly reduce normal tissue toxicity in cancer patients while still delivering a lethal dose of chemotherapy and radiotherapy to the tumour.

Table of Contents

List of Tables

List of Figures

Abbreviations

BSA Bovine Serum Albumin

BSC Biosafety Cabinet

CDK Cyclin-Dependent Kinase

DLS Dynamic Light Scattering

DMEM Dulbecco's Modified Eagle Medium

DMSO Dimethyl Sulfoxide

DNA Deoxyribonucleic Acid

DOX Doxorubicin Hydrochloride

DSB Double Strand Break

EBRT External Beam Radiotherapy

EPR Enhanced Permeability and Retention

FBS Fetal Bovine Serum

FDA US Food and Drug Administration

GNP Gold Nanoparticle

HDR High Dose Rate

HR Homologous Recombination

IC50 50% Inhibitory Concentration

ICP-MS Inductively Coupled Plasma Mass Spectrometry

IMRT Intensity-modulated Radiotherapy

kV Kilovoltage

LDR Low Dose Rate

Linac Linear Accelerator

LL4 Four-parameter Log-Logistic Function

LNCaP Lymph Node Carcinoma of the Prostate

LNP-DOX Liposomal Doxorubicin Hydrochloride

LSPR Localized Surface Plasmon Resonance

MDA-MB-231 M.D. Anderson Metastatic Breast Cancer 231

MDR Multidrug Resistance

MV Megavoltage

NHEJ Non-Homologous End Joining

PBS Phosphate Buffered Saline

PE Plating Efficiency

PEG Polyethylene Glycol

PFA Paraformaldehyde

RME Receptor Mediated Endocytosis

ROS Reactive Oxygen Species

RPMI Roswell Park Memorial Institute 1640 Medium

SBRT Stereotactic Body Radiotherapy

SF Survival Fraction

SSB Single Strand Break

SSBR Single Strand Break Repair

TI Therapeutic Index

UV-Vis Ultraviolet-Visible

VMAT Volumetric Modulated Arc Therapy

Acknowledgements

Thank you to my supervisor, Dr. Devika Chithrani, for encouraging me to pursue grad school and for providing me with this opportunity. Thank you to my fellow lab members, Nolan Jackson and Daniel Cecchi, for your support in the lab.

To Jade Fischer and Olivia Masella, I'm glad I joined this program when I did, so I could meet you. You helped me survive the coursework, and kept me sane when I had to spend long hours in the lab. Thank you so much.

I would also like to acknowledge Karlee Zammit, for sticking by me since we started physics at UVic many years ago, for listening to my woes, and for taking me on afternoon walks around campus to make sure I got some sun.

I would like to thank my dear friends and former roommates, Kali Salmas and Emilie Villeneuve, for always being there to listen to me, and for trying very hard to convince me to use "Cancer is the fourth sign of the zodiac, represented by a crab." as my opening line in this thesis.

Finally, I am incredibly grateful to my family for their support throughout my academic endeavours. To my dad, Tim, and his partner Janie, for providing a sympathetic ear and supporting me from afar. To my beloved dog Emrys, and his brother Magic to whom I had to say goodbye too soon. To my mom, Eva, and her husband Paul, for uncountable dinners and for putting up with my Jeopardy obsession. And to everyone else who isn't named here, you know who you are. Thank you all so much, I couldn't have done it without you.

Section 1

Introduction

Cancer is not just one disease but a range of diseases in which cells undergo unchecked or abnormal growth. It can affect anyone regardless of age, race, gender, or socioeconomic status. Globally, approximately one in five people will develop cancer in their lifetime, and it is responsible for 16.8% of deaths [1]. It is the leading cause of death in Canada, where two in five Canadians will develop cancer in their lifetime and one in four will die from it [2]. While cancer can arise from spontaneous mutations, many cancers are strongly linked to specific causes, such as smoking and lung cancer or HPV and cervical cancer.

1.1 Current Cancer Treatments

Most cancer treatments fall into three categories: surgery, chemotherapy, and radiotherapy. Frequently, a combination of the three treatment modalities is used.

1.1.1 Radiotherapy

Radiotherapy is the use of ionizing radiation to reduce or eradicate tumours. Most radiotherapy today takes the form of external beam radiotherapy (EBRT) with high energy photons generated by a clinical linear accelerator (linac) [3]. Linear accelerators use a magnetron to accelerate electrons into a target (such as tungsten), where they produce Bremsstrahlung photons. The target can be removed if electrons are the desired treatment modality [4]. Radioactive sources may also be used to generate high energy photons, such as cobalt-60. In some cases, protons, or heavy ions such as carbon may be used instead of photons [5]. Models estimate that approximately 50% of cancer patients would benefit from radiotherapy in some form [6].

When it was first used, radiotherapy was limited in energy to kilovoltage (kV) X-rays, so it was only able to treat superficial tumours that were near the skin [7]. In the 1950s,

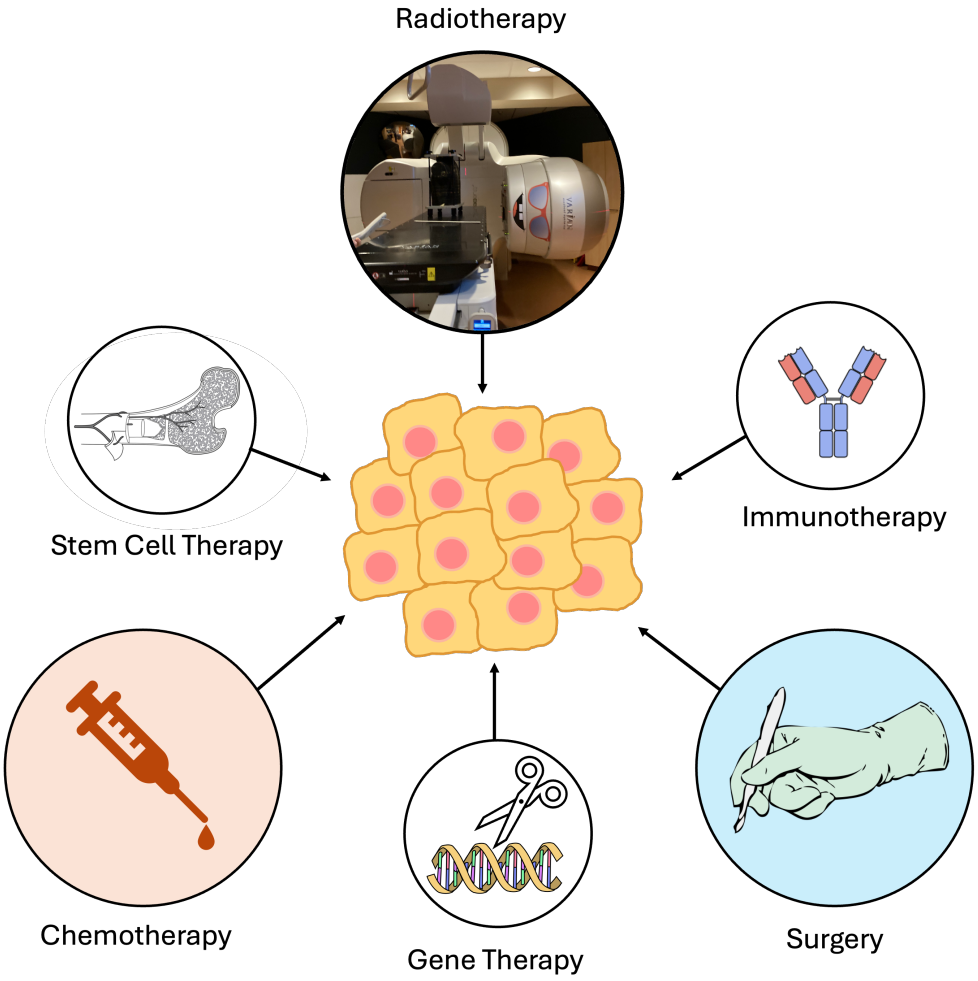

Figure 1.1: Common methods of cancer treatment. Cancer treatment is a multidisciplinary problem, and most patients will receive multiple forms of treatment.

cobalt-60 sources and linacs enabled the treatment of deep-seated tumours with megavoltage (MV) photons [8]. Since then, advances in technology have allowed for more sophisticated techniques and equipment, including the introduction of intensity-modulated radiotherapy (IMRT) in the late 1990s [9]. The invention of multileaf collimators was key to the development of IMRT as they shape the beam fluence. This allows for highly conformal dose delivery to tumours while sparing nearby organs, enhancing treatment efficacy and minimizing side effects [10].

Volumetric modulated arc therapy (VMAT) further optimized treatment by combining fluence shaping with continuous adjustments in dose rate, gantry arcing, and couch motion [11, 12]. This reduced treatment times while maintaining the precise level of dose deliv-

ery. Stereotactic body radiotherapy (SBRT) uses image guidance, dose conformality, and hypofractionation to exploit radiobiological principles and provide more effective treatment [13]. High biological variability between patients necessitates the use of individualized treatment plans. [14].

Brachytherapy is a form of internal radiotherapy where radioactive sources are placed near or inside the tumour. It allows for high doses of radiation to be delivered directly to cancerous tissue while minimizing exposure to surrounding healthy tissue [15]. Low dose rate (LDR) brachytherapy involves placing sources inside the tumour that emit radiation at a low rate and may be left in place for days or even permanently. This method is often used with prostate cancer [16]. High dose rate (HDR) brachytherapy uses highly radioactive sources that enter the body through carefully placed catheters. They are left in place for a specifically calculated dwell time, on the order of minutes, and then removed. HDR is more common for cervical or breast cancer [17]. Both LDR and HDR brachytherapy may be combined with EBRT for optimal tumour control [18].

There is potential to enhance treatment outcomes further through better understanding of the tumour microenvironment and the varying radiosensitivities of different cell lines [19]. Additionally, enhanced tumour control and reduced side effects could be achieved by integrating radiotherapy with concomitant synergistic treatments such as chemotherapy [20], immunotherapy [21, 22], and nanomedicine [23].

1.1.2 Chemotherapy

Chemotherapy plays a pivotal role in cancer treatment, and is often used in conjunction with radiotherapy, surgery, or both to enhance therapeutic efficacy. While anti-cancer drugs may offer curative potential in specific cancers, chemotherapy primarily aims to reduce micrometastases and prevent further cancer spread when used as adjuvant therapy [24].

Chemotherapy is the administration of cytotoxic compounds, with treatment goals varying based on cancer type and therapeutic objectives. Drugs like docetaxel, bleomycin, doxorubicin, and cisplatin have demonstrated effectiveness in limiting cancer growth [25]. For combined chemotherapy and radiotherapy, the order of treatment depends on factors such as cancer type, stage, and treatment goals. Each patient's treatment plan is tailored to their specific needs, considering factors such as tumour characteristics, overall health, and treatment tolerance [26].

Chemotherapy poses several challenges, including issues related to biodistribution, limited tumour specificity, short plasma half-life, poor solubility and stability, and nonspecific

toxicity [27]. Overcoming these challenges requires innovative approaches to drug delivery and formulation to enhance tumour targeting while minimizing adverse effects on healthy tissues. Despite the complexities involved, ongoing research aims to address these challenges and improve the efficacy and safety of chemotherapy in cancer management.

1.1.3 Other Cancer Treatments

Surgery is used to remove solid tumours. Historically, it was the primary avenue of cancer treatment, but as chemotherapy and radiotherapy techniques have progressed they have rendered surgery unnecessary for many cancers. Chemotherapy and radiotherapy are less invasive, and can be just as effective if not more effective than surgery at treating many cancers [28]. Despite advances in other treatment modalities, surgery remains a highly effective and critical treatment, with approximately 60% of patients receiving surgery in the course of their treatment in the United States [29]. Globally, it is estimated that 80% of cancer cases will require surgery in some form, including preventative and palliative care [30].

Stem cell therapy in the form of a bone marrow transplant is typically used when treating leukemia, after high doses of total body radiation, to restore the patients ability to generate new blood cells and their immune system [31]. However stem cells are also being investigated for other promising treatments, such as modifying them to produce antitumour agents in situ [32].

Another evolving area of cancer treatments is immunotherapy. This takes advantage of the fact that the immune system is inherently capable of destroying cancer cells, it simply needs to recognize the cancerous cells as something that should be destroyed [33]. Personalized cancer vaccines are one of the promising avenues of treating cancer which have emerged from immunotherapy research [34].

Other treatments for cancer include thermal or microwave ablation, cryotherapy, hyperthermia, and others [35]. Recent breakthroughs in gene therapy have also opened that up as a promising avenue of cancer treatment [36, 37]. Given the numerous types of cancer and the unique ways in which both the disease and treatments can affect each patient, it is crucial to explore all potential options when considering cancer treatment strategies.

1.2 Treatment Challenges

Ideally, cancer treatment will achieve 100% tumour control and completely halt the division of cancerous cells. However, due to challenges in precisely targeting cancer therapies, this is

often not practically achievable, as the damage to healthy tissues in the patient could result in death or other unacceptable side effects. The therapeutic index (TI) is used to evaluate the balance between tumour control and the patients quality of life.

For radiotherapy, the therapeutic index is the ratio of tumour control probability to the probability of normal tissue damage or complications. This assessment considers not only acute side effects but also long-term damage and patient quality of life [38]. Physicians set an upper tolerance for complications for a given treatment, which limits the achievable tumour response. With chemotherapy the therapeutic index is defined more explicitly as the ratio,

$$TI = \frac{TD_{50}}{ED_{50}} \tag{1.1}$$

where TD_{50} is the dose at which 50% of the population experiences a toxic effect, and ED_{50} is the dose at which 50% of the population experiences a therapeutic effect [39]. Much research in cancer therapy focuses on finding treatments or combinations of treatments that increase the therapeutic index or ratio.

1.2.1 Radiotherapy Challenges

Radiotherapy is more targeted than chemotherapy, but in most cases there is still a significant radiation dose delivered to healthy tissue. There are many strategies to improve radiotherapy outcomes, most of which focus on providing treatment which is highly localized on the tumour, to reduce the dose to normal tissue as much as possible. Side effects from radiotherapy may be immediate, or may occur years later. These side effects can also include secondary cancers caused by the treatment itself, as high doses of radiation to normal tissue are a known cause of cancer [40]. The side effects associated with radiotherapy can vary in severity and timing, depending on factors such as the tumour site, the organs involved, and the specific treatment regimen [41]. Understanding these potential side effects is crucial for optimizing patient care and improving quality of life post-treatment.

Prostate cancer treatment with radiotherapy can lead to side effects such as incontinence, cystitis, diarrhea, erectile dysfunction, and proctitis [42]. Similarly, in cervical cancer, where radiotherapy is often used concurrently with chemotherapy, side effects can occur in organs at risk like the bladder, rectum, and small intestine [20]. These side effects can manifest as gastrointestinal issues, urinary problems, and gynaecological complications [43].

With breast cancer, surgery is a frontline treatment and many patients undergo a mastectomy or lumpectomy. In both cases radiotherapy is often used as an adjuvant therapy, to prevent reoccurrence [44]. Given the proximity of the breast to the lung, pulmonary

complications such as pneumonitis and lung fibrosis can develop after radiotherapy [45]. Additionally, lymphoedema (swelling in the arm) [46], and brachial plexus neuropathy occur frequently, which can impair arm mobility and significantly impact quality of life [47]. Breast radiation can also contribute to late effects of cardiotoxicity, which can compound upon damage caused by concurrent chemotherapy such as doxorubicin [48].

Minimizing normal tissue toxicity while optimizing cancer cell kill is a key focus in improving treatment outcomes and enhancing the quality of life for patients undergoing radiotherapy. Continued research and innovation in radiotherapy techniques, along with a multidisciplinary approach to cancer care, are essential for further refining treatment strategies and maximizing the benefits of radiotherapy while minimizing its potential side effects.

1.2.2 Chemotherapy Challenges

Chemotherapy penetrates the whole body, and causes damage to healthy tissue just as much as to cancerous tissue. Chemotherapeutic drugs cause many unwanted side effects. The most reported are fatigue, loss of appetite, and diarrhea [49]. Other common side effects are hair loss, nausea and vomiting, dry mouth, and constipation [50]. A major focus of chemotherapy research is to determine methods of targeted delivery of drugs to cancerous cells, in the hopes of reducing the normal tissue complications.

Another significant challenge with chemotherapy is multidrug resistance (MDR). MDR is responsible for over 90% of deaths in patients receiving chemotherapy drugs [51]. Prolonged use of chemotherapeutics can lead to the development of drug resistance in cancer cells, reducing their effectiveness over time, however it may have a genetic component as well [52, 53]. This is a common challenge in cancer treatment and may require adjustments to the treatment regimen or the addition of other drugs to overcome. Current research is focused on understanding the causes of MDR and preventing it from developing [54, 55].

1.2.3 Other Treatment Challenges

If surgery fails to remove the whole tumour it can cause the remaining cancerous cells to spread through the body and metastasize [56]. Surgical treatment can involve long and difficult recovery, and it can result in other outcomes not directly related to cancer such as stroke, infection, or bleeding, and can lead to long and expensive hospital stays for patients [57–60]. Immunotherapy can cause a wide range of side effects depending on the treatment, including cardiotoxicity, arrhythmia, thyroid dysfunction, and dermatological toxicities [61]. All cancer therapies come with a wide range of side effects, creating an extensive list of

potential complications. While many effective cancer treatments exist, contemporary cancer research often focuses on reducing these side effects.

1.3 Radiobiology

1.3.1 The Five R's of Radiobiology

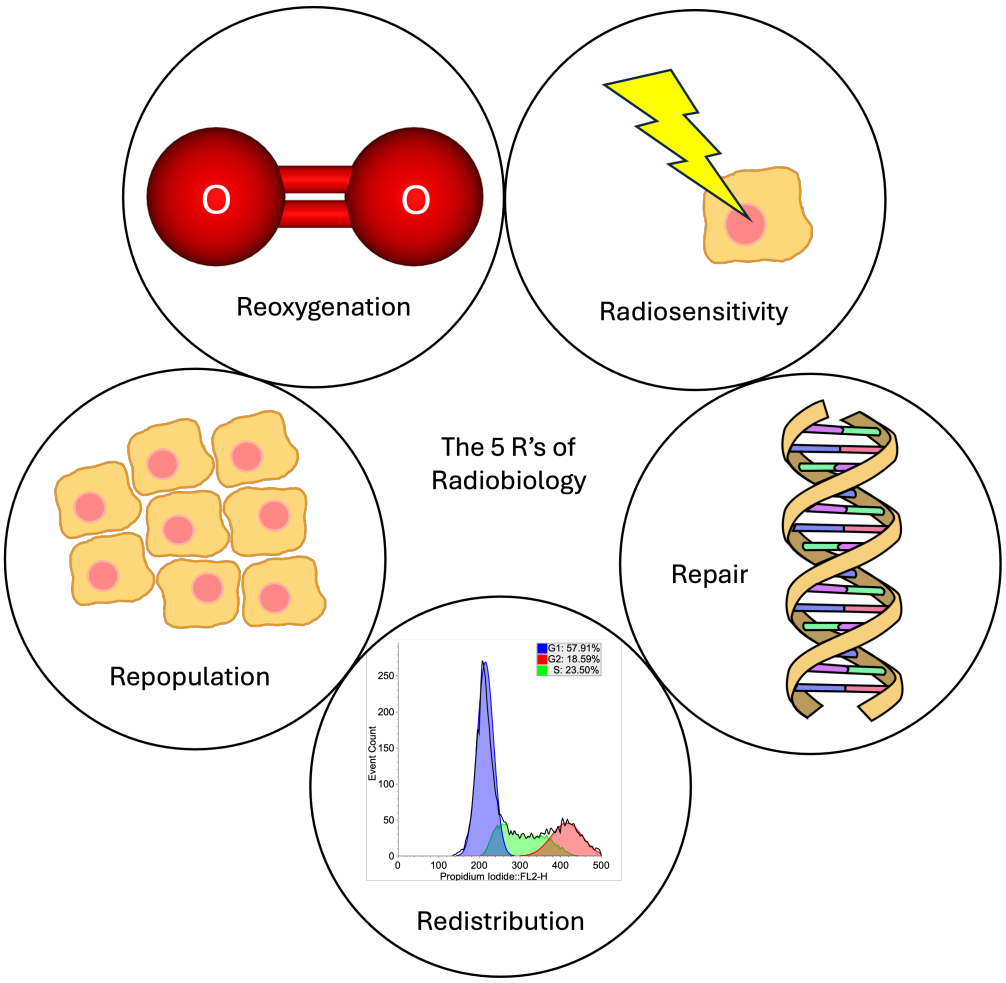

Figure 1.2: The five R's of radiobiology. These are the key principles that govern how cancer responds to radiation and they are used to guide the design of radiotherapy treatment.

The 5 R's of radiobiology are essential principles that describe the biological responses of cells and tissues to ionizing radiation [62]. Originally proposed as an explanation for the tissue sparing effects of fractionated radiotherapy [63], these principles help in understanding how radiation therapy can be optimized to treat cancer effectively while minimizing damage to normal tissues. They guide the design and implementation of radiotherapy protocols,

aiming to maximize the destruction of cancer cells while preserving the function of normal tissues.

Repair Cells have the ability to repair sub-lethal damage caused by radiation. Normal tissue is usually able to repair itself more quickly than cancerous tissue [64]. Fractionated doses of radiation allow normal cells time to repair, limiting normal tissue toxicity while the cancer cells stay in a damaged, vulnerable state.

Redistribution Cells move through different phases of the cell cycle, and their sensitivity to radiation varies with these phases (See Section 1.3.2). Cells are most radiosensitive during the G2 and M phases and most radioresistant during the S phase [65]. A dose of radiotherapy typically results in the cells in the radiosensitive phases dying off, leaving the remaining cells in the radioresistant phases of the cell cycle. Increasing time between fractions of radiation treatment allows the cells to redistribute in the cell cycle, putting more cells in the radiosensitive phases for the next treatment.

Repopulation After radiation damage, both normal and cancerous cells will proliferate to replace those that were killed. Sometimes, tumour cells can repopulate faster than normal cells. Additionally, repopulating tumour cells may be more radioresistant [66]. The timing and dosing of radiation must be carefully planned to control the repopulation of tumour cells while allowing sufficient recovery of normal tissues.

Reoxygenation Oxygen is essential to radiotherapy through the production of reactive oxygen species which can cause lethal damage. Tumours that are hypoxic (low oxygen) are more resistant to radiation [67]. After an initial radiation dose kills oxygenated cells, previously hypoxic cells can become oxygenated and thus more sensitive to subsequent doses. Fractionated radiotherapy allows for reoxygenation of hypoxic tumour areas, improving the overall effectiveness of the treatment.

Radiosensitivity The inherent sensitivity of cells to radiation varies [62]. Factors influencing radiosensitivity include the type of cell, the phase of the cell cycle, and the presence of oxygen. Understanding the radiosensitivity of different tissues helps in tailoring the treatment plan to maximize damage to cancer cells while minimizing harm to normal cells.

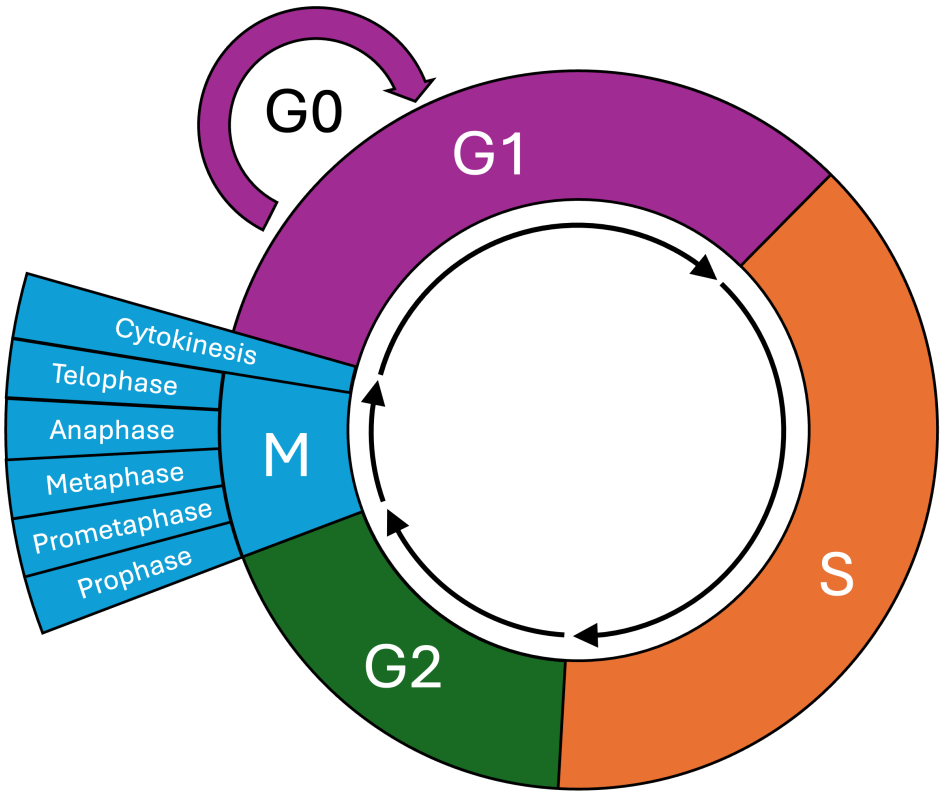

Figure 1.3: The life cycle of a eukaryotic cell.

1.3.2 The Eukaryotic Cell Cycle

The cell cycle is a tightly regulated process that governs the proliferation and division of normal cells. It ensures that cells duplicate accurately and distribute their genetic material evenly to daughter cells. There are four main phases to the cell cycle, G1, S, and G2, which are collectively called the interphase, and mitosis or the M phase. Progress through the cell cycle is regulated by cyclin-dependent kinases (CDKs), which phosphorylate other proteins required for cells to proceed through the cell cycle checkpoints [68].

G1, or gap 1 phase, is the first growth phase of the cell. During this phase the cell is metabolically active and grows in size while performing its regular functions. It also increases its supply of proteins and organelles in preparation for the next phase. Prior to entering the S phase, the cell goes through the G1/S checkpoint, which is intended to prevent cells containing DNA damage from proceeding to S phase. The G1/S checkpoint is activated by the p53 and p21 proteins. A cell that fails the G1/S checkpoint can be arrested in the G1 phase until DNA damage is repaired. If the cell is arrested in G1 due to a lack of extracellular growth factors, it may enter G0 or resting phase and become quiescent. Cells in G0 are still

viable, and can resume proliferating in the presence of sufficient growth factors [69].

If the cell passes through the G1/S checkpoint, it is committed to dividing and enters the synthesis or S phase [70]. This is typically the longest phase of the cell cycle, during which the cell duplicates all of its DNA in preparation for mitosis. During S phase, the cell monitors the DNA replication process, and any issues can trigger the S phase checkpoint, which slows the DNA replication process and extends S phase until the issue is resolved. This checkpoint is regulated by the proteins ATM, CHK1, and CHK2 [71], and can also be influenced by the BRCA1 and BRCA2 proteins [72].

After duplicating its DNA, the cell leaves S phase and enters the second gap phase, G2. It now contains two identical sets of chromosomes. G2 phase consists of rapid growth and protein synthesis. There are two G2 phase checkpoints. The early G2 checkpoint ensures that all DNA has been replicated. Failure of the early G2 checkpoint will arrest the cell in the G2 phase until DNA replication is finished. The late G2 checkpoint is the final check for DNA damage prior to mitosis [73]. Both G2 checkpoints are activated by a similar mechanism which involves the proteins ATM or ATR, CHK1/2, and CDC25A/C [72].

Finally, the cell undergoes division into two daughter cells during the M phase, mitosis. The M phase consists of several stages: prophase, prometaphase, metaphase, anaphase, and telophase, culminating in cytokinesis where the cytoplasm is divided into two daughter cells. During prophase, chromosomes condense, the nucleus breaks down, and the mitotic spindle begins to form. Prometaphase is marked by the fragmentation of the nuclear envelope, allowing microtubules to attach to chromosomes via their kinetochores. In metaphase the chromosomes have lined up in the middle of the cell and the centrosomes are at opposite poles. During anaphase, the sister chromatids separate and the cell elongates. Telophase sees the reformation of nuclear membranes, with chromosomes de-condensing to form two nuclei. Cytokinesis completes the process, splitting the cytoplasm into two daughter cells [74]. Understanding of the G2 and M phases is key for radiotherapy, as this is when cells are the most radiosensitive [65].

Many cancer cells have mutations in the p53, p21, or BRCA genes [75], which enable them to pass the G1/S and S phase checkpoints despite the presence of possible DNA damage. This enables cancer cells to proliferate rapidly when other healthy cells would have been halted in the cell cycle, and also to pass on genetic mutations. Accumulation of genetic defects compromises cell cycle regulation, preventing proper cell cycle exit and initiation of apoptosis. This continuous cell division and accumulation of genetic alterations contributes to tumour growth and survival, highlighting the importance of understanding and targeting cell cycle pathways in cancer therapy.

1.3.3 DNA Damage and Repair

DNA damage is a key focus of radiotherapy, because every time there is a break in a DNA strand, the cell must repair it in order to function properly. The more breaks there are, the more likely it is that the cell will repair the break incorrectly or fail to repair it altogether, and cause a catastrophic failure resulting in cell death.

Ionizing radiation can cause DNA damage directly by striking the DNA strands and breaking the bonds [76]. However, given the small volume that the DNA takes up relative to the total volume of the cell [77], the fraction of the radiation beam interacting directly with DNA is very small. It is more likely that the radiotherapy deposits energy into the cytoplasm of the cell, which is mostly water, and generates free electrons and reactive oxygen species which then react with DNA and cause damage [78]. Cells have evolved several DNA repair pathways to maintain genomic integrity and ensure cell survival in the face of DNA damage. These pathways can be broadly categorized into mechanisms that repair base damage, single-strand breaks (SSBs) and double-strand breaks (DSBs).

DNA base lesions are any number of chemical modifications to the base of a nucleotide, and are the most common type of genomic damage [79]. They can be repaired through direct lesion reversal or base excision repair [80]. Single strand breaks are the next most common type of damage. They are related to base lesions but typically involve a missing section of one strand of the DNA. The single strand break repair (SSBR) process is closely linked to base excision repair [81]. Another repair pathway, mismatch repair, corrects base-base mismatches and insertion-deletion loops that escape proofreading during DNA replication.

Double strand breaks, where both strands of DNA are damaged at the same spot, are the rarest but the most deadly type of DNA damage [82]. DSBs can be repaired by non-homologous end joining (NHEJ) or homologous recombination (HR). NHEJ simply joins the two broken ends together again [83]. It often results in a small portion of DNA missing from the repaired strand. HR uses a similar or identical undamaged DNA as a template, which is replicated to complete the repair.

When a DSB occurs, it triggers a complex cellular response to detect and repair the damage. One of the earliest events in this response is the phosphorylation of the histone protein H2AX, after which it is called γH2AX. After radiation exposure, this phosphorylation is primarily carried out by the ataxia telangiectasia mutated (ATM) protein. In humans, ATM is recruited to the DSB by a complex of three proteins: MRE11, RAD50, and NBS1 (collectively known as MRN). Once phosphorylated, γH2AX spreads along the chromatin over a large region surrounding the DSB, forming what are known as γH2AX foci. These

foci are a platform for the recruitment of various DNA repair proteins and help to activate DNA repair pathways and cell cycle checkpoints [84].

Another crucial regulator of the DNA DSB repair mechanism is p53-binding protein 1 (53BP1). This protein has multiple functions, one of which is to direct DSB repair via NHEJ [85]. Like γH2AX, the recruitment of 53BP1 can be tracked by the foci that form at sites of damaged chromatin. 53BP1 can be recruited independently of γH2AX, but it can also be recruited by the γH2AX platform, causing both foci to localize together [86].

1.4 Gold Nanoparticles

Gold nanoparticles (GNPs) have been studied for a number of different medical uses, including as a vehicle for drug delivery and as a contrast agent for medical imaging [87]. This work will focus on the use of GNPs as a radiosensitizer.

1.4.1 Characteristics of Gold Nanoparticles

GNPs exhibit highly customizable behavior, making them effective platforms for a range of treatments. Many studies have investigated gold nanoparticle systems of different size, shape, and surface chemistry [88]. Various gold-based nanotherapeutic systems, such as spherical GNPs, gold nanorods, gold nanoshells, gold nanoclusters, and GNP-incorporated liposomal nanoparticles, offer unique advantages and functionalities. Spherical GNPs are particularly favoured for their ease of production, and modifiable surface chemistry.

Gold nanoparticles exhibit a phenomenon called localized surface plasmon resonance (LSPR). This phenomenon occurs because the nanoparticles are similar in size or smaller than the wavelength of the light incident upon them. The cloud of electrons around the GNP resonates with the frequency of the incoming photons, and this causes a band of absorption in the electromagnetic spectrum. LSPR is affected by the size, shape, charge, and surface composition of the nanoparticles, as well as other factors like the temperature and pressure at which they are stored [89]. It is also responsible for the distinct range of colours taken on by gold nanoparticle solutions, with small gold nanoparticles appearing red and the colour shifting through purple and becoming blue as the size of the GNPs increases [90].

Chithrani, et al. showed that undecorated, spherical GNPs have highest cellular uptake when 50 nm in size [91]. However further studies showed that after functionalization with PEG and RGD, higher uptake was found with 14 nm diameter GNPs [92]. GNPs enter the cell through receptor-meditated endocytosis (RME). This process is also dependent on the size, shape, and surface chemistry of the GNPs [93].

The cytotoxicity and biocompatibility of GNPs depend on factors like size, shape, and surface functionalization. Smaller nanoparticles may exhibit greater cytotoxicity due to increased interaction with biomolecules, but surface modification, such as PEGylation, can mitigate adverse effects. Additionally, the shape of GNPs influences their biocompatibility, with nanospheres generally considered safer than nanorods [94].

1.4.2 Surface Ligands

Nanoparticles functionalized with PEG (polyethylene glycol) and RGD (Arg-Gly-Asp) serve a crucial role in various biomedical applications, particularly in targeted drug delivery systems. The functionalization of nanoparticles with PEG and RGD offers several advantages, such as improved stability, targeted delivery, and increased therapeutic efficacy.

PEGylation, the process of attaching PEG chains to the surface of nanoparticles, enhances their stability in biological environments because PEG acts as a steric barrier, preventing non-specific interactions with proteins and other biomolecules [95, 96]. This reduces the likelihood of triggering an immune response and prolongs circulation time in the bloodstream [97]. The length of the PEG molecules and the density at which they are attached to the nanoparticles can affect the uptake and toxicity of the PEGylated system [98].

The incorporation of RGD ligands onto the surface of nanoparticles enables specific targeting of cancer cells and tissues that overexpress integrin receptors, such as $\alpha_v\beta_3$ and $\alpha_v\beta_5$ [99]. The RGD motif binds selectively to these receptors, facilitating the internalization of nanoparticles into cancer cells while minimizing uptake by healthy cells. This targeted approach enhances the efficacy of drug delivery while reducing off-target effects and minimizing systemic toxicity. While the benefits of RGD have been confirmed extensively in vitro, the same benefits are not always seen in vivo [100].

The selective accumulation of nanoparticles in tumour tissues enhances the efficacy of anticancer drugs while minimizing their exposure to healthy tissues, thereby reducing side effects and improving patient outcomes. By combining PEGylation with RGD targeting, nanoparticle-based drug delivery systems can achieve higher drug concentrations at the site of action, leading to improved therapeutic outcomes [101]. Overall, the functionalization of nanoparticles with PEG and RGD represents a versatile strategy for designing targeted drug delivery systems with enhanced stability, biocompatibility, and therapeutic efficacy, holding great promise for the treatment of various diseases, particularly cancer.

1.4.3 Radiotherapy Applications of Gold Nanoparticles

Gold nanoparticles (GNPs) are a promising radiosensitizer [102–104]. One of the first studies demonstrating GNP radiosensitization was done by Hainfeld, et al. using 1.9 nm diameter GNPs in mice [105]. Due to their high atomic number (Z=79), gold atoms have a high interaction cross section with X-rays [106] and other forms of ionizing radiation. Gold also has an increased photoelectric absorption at low energies (E), as the probability of photoelectric interaction is proportional to $(Z/E)^3$. The increased photoelectric effect results in a surge of free electrons which generate reactive oxygen species (ROS) in the cell [107, 108]. These secondary particles and ROS cause significant DNA damage in cancer cells, improving the effectiveness of the radiation treatment. This allows for higher radiation doses to be delivered to the tumour while sparing surrounding healthy tissue.

Continued research efforts are focused on refining GNP based approaches to radiation therapy, with the ultimate goal of achieving clinically relevant outcomes. Optimizing GNP properties, such as size, shape, and surface modification, will be critical in realizing the full potential of GNP mediated radiation dose enhancement in clinical practice [109].

1.5 Doxorubicin

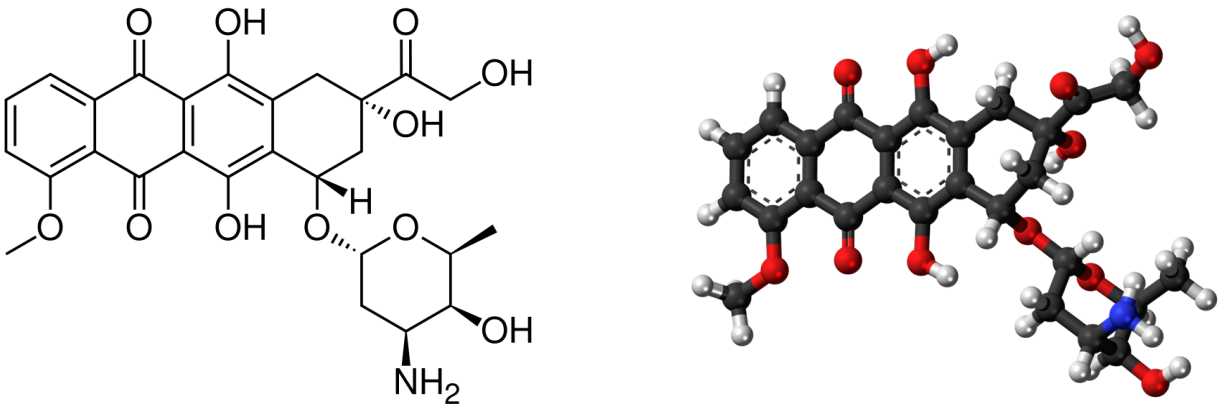

Figure 1.4: The chemical structure of doxorubicin. (Source: Wikimedia Commons in the public domain. Left image. Right image.)

Doxorubicin hydrochloride (DOX, sold under brand name Adriamycin®) and PEGylated liposomal doxorubicin (LNP-DOX, sold under brand names Doxil® or Caelyx®) is used to treat a wide variety of cancers and is commonly used to treat breast cancer. It is an effective form of chemotherapy but has a high level of normal tissue toxicity, particularly in cardiac

tissue [110]. Due to the severity of the side effects and the bright red colour of the drug, it is known colloquially by the name "red devil".

Doxorubicin is derived from the bacterium streptomyces peucetius. The same bacterium is used to produce daunorubicin, a distinct but related chemotherapy drug. Doxorubicin belongs to a family of drugs known as anthracyclines. It was discovered in the 1960's and approved for clinical use in 1974 by the US Food and Drug Administration (FDA) [111].

One of the major limiting side effects of doxorubicin is its potential for causing cardiotoxicity, which can lead to irreversible heart damage and congestive heart failure. The risk is dose-dependent, with higher cumulative doses increasing the risk [112]. Doxorubicin can also cause significant myelosuppression, leading to decreased levels of white blood cells, red blood cells, and platelets. This increases the risk of infections, anemia, and bleeding. Other side effects include nausea, vomiting, alopecia (hair loss), mucositis (inflammation of the intestinal lining), and fatigue [113].

1.5.1 Mechanisms of Action

Doxorubicin works by intercalating DNA, which means it inserts itself between DNA bases, disrupting the DNA structure. It also inhibits the enzyme topoisomerase II, which is essential for DNA replication and transcription [114]. As a result, doxorubicin prevents the proliferation of cancer cells and induces apoptosis (programmed cell death).

Its anticancer molecular action is complex and includes, among others: inhibition of topoisomerases I and II, formation of DNA adducts and free radicals, interaction with membrane proteins, histone eviction and ceramide overproduction [115]. Studies have demonstrated that doxorubicin can induce cell cycle arrest in the G0/G1 phase [116], the S phase [117], and the G2/M phase [116–118]. Additionally, anthracyclines including doxorubicin have been shown to increase the levels of polyunsaturated fatty acids in cells [119]. The mechanism of action may depend on the concentration of the drug, but at typical dosing concentrations the primary mechanism of action is via topoisomerase II inhibition [120].

1.6 Scope of this Thesis

Given the radiosensitization properties of GNPs and the anticancer properties of doxorubicin, these treatments may have a synergistic effect when used in combination. If so, the combined effect would be greater than the sum of the individual effects, which could lead to improved cancer therapeutics.

This work used doxorubicin, gold nanoparticles, and radiation. Breast cancer cells were

administered different combinations of the examined treatments, in order to ascertain the effectiveness and investigate possible synergy. To facilitate this, gold nanoparticle uptake, cellular proliferation, clonogenic survival, and DNA damage were quantified.

Section 2

Materials and Methods

2.1 Synthesis, Functionalization, and Characterization of Gold Nanoparticles

2.1.1 Synthesis

Gold nanoparticles (GNPs) of size ∼12 nm in diameter were prepared via a citrate reduction method adapted from the Turkevitch method [121, 122]. First, a 1% solution of chloroauric acid was produced by dissolving gold(III) chloride trihydrate ($HAuCl_4 \cdot 3H_2O$; Sigma Aldrich) in double distilled water. From this a 1 mM solution of gold was prepared by adding 28.82 mL of distilled water and 1.18 mL of the 1% chloroauric acid solution to an Erlenmeyer flask. The flask was covered with aluminum foil to reduce evaporation, and the solution was heated to boiling while stirring continuously. Once the solution was boiling, 1.2 mL of 5% sodium citrate tribasic dihydrate ($HOC(COONa)(CH_2COONa)_2 \cdot 2H_2O$; Sigma Aldrich) was added. The solution shifted rapidly from pale yellow to clear to dark purple. It boiled for a further 5 minutes until it was ruby red, and was brought to room temperature, all while stirring continuously (Figure 2.1).

2.1.2 Functionalization

The GNPs were functionalized using PEG and RGD. With the goal of moving to in vivo work in the future, PEG is used as it prolongs the circulation time of the nanoparticles in the body [97]. However PEG also reduces the uptake of nanoparticles into cells so a peptide containing RGD (Cys-Lys-Lys-Lys-Lys-Lys-Lys-Gly-Gly-Arg-Gly-Asp-Met-Phe-Gly) was also used to improve cell internalization [92].

To PEGylate the nanoparticles, PEG-thiol was added to the GNP solution at a ratio of 1 PEG molecule per 1 nm^2 of surface area on the GNPs [92]. The GNPs were assumed to be perfect spheres for the purpose of this calculation. The PEG and GNP mixture was

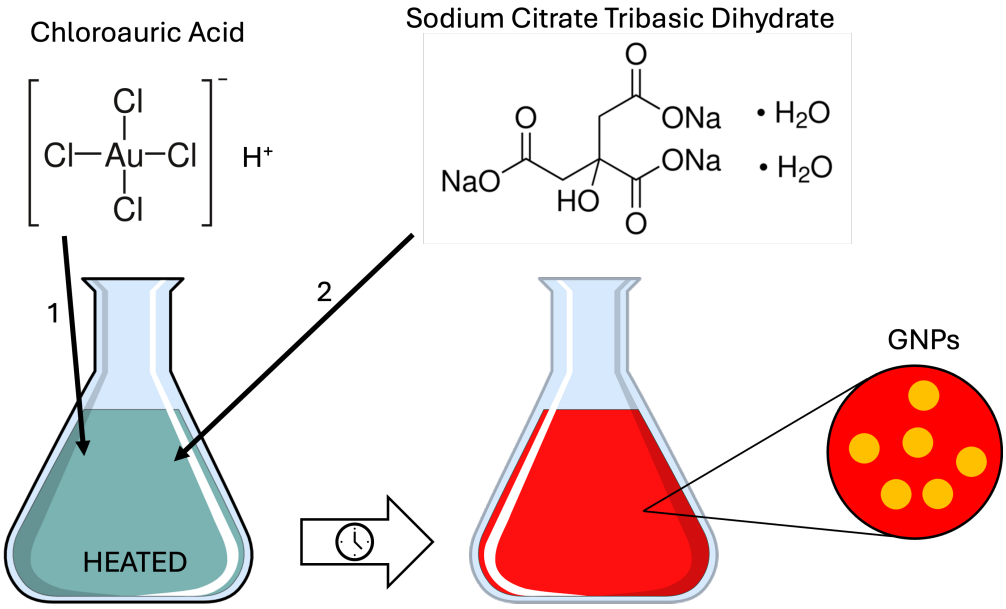

Figure 2.1: GNP Synthesis via the Turkevich method.

mixed thoroughly. Then RGD was added at a ratio of 1 RGD molecule per 2 PEG molecules [123]. The solution was mixed thoroughly and monitored for changes in colour or opacity. The characteristics of the PEG and RGD functionalized GNPs were verified as discussed in the next section. Except for live cell imaging, all experiments were conducted using GNPs functionalized with both PEG and RGD.

For live cell imaging, the GNPs were functionalized using a fluorescent marker so they could be imaged with a laser scanning confocal microscope. Half of the standard PEG molecules were replaced with PEG-thiol-Cy5. First the PEG was added to the GNPs as described above, except half as many were used. Then the PEG-thiol-Cy5 was added in equal proportion of molecules. It was mixed well, then RGD was added as before.

2.1.3 Characterization

UV-Vis Spectroscopy

To determine the size and concentration of the nanoparticles, ultraviolet-visible (UV-Vis) spectroscopy was conducted using a Perkin Elmer Lambda 365 UV/Vis Spectrophotometer using a wavelength range of 400-600 nm and a resolution of 0.05 nm. As the GNPs produced were very concentrated, they were diluted by half in distilled water before 1 mL was added to a quartz low-volume cuvette with a 1 cm path length. A cuvette of deionized water was used as the blank signal.

To determine the absorbance (A) of the sample, light is passed through the cuvette and the intensity of the transmitted light (I) is measured. The absorbance is then calculated according to the equation,

$$A = \log_{10}\left(\frac{I_0}{I}\right) \tag{2.1}$$

where I_0 is the intensity of the light transmitted through the reference material. The Beer-Lambert Law relates the absorbance to the concentration (C) of the sample according to,

$$A = \epsilon C L \tag{2.2}$$

where L is the path length through the sample and ϵ is the extinction coefficient. [124]

The absorbance of 450 nm incident light (A_{450}) and the peak absorbance were measured and used with a lookup table to determine the size of the nanoparticles. A second lookup table was used with A_{450} to get the extinction coefficient ϵ_{450}, from which the concentration was calculated using Equation 2.2 [125].

Dynamic Light Scattering

Dynamic light scattering (DLS) was used to measure the hydrodynamic diameter of the nanoparticles. The hydrodynamic diameter is the diameter of a hypothetical hard sphere that diffuses with the same speed as the particle being measured. Nanoparticles may not be perfectly circular and they are often used with surface modifications (such as PEG and RGD for this work) which affect the particles' motion in solution as well as how they interact with proteins and cells in the body [126]. Because of this, the hydrodynamic diameter is an important characteristic to know when planning for in vivo work.

Particles in a solution exhibit random motion known as Brownian motion. Light scatters off of the randomly moving particles which introduce randomness to the phase of the scattered light. Time-dependent fluctuations in the intensity of the scattered light are measured by a fast photon counter [127]. The fluctuations are directly related to the rate of diffusion of the molecule through the solvent, which is related in turn to the particle's hydrodynamic diameter by the Stokes-Einstein equation,

$$D_t = \frac{Tk_B}{3\pi\nu d_H} \tag{2.3}$$

where D_t is the diffusion coefficient, T is the temperature, k_B is the Boltzmann constant, ν is the viscosity of the medium, and d_H is the hydrodynamic diameter [128].

DLS was performed using a 1 cm path length quartz cuvette in an Anton Paar LiteSizer 500 with a light source of wavelength 658 nm.

Zeta Potential

The zeta or electrokinetic potential of a nanoparticle in solution is the electric potential at the shear plane. A charged nanoparticle in solution will attract ions of the opposite charge, which form a layer on the surface known as the Stern layer. Past this layer, the electrostatic effects of the particle's surface charge decrease with distance, and a second layer of both same and opposite charged ions forms called the diffuse layer. When an electric field is applied to the solution, charged particles move towards the opposite electrode. The shear plane is a hypothetical plane within the diffuse layer which forms an interface between the moving particles and the surrounding solution during this process. The zeta potential is measured at this plane [127].

In nanoparticles, a high zeta potential is an indicator of stability, as the particles repel each other and are less likely to aggregate. It is also useful to confirm successful PEGylation, as the zeta potential will change in the presence of surface ligands. For this work, zeta potential was measured with electrophoretic light scattering using an Anton Paar LiteSizer 500 with an Anton Paar Omega cuvette.

2.2 In Vitro Cell Culture Experiments

2.2.1 Cell Lines and Materials

MDA-MB-231 (ATCC# HTB-26), a breast cancer cell line, was the primary cell line used. It was cultured in high glucose Dulbecco's Modified Eagle Medium (DMEM; Gibco) supplemented with 10% fetal bovine serum (FBS; Gibco), 1% penicillin and streptomycin (Gibco), and 4 mM GlutaMAX (Gibco). Additional experiments were conducted using LNCaP (ATCC# CRL-1740), a prostate cancer cell line. It was cultured in Roswell Park Memorial Institute 1640 Medium (RPMI; Gibco), supplemented with 10% FBS, 1% penicillin and streptomycin, and 2 mM GlutaMAX. Both cell lines were maintained in an incubator at 5% CO_2 and 37°C, and passaged as needed when they reached 80% confluency. For cell dissociation, 0.25% Trypsin-EDTA (Gibco) was used. Experiments using live cells were performed in a biosafety cabinet (BSC).

For the DNA double strand break assay, two different DNA repair markers were examined. For labelling γH2AX foci, Anti-phosphone-Histone H2A.X (Ser139; Sigma-Aldrich) was used

as the primary antibody and Donkey anti-Mouse IgG, Alexa Fluor 647 (Invitrogen) was used as the secondary antibody. For labelling 53BP1 foci, Phospho-53BP1 (Ser1778; Cell Signalling Technology) was the primary antibody and Donkey anti-Rabbit IgG, Alexa Fluor 488 (Invitrogen) was used as the secondary antibody.

Gold nanoparticles were prepared as previously discussed. Doxorubicin hydrochloride (DOX; Sigma-Aldrich) was dissolved in dimethyl sulfoxide (DMSO; Sigma-Aldrich), aliquoted, and kept frozen at -20°C. When required for dosing cells, one aliquot was thawed and further diluted in PBS before adding to cell media to make the desired concentration. Unused portions were discarded and not refrozen. When GNPs were used, all cell lines were dosed with GNPs at a clinically relevant concentration of 7.5 μg/mL of gold.

2.2.2 Dosing Concentration

To determine the 50% inhibitory concentration (IC50) of free DOX for the cell lines used, cells were seeded in all the wells of a 96-well, black, flat bottomed tissue culture plate (Costar®, Corning Inc.) except column 1. Enough cells were seeded that untreated cells would be 80% confluent after four days. During incubation periods, the plates were sealed with a breathable membrane (Breathe-Easy®, Sigma-Aldrich) to reduce evaporation. After waiting 24 hours for the cells to adhere, the cells were dosed with DOX at doses ranging from 50 μM to 1.9x10^{-}4 μM, with a dilution factor of 4 between each column (see Figure 2.2). Cells were incubated with the drug for 48 hours, at which point the drugged media was removed and replaced with fresh media. The cells were allowed to grow for a further 24 hours. The media and PBS was removed and replaced with 100 μL of 10% PrestoBlue™ Cell Viability Reagent (Invitrogen) in media which was incubated for one hour before the amount of fluorescence was measured with a Biotek Cytation 1 plate reader. Viable cells reduce the reaszurin compound in the PrestoBlue, and the resulting fluorescence correlates linearly to the number of viable cells.

The fluorescence was averaged down the columns to get the average fluorescence per condition. The blank wells are necessary as the PrestoBlue alone yields some fluorescence even without cells, and this value was subtracted from the other conditions as the background. The fluorescence of the dosed columns were divided by that of the untreated control column to calculate the relative growth. This was plotted against the drug concentration, and the resultant dose-response curve was fitted with the four-parameter log-logistic function (LL4,

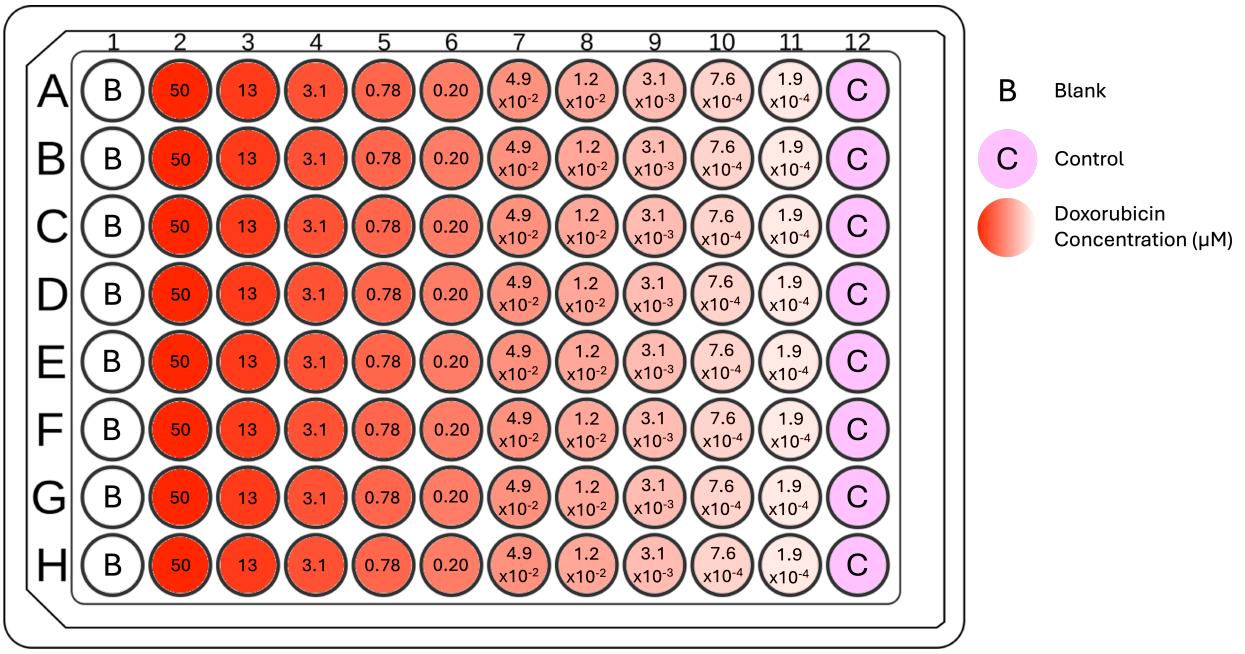

Figure 2.2: 96-well plate layout used for determining IC50.

Equation 2.4) using the `optimize.curve_fit` function from the Python package SciPy.

$$f(x) = c + \frac{d - c}{1 + \exp(b(\ln x - \ln a))} \tag{2.4}$$

The IC50 is the dose at which 50% of cells remained viable relative to the control, and was interpolated from the fitted curve [129]. For all further experiments, cells were dosed at the IC50 concentration of DOX for a 48 hour exposure.

2.2.3 Live Cell Imaging

Cells were seeded in 35 mm glass coverslip bottom dishes (MatTek) and incubated. After 24 hours they were dosed with DOX and GNPs functionalized with PEG-thiol-Cy5 and RGD. Cells were dosed for 48 hours. Four drops (2 drops/mL) of NucBlue™ Live Cell Stain ReadyProbes™ (Invitrogen) were added to the dish and it was incubated for a further 30 min before imaging on a laser scanning confocal microscope (Zeiss). NucBlue uses Hoechst 33342 to stain cell nuclei.

2.2.4 Cellular Uptake

Cells were plated in 6-well cell culture plates (CELLSTAR®, Greiner Bio-One) and incubated for 24 hours so the cells could adhere. After 24 hours, they were dosed with GNPs alone or DOX and GNPs according to Figure 2.3. Each condition was seeded in triplicate. Cells were incubated with the dosed media for 48 hours, then the media was removed. Each well was washed with PBS for five minutes, three times. Cells were dissociated from the plate by incubation with 250 μL trypsin for 5 minutes. 1 mL media was added to neutralize the trypsin and the samples were transferred to 1.5 mL microtubes. 100 μL was removed from each sample and the cell concentration was calculated using a hemocytometer. Samples were refrigerated until the day before data collection.

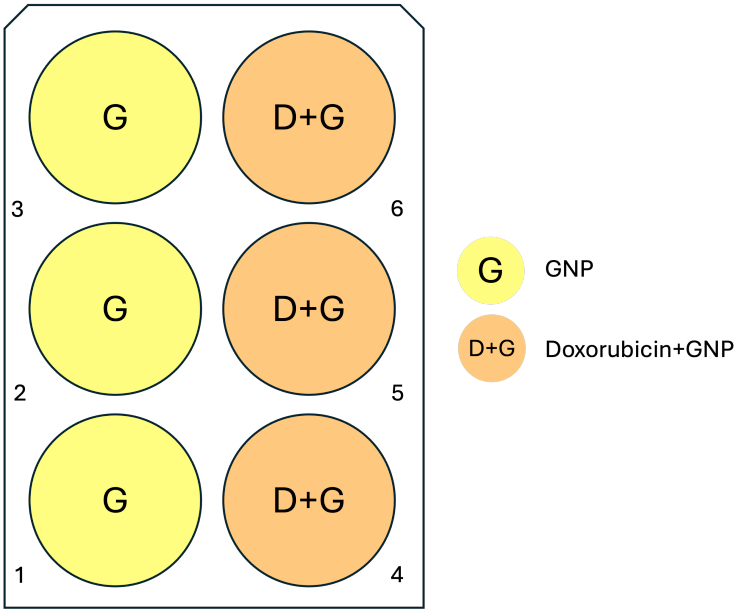

Figure 2.3: 6-well plate layout used for cellular uptake of GNPs.

To measure the gold in each sample, a portion of each sample was transferred to a glass test tube. The full sample was not used as the amount of gold would have been too high and it would saturate the detector. Samples were first mixed with a micropipette as they had settled after sitting in the fridge for a few days, and then a volume between 100-500 μL was transferred to the test tube in order to have 50,000-100,000 cells in the test tube. To reduce evaporation, a plastic cap was added to each tube. Tubes were placed in mineral oil to improve heat distribution and heated to 90°C on a hot plate in a fume hood. 250 μL of aqua regia was added to each sample, and they were maintained at 90°C for 30 min. Then 100 μL of hydrogen peroxide was added to each and they were maintained at 90°C for

another 30 min. Samples were transferred to 15 mL centrifuge tubes, and the glass tubes were washed down with 1 mL distilled water which was also added to the centrifuge tubes. Distilled water was added to bring the volume up to 10 mL. The concentration of gold in each sample was measured using Inductively Coupled Plasma Mass Spectrometry (ICP-MS).

To compute the number of GNPs in each cell, first the number of gold atoms per GNP, N, was computed. Gold has a face-centered cubic crystal structure with a lattice constant of a=0.4065 nm and the GNPs are assumed to be perfectly spherical with radius r, so N is given by,

$$N = \frac{16\pi r^3}{3a^3} \tag{2.5}$$

Knowing this, the gold concentration measured using ICP-MS, X (μg/L), can be converted into GNPs per mL, U, according to,

$$U = \frac{X}{N}\left(\frac{1\text{ g}}{10^6\mu\text{g}}\right)\left(\frac{1\text{ L}}{10^3\text{ mL}}\right)\left(\frac{1\text{ mol}}{196.97\text{ g Au}}\right)\left(\frac{6.022\times10^{23}\text{ atoms}}{1\text{ mol}}\right) \tag{2.6}$$

A small volume of cells, V, was used for each sample, and then the final product was diluted to 10 mL. Accounting for this dilution, the GNPs per cell is given by,

$$\text{GNPs/cell} = \frac{U(10\text{ mL})}{CV} \tag{2.7}$$

where C is the cell concentration calculated before processing samples for ICP-MS.

2.2.5 Cell Cycle

Cells were seeded in 6-well plates, allowed to adhere for 24 hr, then dosed with DOX and GNPs according to Figure 2.4. After dosing for 48 hours, media was removed and the cells were washed with PBS. To dissociate the cells from the well bottoms, they were incubated with 250 μL of trypsin until the cells had released. 1 mL of fresh media was added to each well to neutralize the trypsin. Each sample was then transferred to a 15 mL conical centrifuge tube and centrifuged for 5 min at 1400 rpm and 4°C. The supernatant was poured off, the cells were resuspended in 1 mL PBS, and centrifuged again at the same settings. Then the supernatant was poured off again and the cells were resuspended in 1.5 mL PBS. While vortexing, 0.5 mL of 4% PFA was added dropwise to each tube, and vortexing continued for an additional 10 sec. Samples were incubated on ice in the dark for 15 min, then centrifuged at the previous settings. The supernatant was poured off and they were resuspended in PBS, then centrifuged again. Supernatant was poured off and the cells were resuspended in 0.6

mL of distilled water, then 1.4 mL of freezer cold 100% ethanol was added dropwise while vortexing, and vortexing continued for a further 10 sec. Samples were then placed in a -20°C freezer until the day of data collection (3-4 days).

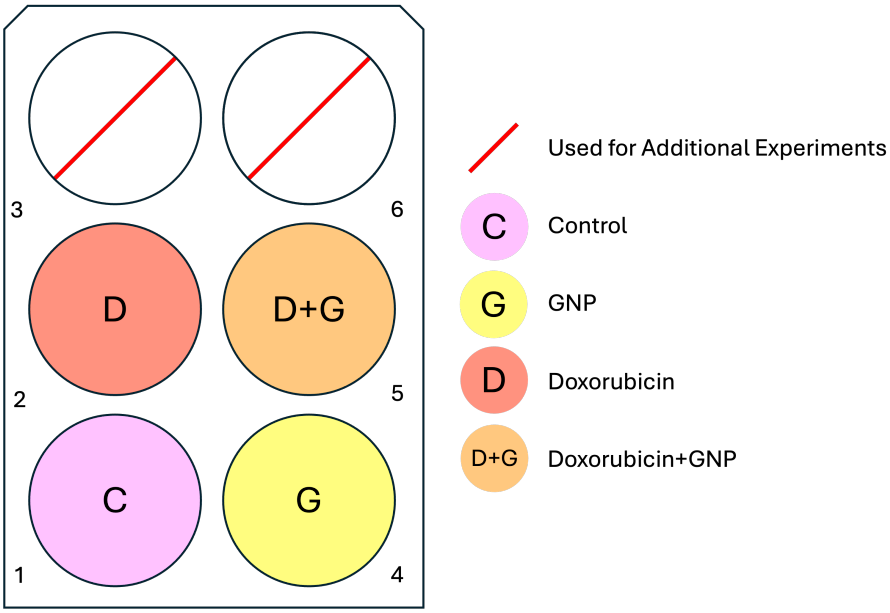

Figure 2.4: 6-well plate layout used for cell cycle assay, double strand break assay, and for the dosing and irradiation steps of the clonogenic assay. Multiple plates were seeded as required for the given assay. For additional experiments see Appendix A.

On the day of data collection, samples were removed from the freezer and centrifuged at 1400 rpm and 20°C for 10 min. Buffers of 0.5% Bovine Serum Albumin (BSA) in PBS and 0.5% BSA and 0.1% Triton-X in PBS were prepared. Supernatant was poured off, cells were resuspended in 1 mL 0.5%BSA/PBS, and centrifuged at 1400 rpm and 20°C for 5 min. Supernatant was poured off and cells were resuspended in 1 mL 0.5%BSA/0.1%Triton-X/PBS. 50 μL of 2 mg/mL RNaseA was added to each tube to achieve a concentration of 100 μg/mL. Samples were incubated on a shaker at 37°C for 25 min. Propidium iodide was added to a concentration of 0.01 mg/mL, and then samples were incubated on a shaker in the dark at 4°C for one hour. Each sample was then passed through a 100 μm nylon net filter (Millipore) while being transferred to a flow cytometry tube. Samples were read using a FACSCalibur flow cytometer (BD Biosciences).

2.3 Radiation Experiments

2.3.1 Radiation Treatment

For any assay where the cells needed to be irradiated, a Varian TrueBeam clinical linear accelerator (linac) was used. Cell plates were positioned so the bottom of the plates, where the cells were adhered, would be at isocenter (Source Axis Distance = 100 cm). Plates were placed between two 5 cm thick blocks of Solid Water® (Sun Nuclear). Irradiation was performed from below (Gantry angle 180°) to reduce the air gap between the Solid Water® and the cells created by the culture plate. A 28x28 cm field was used, which was able to accommodate up to six culture plates in a single beam, with at least 1 cm between the plate edge and the field penumbra. Either 2 Gy or 5 Gy was delivered using a 6 MV beam at the maximum dose rate of 600 MU/min. To maintain consistency of other growth conditions, unirradiated plates were also brought to the linac location but were left outside the bunker. 2 Gy and 5 Gy were used as these are clinically relevant doses often used in fractionated radiotherapy treatment regimes.

2.3.2 Proliferation Assay

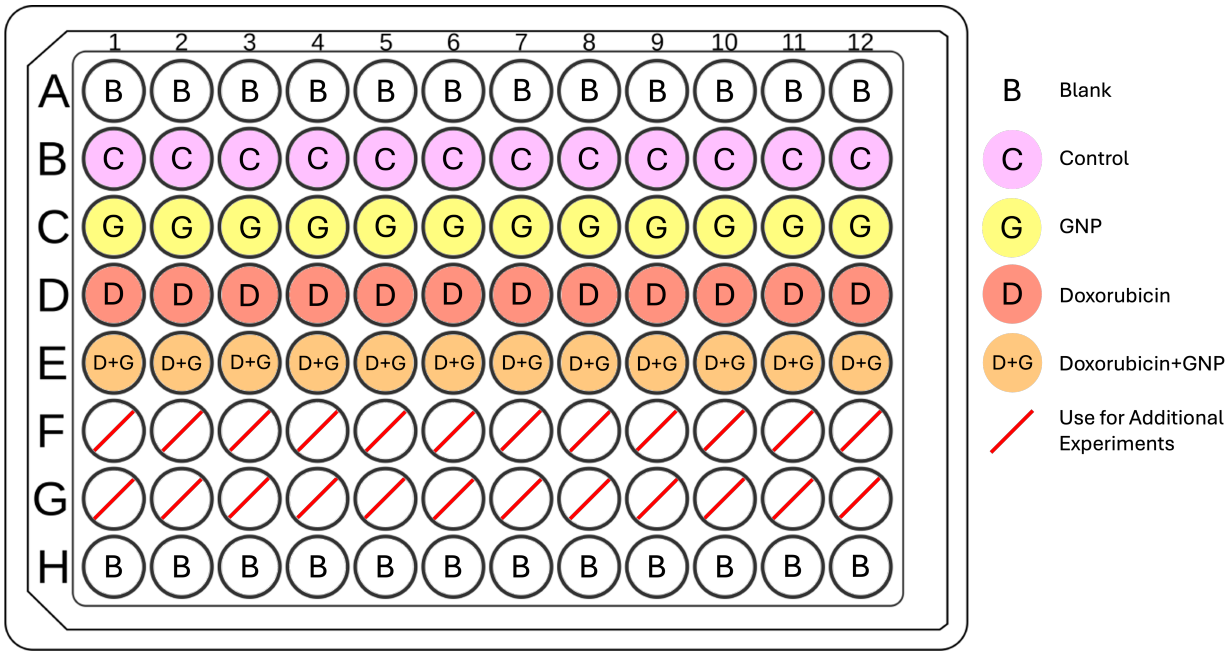

Figure 2.5: 96-well plate layout used for cellular proliferation assay.

Cells were plated in 96-well plates such that there would be 40,000 cells in the control

group after 6 days. 6 plates were seeded, 2 per radiation condition, and the experiment was repeated 3 times. The A and H rows were not used, and were instead filled with PBS to reduce edge effects. After seeding, the plates were sealed with a breathable membrane and incubated for 24 hours to allow the cells to adhere. Cells were dosed with DOX and GNPs according to the layout seen in Figure 2.5. Plates were resealed and incubated for 48 hr. After 48 hr, plates were irradiated with 2 Gy or 5 Gy using a clinical linear accelerator (Varian) or were unirradiated (0 Gy). After irradiation, the media was removed from all wells and replaced with fresh media, then the plates were resealed and returned to the incubator. For each radiation condition, half of a plate including blank wells (columns 1-6 or 7-12) was aspirated and 100 μL of 10% PrestoBlue in media was added. The plates were incubated for 1 hour and then the fluorescence of the open wells was read with a plate reader. Readings were taken immediately after irradiation, and again every 24 hr after that for 3 days.

To compute relative growth on a given day, the average blank fluorescence was subtracted from the average reading for each condition, and this was divided by the reading for that condition from day 0 (immediately post irradiation).

2.3.3 Clonogenic Assay

Cells were seeded in 6-well plates and incubated for 24 hours for the cells to adhere. They were dosed according to the plate layout in Figure 2.4. Cells were incubated with the dosed media for 48 hours, and then irradiated with 0 Gy, 2 Gy, or 5 Gy. Immediately after radiation, cells were dissociated from 6-well plates and each condition was counted using a hemocytometer. The cell suspensions were diluted such that the desired number of cells to seed could be found in a volume between 100 μL and 1 mL. Dilutions were performed 1:10 until the desired concentration was reached. 60 mm cell culture plates were labelled and 4 mL of media was added to each. The appropriate volume was added dropwise to each plate to achieve the desired cell count. Plates were carefully transferred to a 37°C, 5% CO_2 incubator and incubated for 12 days to allow colonies to form.

During incubation, clonogenic assay plates were kept in a secondary incubator set aside for this purpose to reduce jostling. After 12 days incubation the lid was removed from each plate and the media was carefully poured off. Enough 0.5% methylene blue (BioShop) was added to each plate to cover the bottom, and plates were stained for 15 minutes. Next, the methylene blue was poured off and the plates were carefully rinsed face down in water. Plates were then left overnight to dry. The next day, colonies were counted manually. Any cluster of 50 or more cells was scored as a colony. This procedure was adapted from the

methods given by Munshi, et al. [130].

To compute the surviving fraction of cells, first the plating efficiency (PE) is calculated by dividing the number of colonies by the number of cells seeded. This was computed for each plate, and then averaged for each condition, as all conditions had been plated in triplicate. The survival fraction (SF) for a certain condition is given by its plating efficiency divided by the plating efficiency of the unirradiated control cells.

$$\text{PE} = \frac{\text{\# colonies}}{\text{\# cells seeded}} \qquad \text{SF} = \frac{\text{PE}}{\text{PE of control}} \tag{2.8}$$

2.3.4 DNA Double Strand Break Assay

Cells were seeded in 6-well plates with a glass microscope coverslip placed in the bottom. After 24 hours for cells to adhere, they were dosed with DOX and GNPs according to the plate layout in Figure 2.4. After 48 hours incubation with the drug formulations, cells received either 0 Gy (unirradiated), or 2 Gy of radiation from a clinical linear accelerator. 5 Gy was not used for this experiment as it causes so much DNA damage that the repair foci are uncountable. After irradiation, media was aspirated and replaced with fresh media. Cells were incubated a further 24 hours to allow DNA damage foci to form. After 24 hours media was aspirated, then cells were washed with PBS and fixed with 4% paraformaldehyde (PFA) for 10 min. Cells were washed twice more with PBS, 5 minutes for each wash, and then blocked with a solution of 2% BSA and 0.1% Triton-X in PBS for 20 minutes. The two primary antibodies and the two secondary antibodies were diluted 1:200 and 1:500, respectively, in 0.5% BSA and 0.1% Triton-X in PBS. The coverslips were carefully lifted out of the 6-well plates and placed cell-side down on 50 μL of each primary antibody on clean parafilm. They were incubated with the primary antibodies in the dark for one hour. Coverslips were placed back into their wells in the 6-well plates, cell-side up, and washed two times with PBS, 5 minutes per wash. Next they were washed with 0.5% BSA and 0.1% Triton-X in PBS. Then they were lifted out of the wells and placed cell-side down on 50 L each of the secondary antibodies, and incubated in the dark for 45 minutes. Coverslips were returned to their wells in the 6-well plates, cell-side up, and washed with PBS for 5 minutes. They were fixed again with 4% PFA for 5 minutes, then given a final wash with PBS. Coverslips were carefully dried and fixed to labelled microscope slides using ProLong™ glass Antifade with NucBlue™ (Invitrogen). Slides were kept in the dark and left for 48 hours to cure. Imaging was done with a laser scanning confocal microscope (Zeiss). Multiple images were taken in different areas of the slide, and each was taken as a z-stack to encompass

the entire cell and then compressed into a single image to count the foci. Image processing was performed in ImageJ and foci were manually counted.

2.4 Statistical Analysis

P values were calculated using a Welch's independent t-test. This test was used as it applies even when samples have differing variance and sample sizes. The test statistic, t, for a Welch's t-test is given by,

$$t = \frac{\Delta\overline{X}}{s_{\Delta\overline{X}}} = \frac{\overline{X}_1 - \overline{X}_2}{\sqrt{s^2_{\overline{X}_1} + s^2_{\overline{X}_2}}} \tag{2.9}$$

where $s_{\overline{X}_i} = s_i/\sqrt{N_i}$ is the standard error for the i^{th} sample with mean $\overline{X}_i$, standard deviation s_i, and sample size N_i. The degrees of freedom, v, for this test statistic is calculated using,

$$v \approx \frac{\left(\frac{s_1^2}{N_1} + \frac{s_2^2}{N_2}\right)^2}{\frac{s_1^4}{N_1^2(N_1-1)} + \frac{s_2^4}{N_2^2(N_2-1)}} \tag{2.10}$$

The test statistic and degrees of freedom are used with the Student's t-distribution to calculate the p value. $P<0.05$ was considered statistically significant.

Section 3

Results and Discussion

3.1 Gold Nanoparticle Characterization

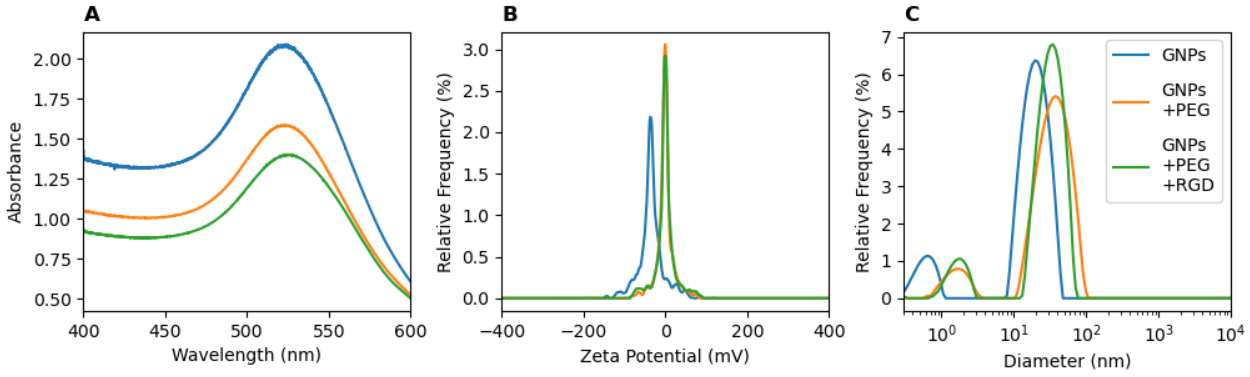

Figure 3.1: Characterization figures for plain GNPs and GNPs functionalized with PEG and RGD. (A) UV-Vis plot. (B) Zeta potential. (C) Hydrodynamic diameter measured using DLS.

Table 3.1: Characterization data for GNP, GNP+PEG, and GNP+PEG+RGD functionalized nanoparticles from UV-Vis Spectroscopy, Zeta Potential, and DLS.

	Peak Absorption Wavelength (nm)	**Zeta Potential (mV)**	**Hydrodynamic Diameter (nm)**
GNPs	524.55 ± 0.05	-32 ± 5	16.03 ± 0.03
GNPs+PEG	521.00 ± 0.05	-2.1 ± 0.4	28.68 ± 0.09
GNPs+PEG+RGD	526.05 ± 0.05	0.3 ± 0.2	26.2 ± 0.5

Gold nanoparticles were prepared with a hydrodynamic diameter of 16.03±0.03 nm as measured by DLS, and a zeta potential of -32±5 mV. From the UV-Vis results, the particle diameter was calculated to be 12.8 nm, and the concentration was 240.12 μg/mL. After

functionalization with PEG and RGD, the hydrodynamic diameter was increased to 26.2 nm and the positively charged RGD peptides shifted the zeta potential to 0.3±0.2 mV. The DLS results showed a second small peak (Figure 3.1C) at 0.7 nm for the plain GNPs and at 1.7 nm for GNPs+PEG+RGD. This may be gold seeds leftover from the synthesis process that never formed larger nanoparticles [131, 132]. As these seeds only make up a small portion of the nanoparticles, they are inconsequential for the in vitro experiments performed in this work. However this could be of concern in future in vivo studies, as different sized nanoparticles may have different levels of toxicity [133].

3.2 Results for Breast Cancer Cell Line MDA-MB-231

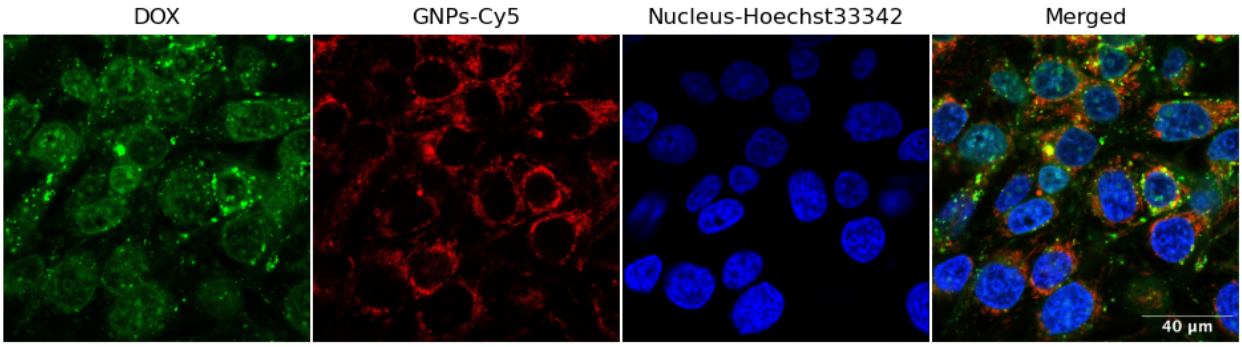

Figure 3.2: Live cell confocal imaging of MDA-MB-231 cells containing DOX (green channel) and GNPs functionalized with PEG-Cy5 (red channel). Cell nuclei are stained with NucBlue (Hoechst33342, blue channel).

Live cell images (Figure 3.2) were taken to demonstrate the internalization of DOX and GNPs in the cells. DOX has an inherent fluorescence, with the excitation peak at 470 nm and the emission peak at 560 nm [134]. GNPs were functionalized with Cy5, which has an excitation peak at 647 nm and an emission peak at 665 nm. Cell nuclei were stained with NucBlue containing Hoechst33342, which has an excitation peak at 360 nm and an emission peak at 460 nm.

In Figure 3.2 it can be seen that the GNPs are found throughout the cell but tend to cluster near the nucleus. DOX is seen distributed throughout the cell, with some brighter spots that are likely lysosomes which have sequestered the drug [135].

3.2.1 Cytotoxicity Assay

Prior to beginning cell culture studies, it was necessary to determine the concentration that should be used when dosing cells with DOX. Maass et al. used a novel method to measure the

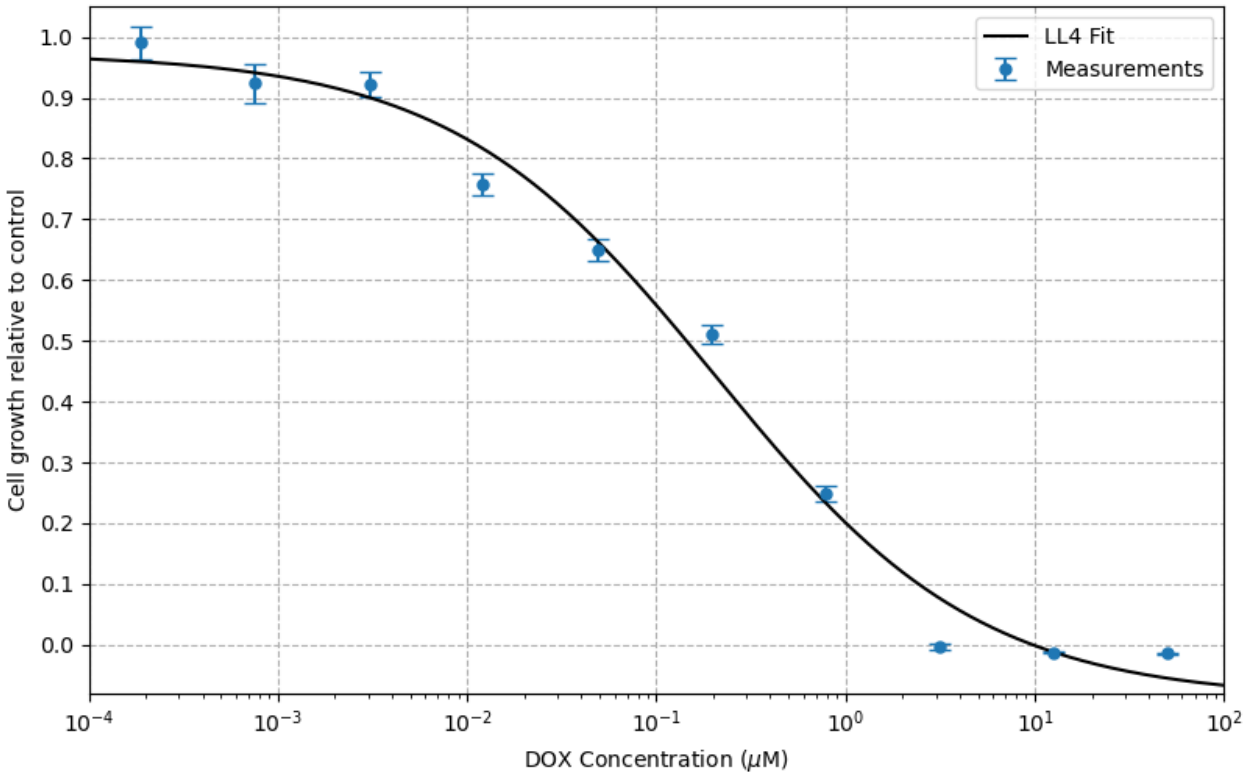

Figure 3.3: Relative cell growth versus DOX concentration used to determine the IC50 of DOX for MDA-MD-231 cells after 48 hour drug incubation time. The IC50 was determined to be 144.4 nM. The experiment was performed in triplicate and the error bars represent the standard error in the mean between the three plates.

IC50 of DOX, and found that after 24 hours incubation the IC50 was 45 nM for MDA-MB-231 [136]. Other experiments demonstrated a wide range of IC50 values for DOX, dependent on the cell line, drug incubation time used, and growth conditions [137–140]. Based on that data as well as preliminary experiments, a concentration range of 0.19 nM-50 μM was used as it was expected to encompass the inflection point of the curve. The IC50 of DOX for MDA-MB-231 cells was determined from Figure 3.3 to be 144.4 nM. This is the concentration at which DOX was dosed for all other experiments using MDA-MB-231 cells, including the live cell images pictured in Figure 3.2. As the efficacy of DOX is impacted by cell passage number [141], experiments were conducted in quick succession and only passage numbers below 15 were used.

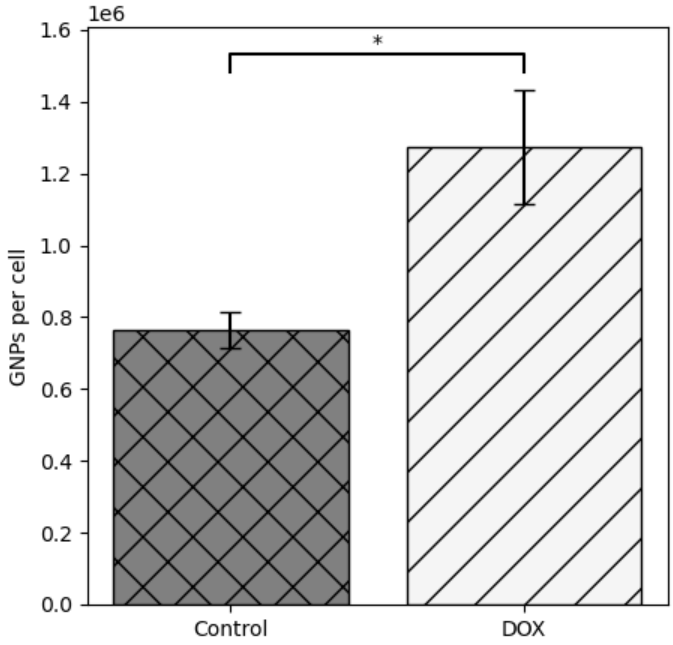

Figure 3.4: Gold nanoparticle uptake by MDA-MB-231 cells treated with DOX. Cells were treated for 48 hours with GNPs at 7.5 μg/mL and/or DOX at 144.4 nM. The experiment was performed in triplicate and the error bars represent standard error between wells. * indicates a significant difference between results ($p<0.05$, two-tailed Welch's independent t-test).

3.2.2 Cellular Uptake

To ascertain if DOX would affect the amount of gold that was taken up into the cells, which could affect the cells' response to radiation in later studies, the uptake of gold into the cells was measured using ICP-MS. Control cells contained on average $(0.76\pm0.05)\times10^6$ GNPs per cell. Samples incubated with DOX contained on average $(1.27\pm0.16)\times10^6$ GNPs per cell. The significant increase ($p<0.05$) in GNPs per cell seen with DOX is likely due to DOX interfering with the microtubule network [142]. The microtubule network is used to move vesicles [143], which contain the GNPs, around the cell. Interfering with this network may prevent the cells from expelling the GNPs, resulting in an increase in the measured uptake [144].

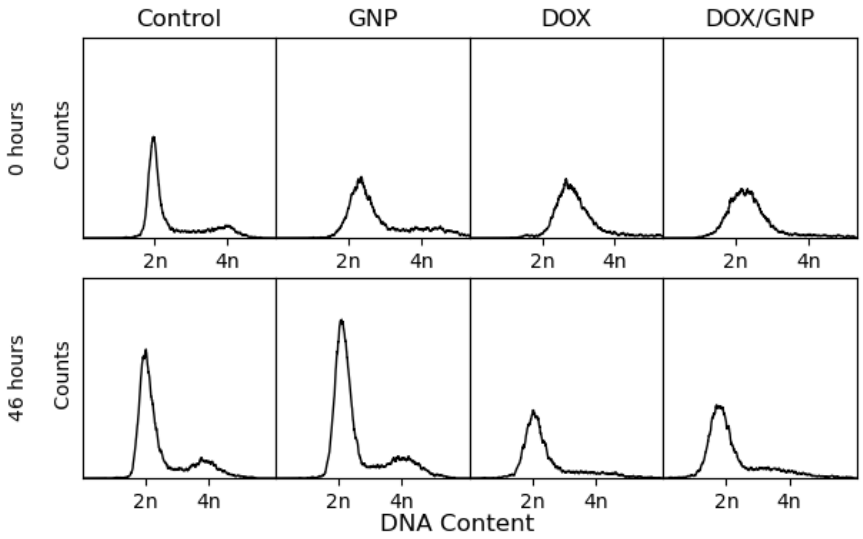

Figure 3.5: Flow cytometry results for MDA-MB-231 cells incubated with DOX and GNPs. Cells were unirradiated, and data was collected at two time points after removing the treated media, 0 hours and 46 hours. DNA content is based on the amount of propidium iodide measured by flow cytometry. 2n and 4n DNA content was labelled based on the locations of the peaks in the 0hr and 46hr control samples. 2n DNA indicates the G1 phase, and 4n indicates the G2/M phase. Cells were treated for 48 hours with GNPs at 7.5 μg/mL and/or DOX at 144.4 nM.

3.2.3 Cell Cycle

The flow cytometry results shown in Figure 3.5 indicate cell accumulation in G1 and S phase at the 0 hour time point in the samples that were treated with DOX, however it is not conclusive. After 46 hours the G1 peak is beginning to appear, but there is no indication of the typical G2/M peak. The lack of clear cell cycle phases in the DOX samples, combined with the large appearance of the cells in Figure 3.9, may indicate that the cells entered senescence and ceased progressing through the cell cycle [145]. This will be discussed further in Section 3.2.4.

3.2.4 Cell Growth

Two experiments were performed which assessed overall cell growth and survival. A proliferation experiment (Section 2.3.2) in 96-well plates was conducted to assess short term growth of MDA-MB-231 cells after treatment. A long term colony formation assay (Section 2.3.3) was also conducted, which assessed the cells' ability to survive at least six cell divisions and form new colonies. A cell that is capable of forming new colonies after treatment is referred

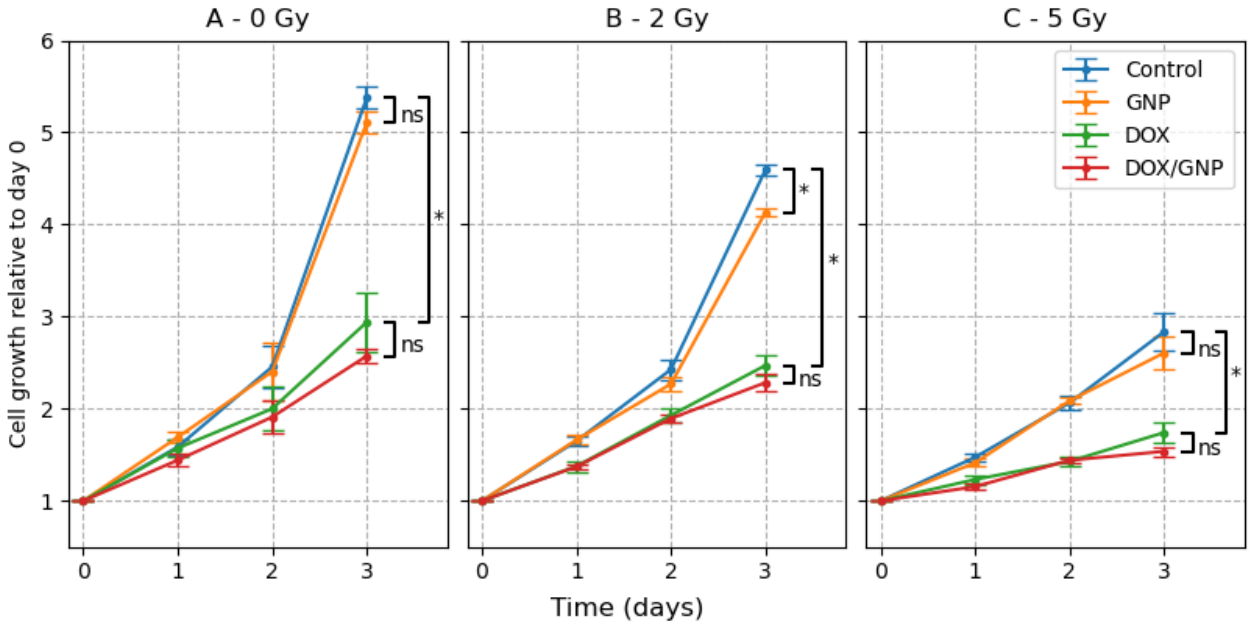

Figure 3.6: Cellular proliferation over three days of MDA-MB-231 cells treated with DOX, GNPs, and radiation. Cell growth is relative to the first set of measurements. The experiment was performed in triplicate with 6 wells per condition per plate per reading, for a total of 18 wells for each data point. Prior to irradiation, cells were treated for 48 hours with GNPs at 7.5 μg/mL and/or DOX at 144.4 nM. Error bars represent the standard error. * indicates a significant difference between results ($p<0.05$) and "ns" indicates no significant difference ($p>0.05$) using a two-tailed Welch's independent t-test.

to as clonogenic, and clonogenic survival is considered the highest standard when assessing the effects of radiotherapy and other treatments on cancer cells [146].

The cellular proliferation results are shown in Figure 3.6 and Table 3.2. 2 Gy of radiation caused a (15±2)% reduction in cell growth, compared to the unirradiated control. 5 Gy of radiation had a much larger effect, with (48±4)% reduction in cell growth. MDA-MB-231 are known to be radioresistant [147], so the lack of response at the lower radiation dose is expected.

Table 3.2: Relative growth values for MDA-MB-231 after 3 days of growth.

	Day 3 Relative Growth		
	0 Gy	**2 Gy**	**5 Gy**
Control	5.4 ± 0.1	4.59 ± 0.06	2.8 ± 0.2
GNP	5.1 ± 0.1	4.13 ± 0.05	2.6 ± 0.2
DOX	2.9 ± 0.3	2.5 ± 0.1	1.7 ± 0.1
DOX/GNP	2.57 ± 0.07	2.28 ± 0.09	1.54 ± 0.05

The GNPs showed little effect in this assay, with no significant differences between the DOX and DOX/GNP samples at any radiation level. The control and GNP samples showed some evidence of radiosensitization at 2 Gy on day 3, with (24±2)% reduction in growth between the 0 Gy control and 2 Gy GNP samples versus (15±2)% reduction in growth between the 0 Gy and 2 Gy control sample. However this did not occur at 5 Gy where there was no significant difference between the samples, and no significant differences between the GNP and no-GNP sample pairs were observed on days 1 or 2.

DOX caused radiosensitization at 2 Gy with a (54±2)% reduction in cellular proliferation. However, the treatment was not synergistic as the DOX only and 2 Gy only caused (46±6)% and (15±2)% reduction in growth, respectively. Similarly, the combination of 5 Gy radiation and DOX caused a (69±8)% reduction in growth, but 5 Gy only caused (48±4)% and DOX only caused (46±6)% reduction in growth. Thus there is no evidence from this in vitro study that concomitant administration of these therapies is more effective than adjuvant or neoadjuvant administration.

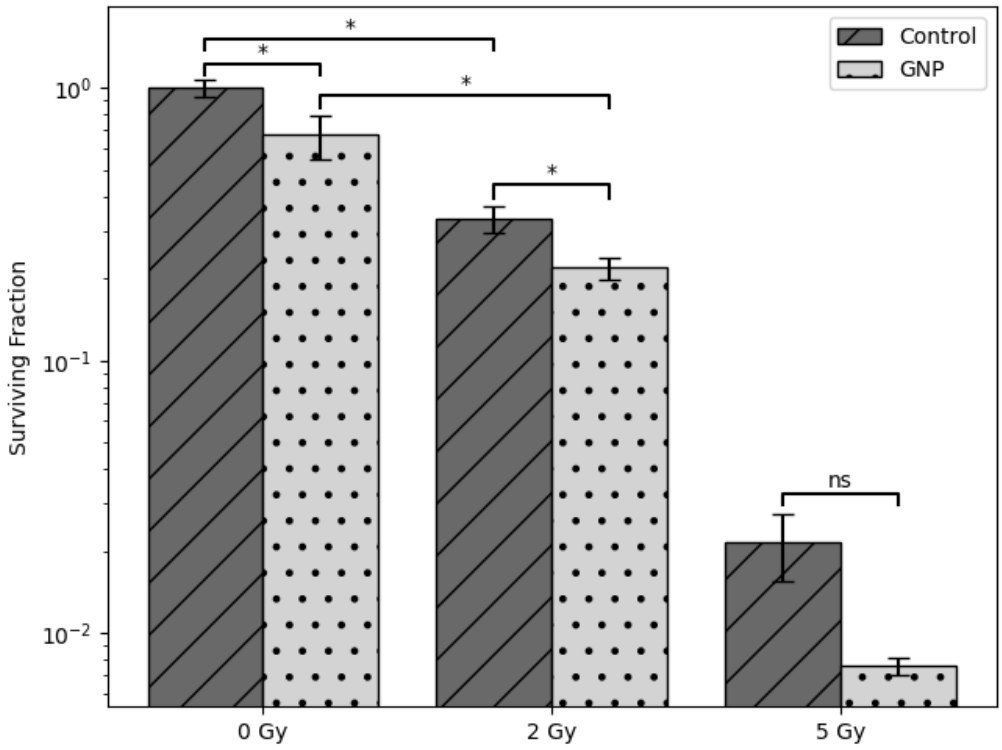

Figure 3.7: Clonogenic assay results for MDA-MB-231 cells. GNPs were dosed at 7.5 μg/mL for 48 hours. Error bars represent the standard error between all plates for a given condition, with at least three colony forming plates per condition. Prior to irradiation, cells were treated for 48 hours with GNPs at 7.5 μg/mL. * indicates a significant difference between results ($p<0.05$, two-tailed Welch's independent t-test).

Table 3.3: Tabulated clonogenic assay results for MDA-MB-231. GNPs were dosed at 7.5 μg/mL for 48 hours. Given uncertainty is the standard error between all plates for a given condition, with at least three colony forming plates per condition.

	Survival Fraction		
	0 Gy	**2 Gy**	**5 Gy**
Control	1.00 ± 0.07	0.33 ± 0.04	0.021 ± 0.006
GNP	0.7 ± 0.1	0.22 ± 0.02	0.0076 ± 0.0005

Multiple clonogenic assays were conducted, with conditions plated in triplicate each time, and Figure 3.7 shows the average of the results. Each time, no matter how many cells were seeded initially, no colonies were counted in the DOX treated plates. This may be due to cell death via mitotic catastrophe, where the DOX causes damage that does not induce cell death until after the cell has undergone mitosis once or more [148]. This sort of damage would not be seen in a shorter term assay such as cell proliferation (Section 2.3.2, Figure 3.6), which only measures cell growth over three days and will only see one or two cell divisions. Another explanation is that DOX is inducing senescence in the cells. Many studies have shown that DOX induces senescence in multiple cell lines [149–154]. Doses of DOX ranging from 20 nM [153] to 200 nM [152] have been used to intentionally induce senescence in order to study it. The dose required depends on the cell line, dosing time, and growth conditions. As the dose of 144.4 nM used to dose MDA-MB-231 cells for this experiment falls within this range, it is reasonable to assume that it is sufficient to induce senescence. Senescent cells are still metabolically active, so they will appear as viable cells in the proliferation assay. However they no longer undergo mitosis, so they will not form colonies in the clonogenic assay. One of the morphological changes associated with senescence is large flat cells [155], which can be seen in Figures 3.9 and 3.2, providing further support for this hypothesis.

At 0 Gy, the cells incubated with GNPs alone had (30±11)% less ($p<0.05$) clonogenic survival than the control cells. The lower clonogenic survival in the unirradiated GNP incubated samples indicates there may be some toxicity introduced by the GNPs. This has been observed before in MDA-MB-231 cells. Jeyarani, et al. observed GNP toxicity in MDA-MB-231 cells using spherical, 12 nm diameter, biomimetic gold nanoparticles at an IC50 of 43.09±1.6 μg/mL [156]. Surapaneni et al. also observed gold toxicity in MDA-MB-231, with IC50 values of 720 μg/mL using 212.7 nm citrate-capped GNPs, and 635 μg/mL using 40 nm cysteamine-capped GNPs [157]. Abu-Dahab et al. used gold nanorods and found an IC50 of 0.59 μg/mL [158]. Other research using a variety of cell lines and GNP modifications has shown contradictory results on whether gold nanoparticles are cytotoxic or not [133, 159, 160]. The level of toxicity depends on the cell line, the size and shape of the

nanoparticles, any surface modifications, the dosing concentration, the growth conditions, and the method by which the toxicity is measured [161, 162]. There is even evidence that, when performing experiments in vivo, the method by which the GNPs are administered can affect the toxicity [163]. While the broader question of whether or not GNPs are toxic is yet to be answered, the studies listed show that MDA-MB-231 in particular is sensitive to GNP toxicity, which supports the results shown here.

In the cells which received radiation only, 2 Gy radiation caused a (67±5)% decrease and 5 Gy caused a (97.9±0.6)% decrease in clonogenic survival when compared to the control. The combined treatment of GNPs and 2 Gy of radiation yielded a (78±3)% decrease in clonogenic survival, demonstrating some radiosensitization by the GNPs. A Bliss independence test [164] was conducted to evaluate the synergy of the GNP and 2 Gy radiation treatments. The Bliss independence model uses a combination index (CI) calculated by,

$$CI = \frac{E_A + E_B - E_A E_B}{E_{AB}} \tag{3.1}$$

where E_A and E_B are the effect of treatment A and treatment B, respectively, and E_{AB} is the effect of the combined treatment, with $0 \leq E_A, E_B, E_{AB} \leq 1$. The treatments are considered synergistic if $CI < 1$, independent if $CI = 1$, and antagonistic if $CI > 1$ [165, 166]. In this case, the effect used was the amount of clonogenic growth that was inhibited by the GNPs or the radiation. GNPs plus 2 Gy radiation had a combination index of 0.99±0.07, indicating the effect was independent. At 5 Gy, there was no significant difference between the GNP and 5 Gy control sample, which matches the 5 Gy proliferation results in Figure 3.6.

3.2.5 DNA Damage

DNA damage can be induced by radiation or by chemotherapy drugs. 53BP1 and γH2AX are both proteins which are known to regulate DNA repair, and are indicative of double strand breaks [84, 167]. Here, both 53BP1 and γH2AX foci were imaged and counted. Figure 3.9 demonstrates this qualitatively while Figure 3.8 shows it quantitatively. The numbers presented in Figure 3.8 represent the total number of 53BP1 and γH2AX foci counted. Co-localized 53BP1 and γH2AX foci were only counted once. Multiple images from different areas of the microscope slide were used such that at least 50 nuclei were counted. As can be seen in Figure 3.9, DOX induced so much DNA damage that the foci were uncountable, so those samples were omitted from Figure 3.8.

In Figure 3.9 the DOX incubated cells are much larger than the control cells, which supports the conclusion that the cells have entered senescence, as discussed previously. The

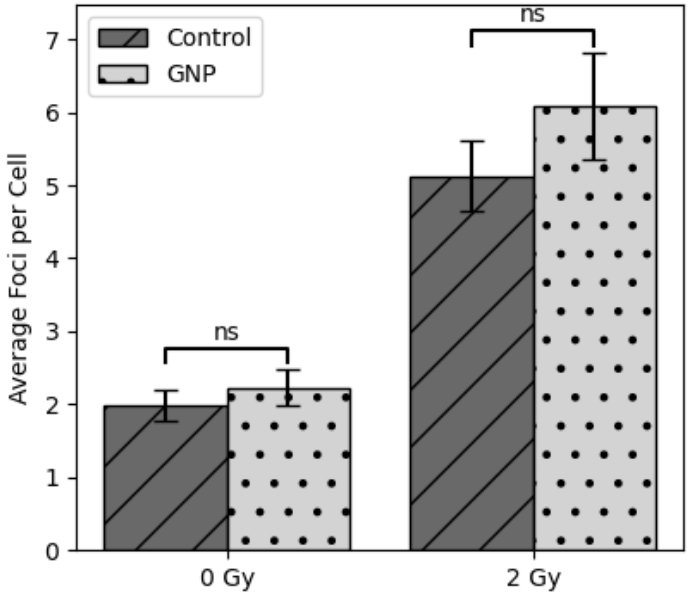

	Average Foci per Cell	
	0 Gy	**2 Gy**
Control	2.0 ± 0.2	5.1 ± 0.5
GNP	2.2 ± 0.2	6.1 ± 0.7

Figure 3.8: Number of DNA repair foci, γH2AX and 53PB1, counted in MDA-MB-231 cells. Multiple images were taken so that at least fifty unique nuclei were counted for each sample. Error bars represent the standard error amongst all of the nuclei counted for a sample. GNPs were dosed at 7.5 μg/mL for 48 hours. "ns" indicates no significance difference ($p>0.05$, two-tailed Welch's independent t-test).

GNPs made no significant difference on the number of DNA damage foci, indicating that they are causing harm to the cells in other ways. Research has indicated many possibilities for the mechanism of action by which GNPs cause cell damage, including oxidative stress, membrane damage, and mitochondrial damage [168, 169].

In the cells which were not treated with DOX or GNPs, 2 Gy radiation caused an increase in DNA damage foci from 2.0±0.2 to 5.1±0.5 foci per cell. No significant difference in foci was seen between the control and the GNP incubated cells at 0 or 2 Gy.

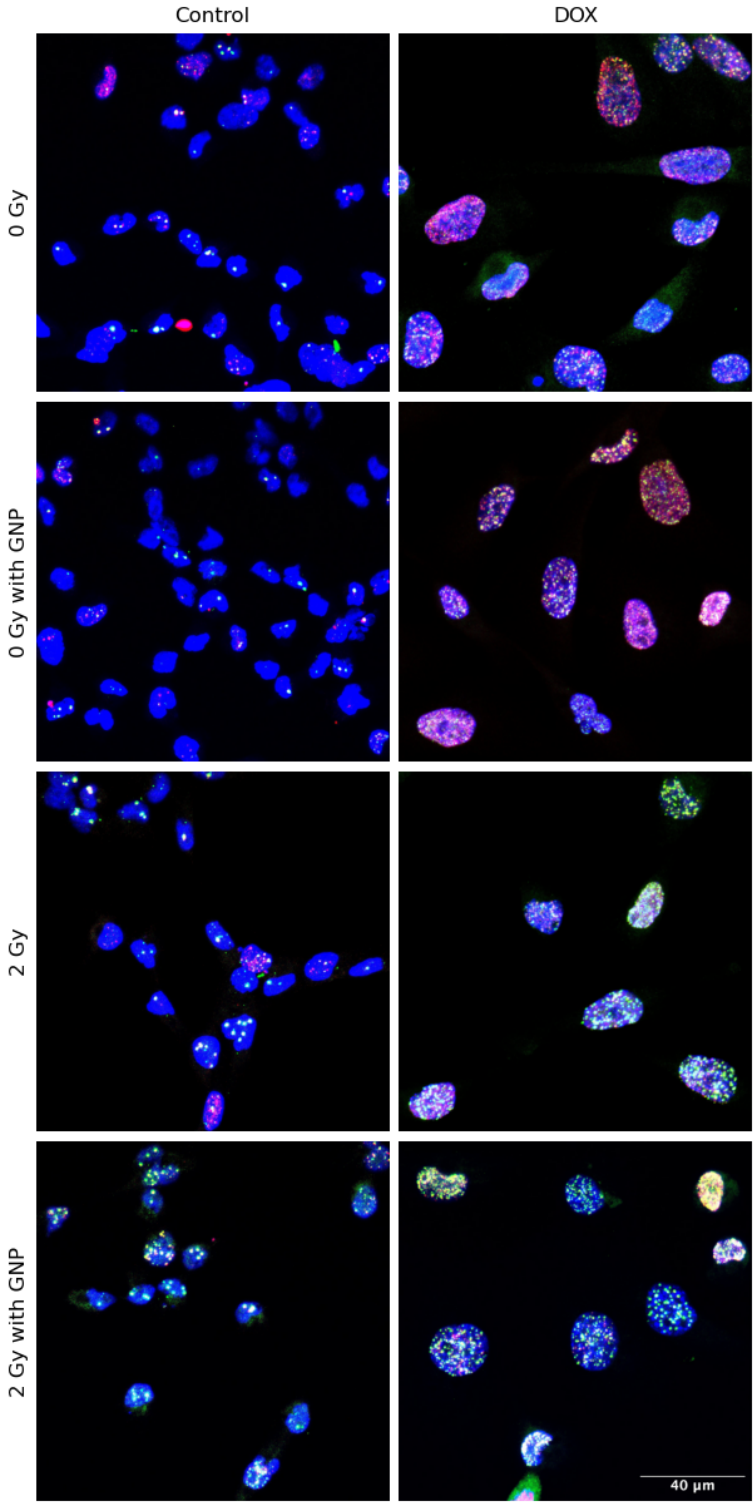

Figure 3.9: Confocal imaging of DNA damage indicators in MDA-MB-231 cells containing DOX and GNPs. Blue is Hoechst 33342 used to stain the cell nucleus. Red is Alexa Fluor 647, used to label γH2AX. Green is Alex Fluor 488, used to label 53BP1. Cells were treated for 48 hours with GNPs at 7.5 μg/mL and/or DOX at 144.4 nM.

Section 4

Conclusions and Future Work

4.1 Conclusions

The IC50 of doxorubicin (DOX) for MDA-MB-231 cells was found to be 144.4 nM. Cells incubated with DOX showed an increase in GNP uptake, and it affected the distribution of cells in the cell cycle but did not show definitive cell cycle arrest. The short term proliferation assay showed approximately significant growth inhibition, as expected given it was dosed at the IC50 concentration. There was evidence of radiosensitivity in the proliferation assay, but the effect was not synergistic. However, it was evident from the clonogenic and DSB results that DOX was having an extreme effect on the MDA-MB-231 cells, which resulted in no colonies forming and in the DNA damage being so extensive that the foci were uncountable. The conclusion reached was that DOX was inducing senescence in the MDA-MB-231 cells. As this was unexpected given the cells were being dosed at the IC50 of DOX, the method of determining the IC50 should be reassessed.

The data gathered for this thesis showed no GNP toxicity in the short term proliferation assay, but did show toxicity in the long term clonogenic assay. While some research performed with gold nanoparticles (GNPs) similar to those used in this work has shown they are biocompatible with MDA-MB-231 cells [92, 103, 170], those studies used lower dosing concentrations, a much shorter treatment time (24 hours or less), and were not studying toxicity specifically. As the question of GNP toxicity in general is yet to be answered, it would be prudent for future work to examine this in more detail. Additionally, there was evidence of radiosensitization by GNPs at 2 Gy in the proliferation and clonogenic assay, however there was no synergy due to the GNP toxicity. No radiosensitization by GNPs was seen when 5 Gy of radiation was used, and it was not seen in the DOX treated cells either. Additionally, the GNPs did not affect the amount of DNA double strand breaks at 0 Gy or 2 Gy.

In summary, DOX was more effective as a cytotoxic agent against the MDA-MB-231 cells than expected, due to inducement of senescence in the cells. Additionally, the GNPs showed evidence of GNP induced toxicity, and evidence of radiosensitization at 2 Gy, but not at 5 Gy.

4.2 Future Work

While cellular senescence was determined to be a plausible explanation for the DOX results shown here, it would be worthwhile to further validate this experimentally. There is no single marker which indicates that cells have entered senescence, however cell cycle arrest, lack of proliferation, morphology changes to large and flat cells, and the DNA damage markers γH2AX and 53BP1, all of which were observed in this work, are all markers of senescence [145]. Vassilis, et al. proposed testing first for senescence-associated beta-galactosidasde (SA-β-gal) activity and then the $p16^{Ink4a}$ and $p21^{WAF1/Cip1}$ proteins, as part of the senescence identification workflow [171]. Adewoye, at al. developed a flow cytometry based protocol to detect SA-β-gal activity in addition to $p16^{Ink4a}$ and γH2AX expression to verify senescence [152], which could be applied here.

In order to continue studying the use of DOX as a radiosensitizer, it will need to be dosed at a low enough concentration that it is not inducing a significant amount of senescence. First, the IC50 could be reassessed using a more robust method which will exclude senescent cells from the viable cell count, such as a colony forming assay [172]. Then concentration and drug exposure time should be adjusted so that some toxicity is seen but senescence is not induced. Alternatively, experiments could be performed with a cell line which responds differently to DOX, such as Hela [173].

The toxicity of gold nanoparticles is still very uncertain, and given the number of variables that can affect cellular response, including size, shape, surface capping, exposure time, and cell line used, future work should first evaluate this GNP formulation's toxicity [169]. This could take the form of measuring the IC50, or by administering the desired treatment and conducting a colony formation assay. The toxicity should be reevaluated if there are any changes in the treatment protocol, such as if the exposure time is changed, or if a different cell line is used.

Once the appropriate dosing concentrations for DOX and GNPs has been determined, the effectiveness of the combined treatment can be verified in monolayer cell culture. The next stage of the research is to use three dimensional in vitro cell models, such as tumour spheroids. Spheroids are able to better mimic the tumour microenvironment which is observed in situ

[174]. They have an oxygenation gradient from the outside to the center, with a hypoxic core, and also display similar concentration gradients for GNPs and drugs which they are exposed to [175]. Additionally, co-culture methods can be used to replicate other aspects of the tumour microenvironment such as the presence of cancer associated fibroblasts [176]. This technique can also be used to investigate the immune response to the treatment, something which is lacking from many in vitro experimental techniques [177]. Co-culture of cancer cells with immune cells enables the replication of immune penetration into the tumour [178], which is of particular interest for this research as immune cells can take up GNPs and affect the number of GNPs circulating in the blood, thus reducing the uptake of GNPs into the cancer cells.

Bibliography

[1] F. Bray, M. Laversanne, H. Sung, J. Ferlay, R. L. Siegel, I. Soerjomataram, and A. Jemal, "Global cancer statistics 2022: GLOBOCAN estimates of incidence and mortality worldwide for 36 cancers in 185 countries," *CA: A Cancer Journal for Clinicians*, vol. 74, no. 3, pp. 229–263, 2024.

[2] Canadian Cancer Statistics Advisory Committee in collaboration with the Canadian Cancer Society, Statistics Canada and the Public Health Agency of Canada, "Canadian Cancer Statistics 2023," tech. rep., Canadian Cancer Society, Toronto, ON, Nov. 2023.

[3] G. Chaput and L. Regnier, "Radiotherapy," *Canadian Family Physician*, vol. 67, pp. 753–757, Oct. 2021.

[4] E. B. Podgoršak, *Radiation Physics for Medical Physicists*. Biological and Medical Physics, Biomedical Engineering, Heidelberg: Springer, 2nd, enl. ed ed., 2010.

[5] E. B. Podgoršak and International Atomic Energy Agency, eds., *Radiation Oncology Physics: A Handbook for Teachers and Students*. Vienna: International Atomic Energy Agency, 2005.

[6] G. P. Delaney and M. B. Barton, "Evidence-based estimates of the demand for radiotherapy," *Clinical Oncology (Royal College of Radiologists (Great Britain))*, vol. 27, pp. 70–76, Feb. 2015.

[7] F. Baclesse, "Comparative study of results obtained with conventional radiotherapy (200 KV) and cobalt therapy in the treatment of cancer of the larynx," *Clinical Radiology*, vol. 18, pp. 292–300, Jan. 1967.

[8] C. S. Houston and S. O. Fedoruk, "Saskatchewan's role in radiotherapy research," *Canadian Medical Association Journal*, vol. 132, pp. 854–864, Apr. 1985.

[9] B. Cho, "Intensity-modulated radiation therapy: A review with a physics perspective," *Radiation Oncology Journal*, vol. 36, pp. 1–10, Mar. 2018.

[10] C. Nutting, D. P. Dearnaley, and S. Webb, "Intensity modulated radiation therapy: A clinical review.," *British Journal of Radiology*, vol. 73, pp. 459–469, May 2000.

[11] K. Otto, "Volumetric modulated arc therapy: IMRT in a single gantry arc," *Medical Physics*, vol. 35, no. 1, pp. 310–317, 2008.

[12] M. Teoh, C. H. Clark, K. Wood, S. Whitaker, and A. Nisbet, "Volumetric modulated arc therapy: A review of current literature and clinical use in practice," *The British Journal of Radiology*, vol. 84, pp. 967–996, Nov. 2011.

[13] D. E. Heron, M. S. Huq, and A. Quinn, *General Overview of SRS and SBRT Program*. Springer Publishing Company, Aug. 2023.

[14] A. H. Ree and K. R. Redalen, "Personalized radiotherapy: Concepts, biomarkers and trial design," *The British Journal of Radiology*, vol. 88, p. 20150009, July 2015.

[15] C. Chargari, E. Deutsch, P. Blanchard, S. Gouy, H. Martelli, F. Guérin, I. Dumas, A. Bossi, P. Morice, A. N. Viswanathan, and C. Haie-Meder, "Brachytherapy: An overview for clinicians," *CA: A Cancer Journal for Clinicians*, vol. 69, no. 5, pp. 386–401, 2019.

[16] B. J. Stish, B. J. Davis, L. A. Mynderse, R. H. McLaren, C. L. Deufel, and R. Choo, "Low dose rate prostate brachytherapy," *Translational Andrology and Urology*, vol. 7, pp. 341–356, June 2018.

[17] J. J. Sohn, M. Polizzi, S.-W. Kang, W.-H. Ko, Y.-H. Cho, K.-Y. Eom, and J.-B. Chung, "Intensity Modulated High Dose Rate (HDR) Brachytherapy Using Patient Specific 3D Metal Printed Applicators: Proof of Concept," *Frontiers in Oncology*, vol. 12, p. 829529, Feb. 2022.

[18] H. Yamazaki, K. Masui, G. Suzuki, N. Aibe, D. Shimizu, T. Kimoto, K. Yamada, A. Ueno, T. Matsugasumi, Y. Yamada, T. Shiraishi, A. Fujihara, K. Okihara, K. Yoshida, and S. Nakamura, "High-dose-rate brachytherapy with external beam radiotherapy versus low-dose-rate brachytherapy with or without external beam radiotherapy for clinically localized prostate cancer," *Scientific Reports*, vol. 11, p. 6165, Mar. 2021.

[19] H. E. Barker, J. T. E. Paget, A. A. Khan, and K. J. Harrington, "The Tumour Microenvironment after Radiotherapy: Mechanisms of Resistance and Recurrence," *Nature reviews. Cancer*, vol. 15, pp. 409–425, July 2015.

[20] K. S. Rallis, T. H. L. Yau, and M. Sideris, "Chemoradiotherapy in Cancer Treatment: Rationale and Clinical Applications," *Anticancer Research*, vol. 41, pp. 1–7, Jan. 2021.

[21] Y. Wang, W. Deng, N. Li, S. Neri, A. Sharma, W. Jiang, and S. H. Lin, "Combining Immunotherapy and Radiotherapy for Cancer Treatment: Current Challenges and Future Directions," *Frontiers in Pharmacology*, vol. 9, p. 185, Mar. 2018.

[22] J. Boustani, M. Grapin, P.-A. Laurent, L. Apetoh, and C. Mirjolet, "The 6th R of Radiobiology: Reactivation of Anti-Tumor Immune Response," *Cancers*, vol. 11, p. 860, June 2019.

[23] A. N. DuRoss, M. J. Neufeld, S. Rana, C. R. Thomas, and C. Sun, "Integrating Nanomedicine into Clinical Radiotherapy Regimens," *Advanced drug delivery reviews*, vol. 144, pp. 35–56, Apr. 2019.

[24] V. T. DeVita, Jr. and E. Chu, "A History of Cancer Chemotherapy," *Cancer Research*, vol. 68, pp. 8643–8653, Oct. 2008.

[25] U. Anand, A. Dey, A. K. S. Chandel, R. Sanyal, A. Mishra, D. K. Pandey, V. De Falco, A. Upadhyay, R. Kandimalla, A. Chaudhary, J. K. Dhanjal, S. Dewanjee, J. Vallamkondu, and J. M. Pérez de la Lastra, "Cancer chemotherapy and beyond: Current status, drug candidates, associated risks and progress in targeted therapeutics," *Genes & Diseases*, vol. 10, pp. 1367–1401, Mar. 2022.

[26] J. Woo, B.-I. Moon, H. Kwon, and W. Lim, "Effect of radiotherapy sequence on long-term outcome in patients with node-positive breast cancer: A retrospective study," *Scientific Reports*, vol. 12, p. 10729, June 2022.

[27] T. A. Elbayoumi, "Nano drug-delivery Systems in Cancer Therapy: Gains, Pitfalls and Considerations in DMPK and PD," *Therapeutic Delivery*, vol. 1, pp. 215–219, Aug. 2010.

[28] D. Mintzer, "The changing role of surgery in the diagnosis and treatment of cancer," *The American Journal of Medicine*, vol. 106, pp. 81–89, Jan. 1999.

[29] "Surgery." https://www.mdanderson.org/treatment-options/surgery.html, Aug. 2024.

[30] R. Sullivan, O. I. Alatise, B. O. Anderson, R. Audisio, P. Autier, A. Aggarwal, C. Balch, M. F. Brennan, A. Dare, A. D'Cruz, A. M. M. Eggermont, K. Fleming, S. M. Gueye, L. Hagander, C. A. Herrera, H. Holmer, A. M. Ilbawi, A. Jarnheimer, J.-f. Ji, T. P.

Kingham, J. Liberman, A. J. M. Leather, J. G. Meara, S. Mukhopadhyay, S. S. Murthy, S. Omar, G. P. Parham, C. S. Pramesh, R. Riviello, D. Rodin, L. Santini, S. V. Shrikhande, M. Shrime, R. Thomas, A. T. Tsunoda, C. van de Velde, U. Veronesi, D. K. Vijaykumar, D. Watters, S. Wang, Y.-L. Wu, M. Zeiton, and A. Purushotham, "Global cancer surgery: Delivering safe, affordable, and timely cancer surgery," *The Lancet Oncology*, vol. 16, pp. 1193–1224, Sept. 2015.

[31] D. E. Green and C. T. Rubin, "Consequences of irradiation on bone and marrow phenotypes, and its relation to disruption of hematopoietic precursors," *Bone*, vol. 0, pp. 87–94, June 2014.

[32] C.-L. Zhang, T. Huang, B.-L. Wu, W.-X. He, and D. Liu, "Stem cells in cancer therapy: Opportunities and challenges," *Oncotarget*, vol. 8, pp. 75756–75766, Sept. 2017.

[33] A. D. Waldman, J. M. Fritz, and M. J. Lenardo, "A guide to cancer immunotherapy: From T cell basic science to clinical practice," *Nature Reviews Immunology*, vol. 20, pp. 651–668, Nov. 2020.

[34] M. J. Lin, J. Svensson-Arvelund, G. S. Lubitz, A. Marabelle, I. Melero, B. D. Brown, and J. D. Brody, "Cancer vaccines: The next immunotherapy frontier," *Nature Cancer*, vol. 3, pp. 911–926, Aug. 2022.

[35] C. Pucci, C. Martinelli, and G. Ciofani, "Innovative approaches for cancer treatment: Current perspectives and new challenges," *ecancermedicalscience*, vol. 13, p. 961, Sept. 2019.

[36] S. K. Das, M. E. Menezes, S. Bhatia, X.-Y. Wang, L. Emdad, D. Sarkar, and P. B. Fisher, "Gene Therapies for Cancer: Strategies, Challenges and Successes," *Journal of cellular physiology*, vol. 230, pp. 259–271, Feb. 2015.

[37] D. Stefanoudakis, N. Kathuria-Prakash, A. W. Sun, M. Abel, C. E. Drolen, C. Ashbaugh, S. Zhang, G. Hui, Y. A. Tabatabaei, Y. Zektser, L. P. Lopez, A. Pantuck, and A. Drakaki, "The Potential Revolution of Cancer Treatment with CRISPR Technology," *Cancers*, vol. 15, p. 1813, Mar. 2023.

[38] E. J. Hall and A. J. Giaccia, *Radiobiology for the Radiologist*. Philadelphia, Pa. Londo: Wolters Kluwer Lippincott Williams & Wilkins, 7th ed ed., 2012.

[39] J. Tamargo, J.-Y. Le Heuzey, and P. Mabo, "Narrow therapeutic index drugs: A clinical pharmacological consideration to flecainide," *European Journal of Clinical Pharmacology*, vol. 71, no. 5, pp. 549–567, 2015.

[40] T. Tiruye, R. David, M. O'Callaghan, L. M. FitzGerald, B. Higgs, A. A. Kahokehr, D. Roder, and K. Beckmann, "Risk of secondary malignancy following radiation therapy for prostate cancer," *Scientific Reports*, vol. 13, p. 20083, Nov. 2023.

[41] K. Wang and J. E. Tepper, "Radiation therapy-associated toxicity: Etiology, management, and prevention," *CA: A Cancer Journal for Clinicians*, vol. 71, no. 5, pp. 437–454, 2021.

[42] D. P. Dearnaley, V. S. Khoo, A. R. Norman, L. Meyer, A. Nahum, D. Tait, J. Yarnold, and A. Horwich, "Comparison of radiation side-effects of conformal and conventional radiotherapy in prostate cancer: A randomised trial," *The Lancet*, vol. 353, pp. 267–272, Jan. 1999.

[43] M. Palagudi, S. Para, N. Golla, K. C. Meduri, S. P. Duvvuri, Y. Vityala, D. C. Sajja, and U. Damineni, "Adverse Effects of Cancer Treatment in Patients With Cervical Cancer," *Cureus*, vol. 16, p. e54106, Feb. 2024.

[44] T.-A. Moo, R. Sanford, C. Dang, and M. Morrow, "Overview of Breast Cancer Therapy," *PET clinics*, vol. 13, pp. 339–354, July 2018.

[45] E. Senkus-Konefka and J. Jassem, "Complications of Breast-cancer Radiotherapy," *Clinical Oncology*, vol. 18, pp. 229–235, Apr. 2006.

[46] M. R. E. McCredie, G. S. Dite, L. Porter, J. Maskiell, G. G. Giles, K. A. Phillips, S. Redman, and J. L. Hopper, "Prevalence of self-reported arm morbidity following treatment for breast cancer in the Australian Breast Cancer Family Study," *The Breast*, vol. 10, pp. 515–522, Dec. 2001.

[47] W. Kwan, J. Jackson, L. M. Weir, C. Dingee, G. McGregor, and I. A. Olivotto, "Chronic Arm Morbidity After Curative Breast Cancer Treatment: Prevalence and Impact on Quality of Life," *Journal of Clinical Oncology*, vol. 20, pp. 4242–4248, Oct. 2002.

[48] Z. Brownlee, R. Garg, M. Listo, P. Zavitsanos, D. E. Wazer, and K. E. Huber, "Late complications of radiation therapy for breast cancer: Evolution in techniques and risk over time," *Gland Surgery*, vol. 7, pp. 371–378, Aug. 2018.

[49] B. Katta, C. Vijayakumar, S. Dutta, B. Dubashi, and V. P. Nelamangala Ramakrishnaiah, "The Incidence and Severity of Patient-Reported Side Effects of Chemotherapy in Routine Clinical Care: A Prospective Observational Study," *Cureus*, vol. 15, p. e38301, Apr. 2023.

[50] İ. Altun and A. Sonkaya, "The Most Common Side Effects Experienced by Patients Were Receiving First Cycle of Chemotherapy," *Iranian Journal of Public Health*, vol. 47, pp. 1218–1219, Aug. 2018.

[51] K. Bukowski, M. Kciuk, and R. Kontek, "Mechanisms of Multidrug Resistance in Cancer Chemotherapy," *International Journal of Molecular Sciences*, vol. 21, p. 3233, May 2020.

[52] Y. A. Luqmani, "Mechanisms of drug resistance in cancer chemotherapy," *Medical Principles and Practice: International Journal of the Kuwait University, Health Science Centre*, vol. 14 Suppl 1, pp. 35–48, 2005.

[53] B. Mansoori, A. Mohammadi, S. Davudian, S. Shirjang, and B. Baradaran, "The Different Mechanisms of Cancer Drug Resistance: A Brief Review," *Advanced Pharmaceutical Bulletin*, vol. 7, pp. 339–348, Sept. 2017.

[54] X. Wang, H. Zhang, and X. Chen, "Drug resistance and combating drug resistance in cancer," *Cancer Drug Resistance*, vol. 2, pp. 141–160, June 2019.

[55] J. Wang, N. Seebacher, H. Shi, Q. Kan, and Z. Duan, "Novel strategies to prevent the development of multidrug resistance (MDR) in cancer," *Oncotarget*, vol. 8, pp. 84559–84571, July 2017.

[56] S. Tohme, R. L. Simmons, and A. Tsung, "Surgery for Cancer: A Trigger for Metastases," *Cancer research*, vol. 77, pp. 1548–1552, Apr. 2017.

[57] D. M. Gonçalves, R. Henriques, and R. S. Costa, "Predicting Postoperative Complications in Cancer Patients: A Survey Bridging Classical and Machine Learning Contributions to Postsurgical Risk Analysis," *Cancers*, vol. 13, p. 3217, June 2021.

[58] V. Fico, G. Altieri, M. Di Grezia, V. Bianchi, M. M. Chiarello, G. Pepe, G. Tropeano, and G. Brisinda, "Surgical complications of oncological treatments: A narrative review," *World Journal of Gastrointestinal Surgery*, vol. 15, pp. 1056–1067, June 2023.

[59] P. Katta, A. Agarwal, A. M. Saifi, and A. Yadav, "Analysis of postoperative complications of oral cavity cancer: A cohort study," *Oral Oncology Reports*, vol. 6, p. 100038, June 2023.

[60] Q.-L. Xu, H. Li, Y.-J. Zhu, and G. Xu, "The treatments and postoperative complications of esophageal cancer: A review," *Journal of Cardiothoracic Surgery*, vol. 15, p. 163, July 2020.

[61] A. Kichloo, M. Albosta, D. Dahiya, J. C. Guidi, M. Aljadah, J. Singh, H. Shaka, F. Wani, A. Kumar, and M. Lekkala, "Systemic adverse effects and toxicities associated with immunotherapy: A review," *World Journal of Clinical Oncology*, vol. 12, pp. 150–163, Mar. 2021.

[62] G. G. Steel, T. McMillan, and J. Peacock, "The 5Rs of Radiobiology," *International Journal of Radiation Biology*, vol. 56, pp. 1045–1048, Jan. 1989.

[63] H. R. Withers, "The Four R's of Radiotherapy," *Advances in Radiation Biology*, vol. 5, pp. 241–271, Jan. 1975.

[64] R. Baskar, K. A. Lee, R. Yeo, and K.-W. Yeoh, "Cancer and Radiation Therapy: Current Advances and Future Directions," *International Journal of Medical Sciences*, vol. 9, pp. 193–199, Feb. 2012.

[65] T. M. Pawlik and K. Keyomarsi, "Role of cell cycle in mediating sensitivity to radiotherapy," *International Journal of Radiation Oncology*Biology*Physics*, vol. 59, pp. 928–942, July 2004.

[66] J. Yang, J.-B. Yue, J. Liu, and J.-M. Yu, "Repopulation of tumor cells during fractionated radiotherapy and detection methods (Review)," *Oncology Letters*, vol. 7, pp. 1755–1760, June 2014.

[67] C. Beckers, M. Pruschy, and I. Vetrugno, "Tumor hypoxia and radiotherapy: A major driver of resistance even for novel radiotherapy modalities," *Seminars in Cancer Biology*, vol. 98, pp. 19–30, Jan. 2024.

[68] H. K. Matthews, C. Bertoli, and R. A. M. de Bruin, "Cell cycle control in cancer," *Nature Reviews Molecular Cell Biology*, vol. 23, pp. 74–88, Jan. 2022.

[69] G. M. Cooper, "The Eukaryotic Cell Cycle," in *The Cell: A Molecular Approach. 2nd Edition*, Sinauer Associates, 2000.

[70] M. V. Blagosklonny and A. B. Pardee, "The Restriction Point of the Cell Cycle," in *Madame Curie Bioscience Database [Internet]*, Landes Bioscience, 2013.

[71] D. Ciardo, A. Goldar, and K. Marheineke, "On the Interplay of the DNA Replication Program and the Intra-S Phase Checkpoint Pathway," *Genes*, vol. 10, p. 94, Feb. 2019.

[72] M. Joiner and A. van der Kogel, eds., *Basic Clinical Radiobiology*. Boca Raton, FL: CRC Press/Taylor & Francis Group, fifth edition ed., 2018.

[73] B. Xu, S.-T. Kim, D.-S. Lim, and M. B. Kastan, "Two Molecularly Distinct G2/M Checkpoints Are Induced by Ionizing Irradiation," *Molecular and Cellular Biology*, vol. 22, pp. 1049–1059, Feb. 2002.

[74] I. Rehman, A. Gulani, M. Farooq, and B. Simpson, "Genetics, Mitosis," in *StatPearls*, Treasure Island (FL): StatPearls Publishing, 2024.

[75] M. R. Waarts, A. J. Stonestrom, Y. C. Park, and R. L. Levine, "Targeting mutations in cancer," *The Journal of Clinical Investigation*, vol. 132, p. e154943, Apr. 2022.

[76] W. J. Cannan and D. S. Pederson, "Mechanisms and Consequences of Double-strand DNA Break Formation in Chromatin," *Journal of cellular physiology*, vol. 231, pp. 3–14, Jan. 2016.

[77] Y. Wu, A. F. Pegoraro, D. A. Weitz, P. Janmey, and S. X. Sun, "The correlation between cell and nucleus size is explained by an eukaryotic cell growth model," *PLoS Computational Biology*, vol. 18, p. e1009400, Feb. 2022.

[78] S. Barnard, S. Bouffler, and K. Rothkamm, "The shape of the radiation dose response for DNA double-strand break induction and repair," *Genome Integrity*, vol. 4, p. 1, Mar. 2013.

[79] T. Lindahl, "Instability and decay of the primary structure of DNA," *Nature*, vol. 362, pp. 709–715, Apr. 1993.

[80] N. C. Bauer, A. H. Corbett, and P. W. Doetsch, "The current state of eukaryotic DNA base damage and repair," *Nucleic Acids Research*, vol. 43, pp. 10083–10101, Dec. 2015.

[81] P. Fortini and E. Dogliotti, "Base damage and single-strand break repair: Mechanisms and functional significance of short- and long-patch repair subpathways," *DNA Repair*, vol. 6, pp. 398–409, Apr. 2007.

[82] P. Langerak and P. Russell, "Regulatory networks integrating cell cycle control with DNA damage checkpoints and double-strand break repair," *Philosophical Transactions of the Royal Society B: Biological Sciences*, vol. 366, pp. 3562–3571, Dec. 2011.

[83] M. R. Lieber, "The Mechanism of Human Nonhomologous DNA End Joining *," *Journal of Biological Chemistry*, vol. 283, pp. 1–5, Jan. 2008.

[84] A. Kinner, W. Wu, C. Staudt, and G. Iliakis, "γ-H2AX in recognition and signaling of DNA double-strand breaks in the context of chromatin," *Nucleic Acids Research*, vol. 36, pp. 5678–5694, Oct. 2008.

[85] R. Ceccaldi, B. Rondinelli, and A. D. D'Andrea, "Repair Pathway Choices and Consequences at the Double-Strand Break," *Trends in cell biology*, vol. 26, pp. 52–64, Jan. 2016.

[86] L. B. Schultz, N. H. Chehab, A. Malikzay, and T. D. Halazonetis, "P53 Binding Protein 1 (53bp1) Is an Early Participant in the Cellular Response to DNA Double-Strand Breaks," *The Journal of Cell Biology*, vol. 151, pp. 1381–1390, Dec. 2000.

[87] F.-Y. Kong, J.-W. Zhang, R.-F. Li, Z.-X. Wang, W.-J. Wang, and W. Wang, "Unique Roles of Gold Nanoparticles in Drug Delivery, Targeting and Imaging Applications," *Molecules : A Journal of Synthetic Chemistry and Natural Product Chemistry*, vol. 22, p. 1445, Aug. 2017.

[88] R. Arvizo, R. Bhattacharya, and P. Mukherjee, "Gold nanoparticles: Opportunities and Challenges in Nanomedicine," *Expert opinion on drug delivery*, vol. 7, pp. 753–763, June 2010.

[89] V. Amendola, R. Pilot, M. Frasconi, O. M. Maragò, and M. A. Iatì, "Surface plasmon resonance in gold nanoparticles: A review," *Journal of Physics: Condensed Matter*, vol. 29, p. 203002, Apr. 2017.

[90] J. Montaño-Priede, M. Sanromán-Iglesias, N. Zabala, M. Grzelczak, and J. Aizpurua, "Robust Rules for Optimal Colorimetric Sensing Based on Gold Nanoparticle Aggregation," *ACS Sensors*, vol. 8, pp. 1827–1834, Apr. 2023.

[91] B. D. Chithrani, A. A. Ghazani, and W. C. W. Chan, "Determining the Size and Shape Dependence of Gold Nanoparticle Uptake into Mammalian Cells," *Nano Letters*, vol. 6, pp. 662–668, Apr. 2006.

[92] C. Cruje, C. Yang, J. Uertz, M. van Prooijen, and B. D. Chithrani, "Optimization of PEG coated nanoscale gold particles for enhanced radiation therapy," *RSC Advances*, vol. 5, pp. 101525–101532, Nov. 2015.

[93] D. B. Chithrani, "Intracellular uptake, transport, and processing of gold nanostructures," *Molecular Membrane Biology*, vol. 27, pp. 299–311, Oct. 2010.

[94] P. Talarska, M. Boruczkowski, and J. Żurawski, "Current Knowledge of Silver and Gold Nanoparticles in Laboratory Research—Application, Toxicity, Cellular Uptake," *Nanomaterials*, vol. 11, p. 2454, Sept. 2021.

[95] C. D. Walkey, J. B. Olsen, H. Guo, A. Emili, and W. C. W. Chan, "Nanoparticle Size and Surface Chemistry Determine Serum Protein Adsorption and Macrophage Uptake," *Journal of the American Chemical Society*, vol. 134, pp. 2139–2147, Feb. 2012.

[96] T. A. Larson, P. P. Joshi, and K. Sokolov, "Preventing Protein Adsorption and Macrophage Uptake of Gold Nanoparticles via a Hydrophobic Shield," *ACS nano*, vol. 6, pp. 9182–9190, Oct. 2012.

[97] J. S. Suk, Q. Xu, N. Kim, J. Hanes, and L. M. Ensign, "PEGylation as a strategy for improving nanoparticle-based drug and gene delivery," *Advanced drug delivery reviews*, vol. 99, pp. 28–51, Apr. 2016.

[98] M. Musielak, A. Boś-Liedke, O. Piwocka, K. Kowalska, R. Markiewicz, B. Szymkowiak, P. Bakun, and W. M. Suchorska, "The Role of Functionalization and Size of Gold Nanoparticles in the Response of MCF-7 Breast Cancer Cells to Ionizing Radiation Comparing 2D and 3D In Vitro Models," *Pharmaceutics*, vol. 15, p. 862, Mar. 2023.

[99] H.-Q. Yin, F.-L. Bi, and F. Gan, "Rapid synthesis of cyclic RGD conjugated gold nanoclusters for targeting and fluorescence imaging of melanoma A375 cells," *Bioconjugate Chemistry*, vol. 26, pp. 243–249, Feb. 2015.

[100] S. L. Bellis, "Advantages of RGD peptides for directing cell association with biomaterials," *Biomaterials*, vol. 32, pp. 4205–4210, June 2011.

[101] C. Yang, K. Bromma, and D. Chithrani, "Peptide Mediated In Vivo Tumor Targeting of Nanoparticles through Optimization in Single and Multilayer In Vitro Cell Models," *Cancers*, vol. 10, p. 84, Mar. 2018.

[102] D. B. Chithrani, S. Jelveh, F. Jalali, M. van Prooijen, C. Allen, R. G. Bristow, R. P. Hill, and D. A. Jaffray, "Gold Nanoparticles as Radiation Sensitizers in Cancer Therapy," *Radiation Research*, vol. 173, pp. 719–728, Feb. 2010.

[103] C. Yang, K. Bromma, W. Sung, J. Schuemann, and D. Chithrani, "Determining the Radiation Enhancement Effects of Gold Nanoparticles in Cells in a Combined Treatment with Cisplatin and Radiation at Therapeutic Megavoltage Energies," *Cancers*, vol. 10, p. 150, May 2018.

[104] K. Bromma, L. Cicon, W. Beckham, and D. B. Chithrani, "Gold nanoparticle mediated radiation response among key cell components of the tumour microenvironment for the advancement of cancer nanotechnology," *Scientific Reports*, vol. 10, p. 12096, July 2020.

[105] J. F. Hainfeld, D. N. Slatkin, and H. M. Smilowitz, "The use of gold nanoparticles to enhance radiotherapy in mice," *Physics in Medicine & Biology*, vol. 49, p. N309, Sept. 2004.

[106] J. H. Hubbell and S. M. Seltzer, "X-Ray Mass Attenuation Coefficients," *NIST*, Sept. 2009.

[107] J. D. Carter, N. N. Cheng, Y. Qu, G. D. Suarez, and T. Guo, "Nanoscale Energy Deposition by X-ray Absorbing Nanostructures," *The Journal of Physical Chemistry B*, vol. 111, pp. 11622–11625, Oct. 2007.

[108] Y. Zheng, D. J. Hunting, P. Ayotte, and L. Sanche, "Radiosensitization of DNA by Gold Nanoparticles Irradiated with High-Energy Electrons," *Radiation Research*, vol. 169, no. 1, pp. 19–27, 2008.

[109] K. Haume, S. Rosa, S. Grellet, M. A. Śmiałek, K. T. Butterworth, A. V. Solov'yov, K. M. Prise, J. Golding, and N. J. Mason, "Gold nanoparticles for cancer radiotherapy: A review," *Cancer Nanotechnology*, vol. 7, no. 1, p. 8, 2016.

[110] C. F. Thorn, C. Oshiro, S. Marsh, T. Hernandez-Boussard, H. McLeod, T. E. Klein, and R. B. Altman, "Doxorubicin pathways: Pharmacodynamics and adverse effects," *Pharmacogenetics and Genomics*, vol. 21, pp. 440–446, July 2011.

[111] P. Cortazar, R. Justice, J. Johnson, R. Sridhara, P. Keegan, and R. Pazdur, "US Food and Drug Administration Approval Overview in Metastatic Breast Cancer," *Journal of Clinical Oncology*, vol. 30, pp. 1705–1711, May 2012.

[112] S. M. Swain, F. S. Whaley, and M. S. Ewer, "Congestive heart failure in patients treated with doxorubicin: A retrospective analysis of three trials," *Cancer*, vol. 97, pp. 2869–2879, June 2003.

[113] K. Johnson-Arbor and R. Dubey, "Doxorubicin," in *StatPearls*, Treasure Island (FL): StatPearls Publishing, 2024.

[114] F. Yang, S. S. Teves, C. J. Kemp, and S. Henikoff, "Doxorubicin, DNA torsion, and chromatin dynamics," *Biochimica et biophysica acta*, vol. 1845, pp. 84–89, Jan. 2014.

[115] O. Tacar, P. Sriamornsak, and C. R. Dass, "Doxorubicin: An update on anticancer molecular action, toxicity and novel drug delivery systems," *Journal of Pharmacy and Pharmacology*, vol. 65, no. 2, pp. 157–170, 2013.

[116] R. Lüpertz, W. Wätjen, R. Kahl, and Y. Chovolou, "Dose- and time-dependent effects of doxorubicin on cytotoxicity, cell cycle and apoptotic cell death in human colon cancer cells," *Toxicology*, vol. 271, pp. 115–121, May 2010.

[117] E.-J. Park, H.-K. Kwon, Y.-M. Choi, H.-J. Shin, and S. Choi, "Doxorubicin Induces Cytotoxicity through Upregulation of pERK–Dependent ATF3," *PLOS ONE*, vol. 7, p. e44990, Sept. 2012.

[118] O. Bar-On, M. Shapira, and D. D. Hershko, "Differential effects of doxorubicin treatment on cell cycle arrest and Skp2 expression in breast cancer cells," *Anti-Cancer Drugs*, vol. 18, p. 1113, Nov. 2007.

[119] D. Balgoma, F. Kullenberg, C. Calitz, M. Kopsida, F. Heindryckx, H. Lennernäs, and M. Hedeland, "Anthracyclins Increase PUFAs: Potential Implications in ER Stress and Cell Death," *Cells*, vol. 10, p. 1163, May 2021.

[120] D. Gewirtz, "A critical evaluation of the mechanisms of action proposed for the antitumor effects of the anthracycline antibiotics adriamycin and daunorubicin," *Biochemical Pharmacology*, vol. 57, pp. 727–741, Apr. 1999.

[121] J. Turkevich, P. C. Stevenson, and J. Hillier, "A study of the nucleation and growth processes in the synthesis of colloidal gold," *Discussions of the Faraday Society*, vol. 11, pp. 55–75, Jan. 1951.

[122] J. Kimling, M. Maier, B. Okenve, V. Kotaidis, H. Ballot, and A. Plech, "Turkevich Method for Gold Nanoparticle Synthesis Revisited," *The Journal of Physical Chemistry B*, vol. 110, pp. 15700–15707, Aug. 2006.

[123] A. H. Bannister, K. Bromma, W. Sung, M. Monica, L. Cicon, P. Howard, R. L. Chow, J. Schuemann, and D. B. Chithrani, "Modulation of nanoparticle uptake, intracellular distribution, and retention with docetaxel to enhance radiotherapy," *The British Journal of Radiology*, vol. 93, p. 20190742, Feb. 2020.

[124] T. G. Mayerhöfer, S. Pahlow, and J. Popp, "The Bouguer-Beer-Lambert Law: Shining Light on the Obscure," *Chemphyschem*, vol. 21, pp. 2029–2046, Sept. 2020.

[125] W. Haiss, N. T. K. Thanh, J. Aveyard, and D. G. Fernig, "Determination of Size and Concentration of Gold Nanoparticles from UV-Vis Spectra," *Analytical Chemistry*, vol. 79, pp. 4215–4221, June 2007.

[126] C. M. Maguire, M. Rösslein, P. Wick, and A. Prina-Mello, "Characterisation of particles in solution – a perspective on light scattering and comparative technologies," *Science and Technology of Advanced Materials*, vol. 19, pp. 732–745, Oct. 2018.

[127] S. Bhattacharjee, "DLS and zeta potential – What they are and what they are not?," *Journal of Controlled Release*, vol. 235, pp. 337–351, Aug. 2016.

[128] J. Stetefeld, S. A. McKenna, and T. R. Patel, "Dynamic light scattering: A practical guide and applications in biomedical sciences," *Biophysical Reviews*, vol. 8, pp. 409–427, Oct. 2016.

[129] J. L. Sebaugh, "Guidelines for accurate EC50/IC50 estimation," *Pharmaceutical Statistics*, vol. 10, no. 2, pp. 128–134, 2011.

[130] A. Munshi, M. Hobbs, and R. E. Meyn, "Clonogenic Cell Survival Assay," in *Chemosensitivity: Volume 1 In Vitro Assays* (R. D. Blumenthal, ed.), Methods in Molecular Medicine, pp. 21–28, Totowa, NJ: Humana Press, 2005.

[131] K. Bromma, A. Alhussan, M. M. Perez, P. Howard, W. Beckham, and D. B. Chithrani, "Three-Dimensional Tumor Spheroids as a Tool for Reliable Investigation of Combined Gold Nanoparticle and Docetaxel Treatment," *Cancers*, vol. 13, p. 1465, Mar. 2021.

[132] M. Wuithschick, A. Birnbaum, S. Witte, M. Sztucki, U. Vainio, N. Pinna, K. Rademann, F. Emmerling, R. Kraehnert, and J. Polte, "Turkevich in New Robes: Key

Questions Answered for the Most Common Gold Nanoparticle Synthesis," *ACS Nano*, vol. 9, pp. 7052–7071, July 2015.

[133] A. Sani, C. Cao, and D. Cui, "Toxicity of gold nanoparticles (AuNPs): A review," *Biochemistry and Biophysics Reports*, vol. 26, p. 100991, Apr. 2021.

[134] M. K. Kauffman, M. E. Kauffman, H. Zhu, Z. Jia, and Y. R. Li, "Fluorescence-Based Assays for Measuring Doxorubicin in Biological Systems," *Reactive oxygen species (Apex, N.C.)*, vol. 2, no. 6, pp. 432–439, 2016.

[135] A. L. B. Seynhaeve, B. M. Dicheva, S. Hoving, G. A. Koning, and T. L. M. ten Hagen, "Intact Doxil is taken up intracellularly and released doxorubicin sequesters in the lysosome: Evaluated by *in vitro/in vivo* live cell imaging," *Journal of Controlled Release*, vol. 172, pp. 330–340, Nov. 2013.

[136] K. F. Maass, C. Kulkarni, M. A. Quadir, P. T. Hammond, A. M. Betts, and K. D. Wittrup, "A Flow Cytometric Clonogenic Assay Reveals the Single-Cell Potency of Doxorubicin," *Journal of Pharmaceutical Sciences*, vol. 104, no. 12, pp. 4409–4416, 2015.

[137] F. Kullenberg, O. Degerstedt, C. Calitz, N. Pavlović, D. Balgoma, J. Gråsjö, E. Sjögren, M. Hedeland, F. Heindryckx, and H. Lennernäs, "In Vitro Cell Toxicity and Intracellular Uptake of Doxorubicin Exposed as a Solution or Liposomes: Implications for Treatment of Hepatocellular Carcinoma," *Cells*, vol. 10, July 2021.

[138] O. S. Bains, A. Szeitz, J. M. Lubieniecka, G. E. Cragg, T. A. Grigliatti, K. W. Riggs, and R. E. Reid, "A Correlation between Cytotoxicity and Reductase-Mediated Metabolism in Cell Lines Treated with Doxorubicin and Daunorubicin," *Journal of Pharmacology and Experimental Therapeutics*, vol. 347, pp. 375–387, Nov. 2013.

[139] B. Sabeti, M. I. Noordin, S. Mohd, R. Hashim, A. Dahlan, and H. Akbari Javar, "Development and Characterization of Liposomal Doxorubicin Hydrochloride with Palm Oil," *BioMed Research International*, vol. 2014, p. 765426, 2014.

[140] S.-h. Wen, S.-c. Su, B.-h. Liou, C.-h. Lin, and K.-r. Lee, "Sulbactam-enhanced cytotoxicity of doxorubicin in breast cancer cells," *Cancer Cell International*, vol. 18, p. 128, Sept. 2018.

[141] Y. González-Fernández, E. Imbuluzqueta, M. Zalacain, F. Mollinedo, A. Patiño-García, and M. J. Blanco-Prieto, "Doxorubicin and edelfosine lipid nanoparticles are effective acting synergistically against drug-resistant osteosarcoma cancer cells," *Cancer Letters*, vol. 388, pp. 262–268, Mar. 2017.

[142] S. W. Rabkin and P. Sunga, "The effect of doxorubicin (adriamycin) on cytoplasmic microtubule system in cardiac cells," *Journal of Molecular and Cellular Cardiology*, vol. 19, pp. 1073–1083, Nov. 1987.

[143] K. Barlan and V. I. Gelfand, "Microtubule-Based Transport and the Distribution, Tethering, and Organization of Organelles," *Cold Spring Harbor Perspectives in Biology*, vol. 9, p. a025817, May 2017.

[144] B. D. Chithrani, J. Stewart, C. Allen, and D. A. Jaffray, "Intracellular uptake, transport, and processing of nanostructures in cancer cells," *Nanomedicine: Nanotechnology, Biology and Medicine*, vol. 5, pp. 118–127, June 2009.

[145] E. González-Gualda, A. G. Baker, L. Fruk, and D. Muñoz-Espín, "A guide to assessing cellular senescence in vitro and in vivo," *The FEBS Journal*, vol. 288, no. 1, pp. 56–80, 2021.

[146] T. Matsui, E. Nuryadi, S. Komatsu, Y. Hirota, A. Shibata, T. Oike, and T. Nakano, "Robustness of Clonogenic Assays as a Biomarker for Cancer Cell Radiosensitivity," *International Journal of Molecular Sciences*, vol. 20, p. 4148, Aug. 2019.

[147] P. L. Falcão, B. M. Motta, F. C. de Lima, C. V. Lima, and T. P. R. Campos, "Enhancement of viability of radiosensitive (PBMC) and resistant (MDA-MB-231) clones in low-dose-rate cobalt-60 radiation therapy," *Radiologia Brasileira*, vol. 48, no. 3, pp. 158–165, 2015.

[148] H. Vakifahmetoglu, M. Olsson, and B. Zhivotovsky, "Death through a tragedy: Mitotic catastrophe," *Cell Death & Differentiation*, vol. 15, pp. 1153–1162, July 2008.

[149] X. Hu and H. Zhang, "Doxorubicin-Induced Cancer Cell Senescence Shows a Time Delay Effect and Is Inhibited by Epithelial-Mesenchymal Transition (EMT)," *Medical Science Monitor : International Medical Journal of Experimental and Clinical Research*, vol. 25, pp. 3617–3623, May 2019.

[150] G. E. Neurohr, R. L. Terry, J. Lengefeld, M. Bonney, G. P. Brittingham, F. Moretto, T. P. Miettinen, L. P. Vaites, L. M. Soares, J. A. Paulo, J. W. Harper, S. Buratowski, S. Manalis, F. J. van Werven, L. J. Holt, and A. Amon, "Excessive Cell Growth Causes Cytoplasm Dilution And Contributes to Senescence," *Cell*, vol. 176, pp. 1083–1097.e18, Feb. 2019.

[151] T. Srdic-Rajic, J. F. Santibañez, K. Kanjer, N. Tisma-Miletic, M. Cavic, D. Galun, M. Jevric, N. Kardum, A. Konic-Ristic, and T. Zoranovic, "Iscador Qu inhibits doxorubicin-induced senescence of MCF7 cells," *Scientific Reports*, vol. 7, p. 3763, June 2017.

[152] A. B. Adewoye, D. Tampakis, A. Follenzi, and A. Stolzing, "Multiparameter flow cytometric detection and quantification of senescent cells in vitro," *Biogerontology*, vol. 21, no. 6, pp. 773–786, 2020.

[153] Y. Tong, W. Zhao, C. Zhou, K. Wawrowsky, and S. Melmed, "PTTG1 Attenuates Drug-Induced Cellular Senescence," *PLoS ONE*, vol. 6, p. e23754, Aug. 2011.

[154] A. H. El-Far, N. H. E. Darwish, and S. A. Mousa, "Senescent Colon and Breast Cancer Cells Induced by Doxorubicin Exhibit Enhanced Sensitivity to Curcumin, Caffeine, and Thymoquinone," *Integrative Cancer Therapies*, vol. 19, p. 1534735419901160, Jan. 2020.

[155] I. Ben-Porath and R. A. Weinberg, "When cells get stressed: An integrative view of cellular senescence," *The Journal of Clinical Investigation*, vol. 113, pp. 8–13, Jan. 2004.

[156] S. Jeyarani, N. M. Vinita, P. Puja, S. Senthamilselvi, U. Devan, A. J. Velangani, M. Biruntha, A. Pugazhendhi, and P. Kumar, "Biomimetic gold nanoparticles for its cytotoxicity and biocompatibility evidenced by fluorescence-based assays in cancer (MDA-MB-231) and non-cancerous (HEK-293) cells," *Journal of Photochemistry and Photobiology B: Biology*, vol. 202, p. 111715, Jan. 2020.

[157] S. K. Surapaneni, S. Bashir, and K. Tikoo, "Gold nanoparticles-induced cytotoxicity in triple negative breast cancer involves different epigenetic alterations depending upon the surface charge," *Scientific Reports*, vol. 8, p. 12295, Aug. 2018.

[158] R. Abu-Dahab, N. N. Mahmoud, M. Abdallah, L. Hamadneh, S. Hikmat, R. Zaza, D. Abuarqoub, and E. A. Khalil, "Cytotoxicity and Cellular Death Modality of Surface-

Decorated Gold Nanorods against a Panel of Breast Cancer Cell Lines," *ACS Omega*, vol. 6, pp. 15903–15910, June 2021.

[159] R. Coradeghini, S. Gioria, C. P. García, P. Nativo, F. Franchini, D. Gilliland, J. Ponti, and F. Rossi, "Size-dependent toxicity and cell interaction mechanisms of gold nanoparticles on mouse fibroblasts," *Toxicology Letters*, vol. 217, pp. 205–216, Mar. 2013.

[160] Y.-P. Jia, B.-Y. Ma, X.-W. Wei, and Z.-Y. Qian, "The *in vitro* and *in vivo* toxicity of gold nanoparticles," *Chinese Chemical Letters*, vol. 28, pp. 691–702, Apr. 2017.

[161] M. Kus-Liśkiewicz, P. Fickers, and I. Ben Tahar, "Biocompatibility and Cytotoxicity of Gold Nanoparticles: Recent Advances in Methodologies and Regulations," *International Journal of Molecular Sciences*, vol. 22, p. 10952, Oct. 2021.

[162] C. Carnovale, G. Bryant, R. Shukla, and V. Bansal, "Identifying Trends in Gold Nanoparticle Toxicity and Uptake: Size, Shape, Capping Ligand, and Biological Corona," *ACS Omega*, vol. 4, pp. 242–256, Jan. 2019.

[163] X.-D. Zhang, H.-Y. Wu, D. Wu, Y.-Y. Wang, J.-H. Chang, Z.-B. Zhai, A.-M. Meng, P.-X. Liu, L.-A. Zhang, and F.-Y. Fan, "Toxicologic effects of gold nanoparticles in vivo by different administration routes," *International Journal of Nanomedicine*, vol. 5, pp. 771–781, 2010.

[164] Q. Liu, X. Yin, L. R. Languino, and D. C. Altieri, "Evaluation of drug combination effect using a Bliss independence dose-response surface model," *Statistics in biopharmaceutical research*, vol. 10, no. 2, pp. 112–122, 2018.

[165] D. Duarte and N. Vale, "Evaluation of synergism in drug combinations and reference models for future orientations in oncology," *Current Research in Pharmacology and Drug Discovery*, vol. 3, p. 100110, Jan. 2022.

[166] J. Foucquier and M. Guedj, "Analysis of drug combinations: Current methodological landscape," *Pharmacology Research & Perspectives*, vol. 3, no. 3, p. e00149, 2015.

[167] A. Shibata and P. A. Jeggo, "Roles for 53BP1 in the repair of radiation-induced DNA double strand breaks," *DNA Repair*, vol. 93, p. 102915, Sept. 2020.

[168] J. Khalili Fard, S. Jafari, and M. A. Eghbal, "A Review of Molecular Mechanisms Involved in Toxicity of Nanoparticles," *Advanced Pharmaceutical Bulletin*, vol. 5, pp. 447–454, Nov. 2015.

[169] Ł. Niżnik, M. Noga, D. Kobylarz, A. Frydrych, A. Krośniak, L. Kapka-Skrzypczak, and K. Jurowski, "Gold Nanoparticles (AuNPs)—Toxicity, Safety and Green Synthesis: A Critical Review," *International Journal of Molecular Sciences*, vol. 25, p. 4057, Jan. 2024.

[170] K. Rieck, *Gold Nanoparticle Uptake in Synchronized Cell Populations and the Effect on Radiation Sensitization*. PhD thesis, University of Victoria, 2019.

[171] V. Gorgoulis, P. D. Adams, A. Alimonti, D. C. Bennett, O. Bischof, C. Bishop, J. Campisi, M. Collado, K. Evangelou, G. Ferbeyre, J. Gil, E. Hara, V. Krizhanovsky, D. Jurk, A. B. Maier, M. Narita, L. Niedernhofer, J. F. Passos, P. D. Robbins, C. A. Schmitt, J. Sedivy, K. Vougas, T. von Zglinicki, D. Zhou, M. Serrano, and M. Demaria, "Cellular Senescence: Defining a Path Forward," *Cell*, vol. 179, pp. 813–827, Oct. 2019.

[172] V. Rantanen, S. Grénman, J. Kulmala, and R. Grénman, "Comparative evaluation of cisplatin and carboplatin sensitivity in endometrial adenocarcinoma cell lines.," *British Journal of Cancer*, vol. 69, pp. 482–486, Mar. 1994.

[173] G. C. Jagetia and V. Nayak, "Effect of Doxorubicin on Cell Survival and Micronuclei Formation in HeLa Cells Exposed to Different Doses of Gamma-Radiation," *Strahlentherapie und Onkologie*, vol. 176, pp. 422–428, Aug. 2000.

[174] F. Hirschhaeuser, H. Menne, C. Dittfeld, J. West, W. Mueller-Klieser, and L. A. Kunz-Schughart, "Multicellular tumor spheroids: An underestimated tool is catching up again," *Journal of Biotechnology*, vol. 148, pp. 3–15, July 2010.

[175] K. Bromma, W. Beckham, and D. B. Chithrani, "Utilizing two-dimensional monolayer and three-dimensional spheroids to enhance radiotherapeutic potential by combining gold nanoparticles and docetaxel," *Cancer Nanotechnology*, vol. 14, p. 80, Oct. 2023.

[176] A. Alhussan, N. Palmerley, J. Smazynski, J. Karasinska, D. J. Renouf, D. F. Schaeffer, W. Beckham, A. S. Alexander, and D. B. Chithrani, "Potential of Gold Nanoparticle in Current Radiotherapy Using a Co-Culture Model of Cancer Cells and Cancer Associated Fibroblast Cells," *Cancers*, vol. 14, p. 3586, July 2022.

[177] A. A. Fitzgerald, E. Li, and L. M. Weiner, "3D Culture Systems for Exploring Cancer Immunology," *Cancers*, vol. 13, p. 56, Dec. 2020.

[178] G. Al-Hity, F. Yang, E. Campillo-Funollet, A. E. Greenstein, H. Hunt, M. Mampay, H. Intabli, M. Falcinelli, A. Madzvamuse, C. Venkataraman, and M. S. Flint, "An integrated framework for quantifying immune-tumour interactions in a 3D co-culture model," *Communications Biology*, vol. 4, pp. 1–12, June 2021.

[179] Y. Jia, Y. Jiang, Y. He, W. Zhang, J. Zou, K. T. Magar, H. Boucetta, C. Teng, and W. He, "Approved Nanomedicine against Diseases," *Pharmaceutics*, vol. 15, p. 774, Feb. 2023.

[180] P. Bigini, M. Gobbi, M. Bonati, A. Clavenna, M. Zucchetti, S. Garattini, and G. Pasut, "The role and impact of polyethylene glycol on anaphylactic reactions to COVID-19 nano-vaccines," *Nature Nanotechnology*, vol. 16, pp. 1169–1171, Nov. 2021.

[181] N. Zhao, M. C. Woodle, and A. J. Mixson, "Advances in delivery systems for doxorubicin," *Journal of nanomedicine & nanotechnology*, vol. 9, no. 5, p. 519, 2018.

[182] X.-R. Li, X.-H. Cheng, G.-N. Zhang, X.-X. Wang, and J.-M. Huang, "Cardiac safety analysis of first-line chemotherapy drug pegylated liposomal doxorubicin in ovarian cancer," *Journal of Ovarian Research*, vol. 15, p. 96, Aug. 2022.

[183] G. Batist, J. Barton, P. Chaikin, C. Swenson, and L. Welles, "Myocet (liposome-encapsulated doxorubicin citrate): A new approach in breast cancer therapy," *Expert Opinion on Pharmacotherapy*, vol. 3, pp. 1739–1751, Dec. 2002.

[184] Y. C. Barenholz, "Doxil® — The first FDA-approved nano-drug: Lessons learned," *Journal of Controlled Release*, vol. 160, pp. 117–134, June 2012.

[185] R. Solomon and A. A. Gabizon, "Clinical Pharmacology of Liposomal Anthracyclines: Focus on Pegylated Liposomal Doxorubicin," *Clinical Lymphoma and Myeloma*, vol. 8, pp. 21–32, Feb. 2008.

[186] A. T. Perez, G. H. Domenech, C. Frankel, and C. L. Vogel, "Pegylated Liposomal Doxorubicin (Doxil®) for Metastatic Breast Cancer: The Cancer Research Network, Inc., Experience," *Cancer Investigation*, vol. 20, pp. 22–29, Jan. 2002.

[187] S. Nagpal, S. Braner, H. Modh, A. X. X. Tan, M.-P. Mast, K. Chichakly, V. Albrecht, and M. G. Wacker, "A physiologically-based nanocarrier biopharmaceutics model to reverse-engineer the in vivo drug release," *European Journal of Pharmaceutics and Biopharmaceutics*, vol. 153, pp. 257–272, Aug. 2020.

[188] Y. Zhao, D. Y. Alakhova, J. O. Kim, T. K. Bronich, and A. V. Kabanov, "A simple way to enhance Doxil® therapy: Drug release from liposomes at the tumor site by amphiphilic block copolymer," *Journal of Controlled Release*, vol. 168, pp. 61–69, May 2013.

[189] L. Silverman and Y. Barenholz, "In vitro experiments showing enhanced release of doxorubicin from Doxil® in the presence of ammonia may explain drug release at tumor site," *Nanomedicine: Nanotechnology, Biology and Medicine*, vol. 11, pp. 1841–1850, Oct. 2015.

[190] X. Hu, M. Dong, X. Liang, Z. Liu, and Q. Li, "Reactive Oxygen Species-Mediated Inflammation and Apoptosis in Hand-Foot Syndrome Induced by PEGylated Liposomal Doxorubicin," *International Journal of Nanomedicine*, vol. 16, pp. 471–480, Jan. 2021.

[191] M. I. Koukourakis, S. Koukouraki, A. Giatromanolaki, S. C. Archimandritis, J. Skarlatos, K. Beroukas, J. G. Bizakis, G. Retalis, N. Karkavitsas, and E. S. Helidonis, "Liposomal doxorubicin and conventionally fractionated radiotherapy in the treatment of locally advanced non-small-cell lung cancer and head and neck cancer," *Journal of Clinical Oncology: Official Journal of the American Society of Clinical Oncology*, vol. 17, pp. 3512–3521, Nov. 1999.

[192] E. Hagtvet, K. Røe, and D. R. Olsen, "Liposomal doxorubicin improves radiotherapy response in hypoxic prostate cancer xenografts," *Radiation Oncology*, vol. 6, p. 135, Oct. 2011.

[193] S. C. Brüningk, I. Rivens, C. Box, U. Oelfke, and G. ter Haar, "3D tumour spheroids for the prediction of the effects of radiation and hyperthermia treatments," *Scientific Reports*, vol. 10, p. 1653, Feb. 2020.

[194] D. J. Lim, X.-L. Liu, D. M. Sutkowski, E. J. Braun, C. Lee, and J. M. Kozlowski, "Growth of an androgen-sensitive human prostate cancer cell line, LNCaP, in nude mice," *The Prostate*, vol. 22, no. 2, pp. 109–118, 1993.

[195] M. A. Castanares, B. T. Copeland, W. H. Chowdhury, M. M. Liu, R. Rodriguez, M. G. Pomper, S. E. Lupold, and C. A. Foss, "Characterization of a Novel Metastatic Prostate Cancer Cell Line of LNCaP Origin," *The Prostate*, vol. 76, pp. 215–225, Feb. 2016.

[196] S. Ohya, J. Kajikuri, K. Endo, H. Kito, and M. Matsui, "KCa1.1 K+ Channel Inhibition Overcomes Resistance to Antiandrogens and Doxorubicin in a Human Prostate Cancer LNCaP Spheroid Model," *International Journal of Molecular Sciences*, vol. 22, p. 13553, Dec. 2021.

[197] E. J. Orzechowska, A. Girstun, K. Staron, and J. Trzcinska-Danielewicz, "Synergy of BID with doxorubicin in the killing of cancer cells," *Oncology Reports*, vol. 33, pp. 2143–2150, May 2015.

[198] W. H. Chappell, B. D. Lehmann, D. M. Terrian, S. L. Abrams, L. S. Steelman, and J. A. McCubrey, "P53 expression controls prostate cancer sensitivity to chemotherapy and the MDM2 inhibitor Nutlin-3," *Cell Cycle*, vol. 11, pp. 4579–4588, Dec. 2012.

Appendix A

Treatment of MDA-MB-231 Cells With Liposomal Doxorubicin

A.1 Nanomedicine Formulations of Doxorubicin

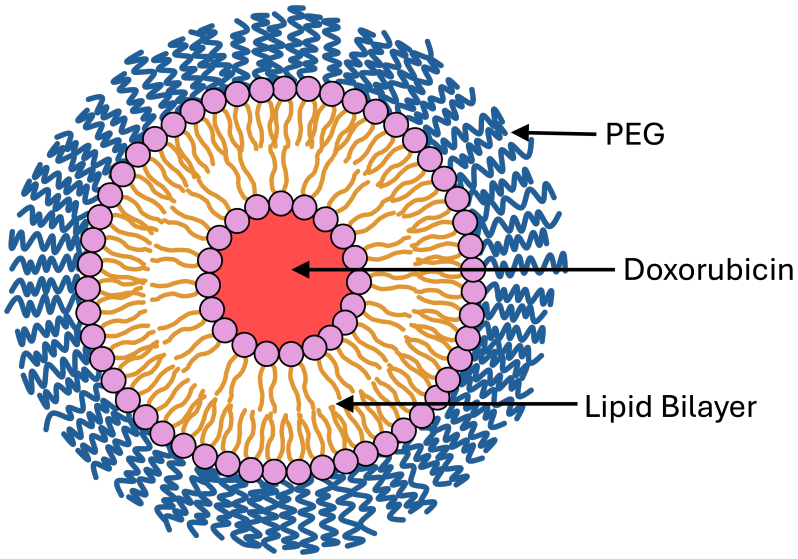

Figure A.1: A diagram illustrating the structure of PEGylated liposomal doxorubicin. Doxorubicin is enclosed in an aqueous core surrounded by a lipid bilayer forming a spherical liposome, and PEG molecules are attached to the surface.

In chemotherapy, nanoparticles serve as effective platforms for delivering chemotherapeutic agents, overcoming biological barriers and enhancing drug accumulation at the tumour site. Many nanoparticle based drug delivery systems are already in clinical use, [179]. Additionally, nanomedicine and lipid nanoparticles were a key component of the success of the COVID-19 vaccines [180].

Liposomal doxorubicin (LNP-DOX) encapsulates the drug in an aqueous core inside of li-

posomes, which preferentially accumulate in tumour tissue due to the enhanced permeability and retention (EPR) effect [181]. This reduces the exposure of normal tissues to DOX and lowers the risk of cardiotoxicity [182]. Myocet™ (Elan Pharmaceuticals) is an unPEGylated liposome-encapsulated doxorubicin citrate which has shown to be less cardiotoxic and have an improved therapeutic index versus free DOX [183].

Doxil is a formulation of DOX encapsulated in PEGylated liposomes. It was the first nanomedicine drug to be approved by the FDA in 1995 [184]. The liposomal encapsulation allows for controlled release of doxorubicin at the tumour site, reducing systemic exposure and minimizing side effects such as cardiotoxicity. Clinical trials have demonstrated Doxil's efficacy in various cancers, including recurrent ovarian cancer, metastatic breast cancer, and multiple myeloma [185]. In metastatic breast cancer, it offers equivalent efficacy with reduced cardiotoxicity compared to free doxorubicin [186]. For Doxil, the mean residence time of the doxorubicin inside the liposome was found to be 128 hours [187], which gives the liposomes more time to accumulate at the target site before releasing the drug. To further localize the treatment, studies have examined mechanisms for triggering release at the tumour site [188, 189].

One side effect of liposomal doxorubicin that does not occur with free doxorubicin is hand-foot syndrome, where the palms and soles of the feet become red, swollen, and blistered [190].

A.2 Materials and Methods

Clinical grade PEGylated liposomal doxorubicin hydrochloride (LNP-DOX; Taro Pharmaceutical Industries) was kept refrigerated at 4°C and diluted in PBS and cell media as needed for dosing. Cells were dosed for 48 hours with LNP-DOX at the IC50 dose as determined for a 48 hour incubation of DOX (144.4 nM for MDA-MB-231). Experiments were performed as described in Section 2 with modifications to the plate layouts as shown in Figure A.2.

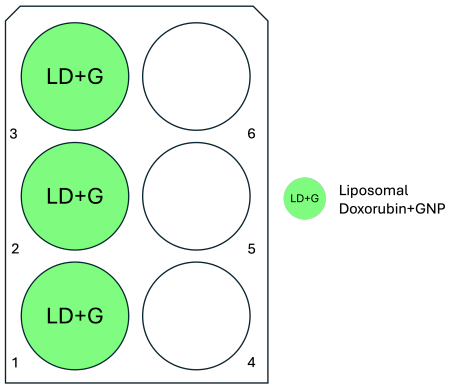

(a) 6-well plate layout used for cellular uptake of GNPs with LNP-DOX.

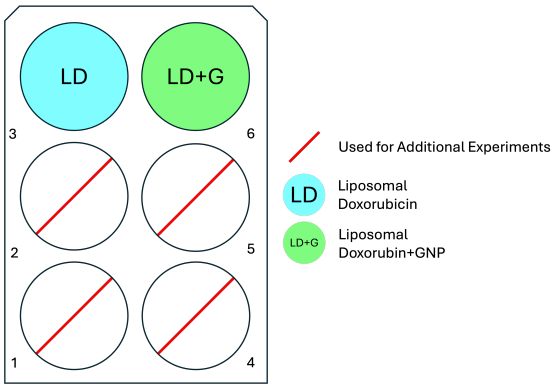

(b) 6-well plate layout used for cell cycle assay, double strand break assay, and for the dosing and irradiation steps of the clonogenic assay.

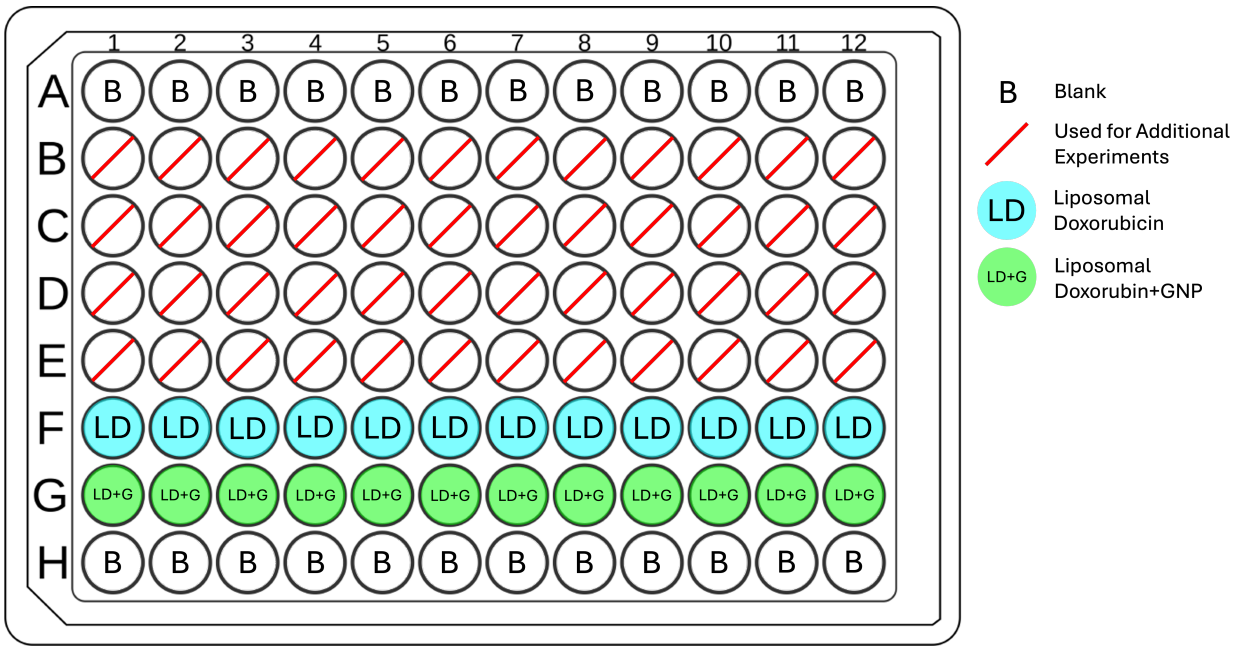

(c) 96-well plate layout used for cellular proliferation assay.

Figure A.2: Modifications to cell culture plate layouts used for LNP-DOX experiments.

A.3 Results

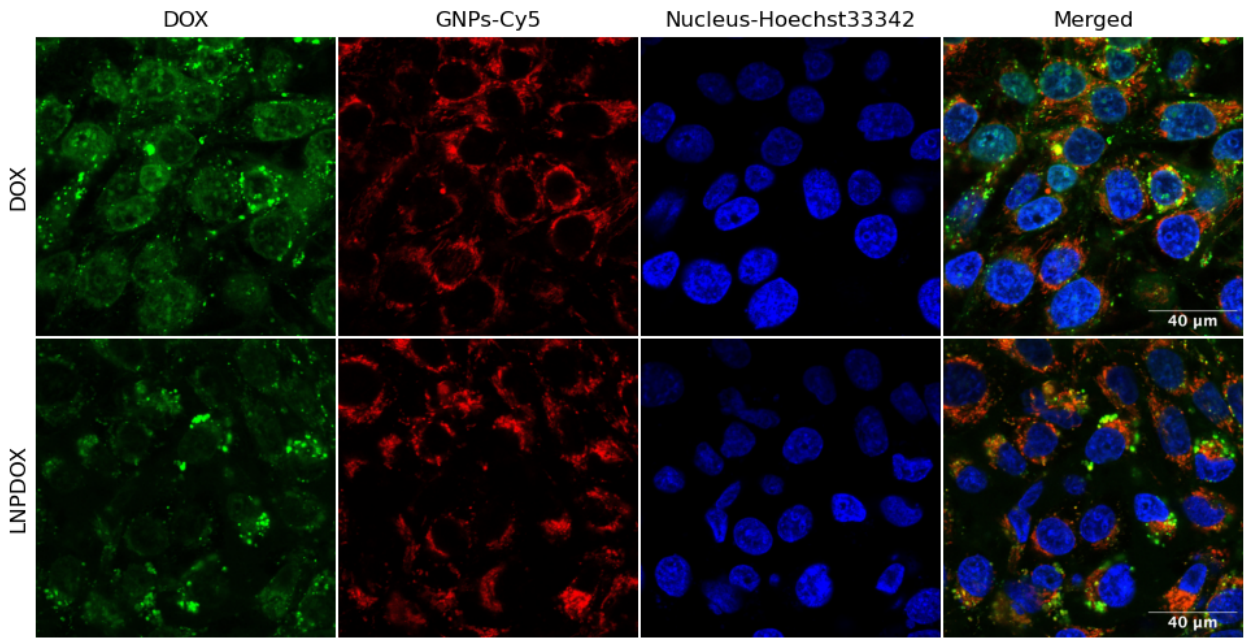

Figure A.3: Live cell confocal imaging of MDA-MB-231 cells containing either DOX or LNP-DOX (green channel) and GNPs functionalized with PEG-Cy5 (red channel). Cell nuclei are stained with NucBlue (Hoechst33342, blue channel).

In Figure A.3 it can be seen that the GNPs are found throughout the cell but tend to cluster near the nucleus. DOX and LNP-DOX are both seen distributed throughout the cell, with some brighter spots that are likely lysosomes which have sequestered the drug [135]. These images were taken right at the end of the 48 hour drug incubation period, and the DOX treated cells appear larger than the LNP-DOX cells. This size difference is much more significant in Figure A.9, in which the cells were incubated in fresh media for an additional 24 hours after treatment.

Samples incubated with LNP-DOX contained on average $(0.75\pm0.04)\times10^6$ GNPs per cell. This is consistent with having the same amount of uptake as the control cells ($p>0.05$). The LNP-DOX having no effect on GNP uptake when the DOX had a large effect is an indicator that the liposomes are not delivering as much doxorubicin to the cells as they are receiving when dosed with the free DOX. There are two contributing factors to this. Firstly, the LNP-DOX is PEGylated, and while PEG is useful in vivo as it prolongs circulation time in the body [186], it has been shown to reduce uptake of nanoparticles in vitro [92]. Secondly, once in the cell, the liposomes must release the doxorubicin for it to be effective. The release process is still not fully understood, and it is likely that some of the LNP-DOX is

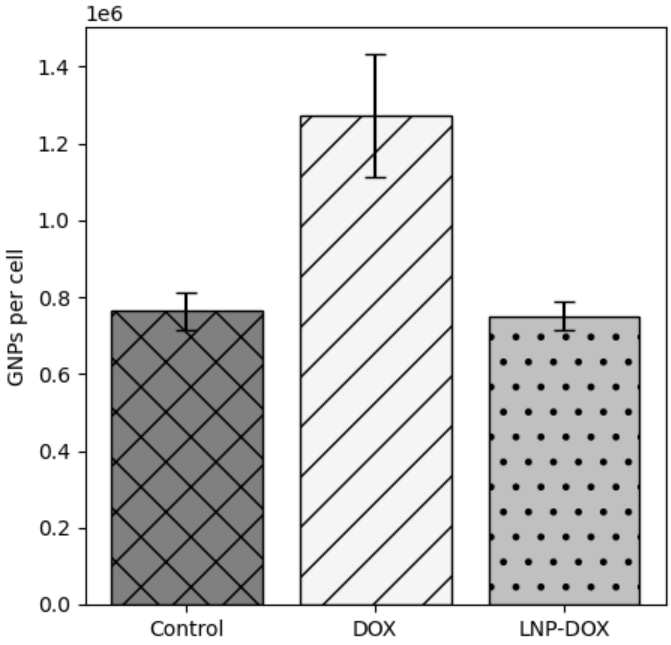

Figure A.4: Gold nanoparticle uptake by MDA-MB-231 cells treated with DOX or LNP-DOX. The experiment was performed in triplicate and the error bars represent standard error between wells.

being expelled from the cell before the doxorubicin can be released. Seynhaeve et al. found that liposomal doxorubicin had reduced bioavailability when compared to free doxorubicin, and only 0.4% of doxorubicin administered as LNP-DOX entered the nucleus [135]. This is consistent with the live cell images in Figure A.3 where there is significantly less doxorubicin fluorescence in the nuclei of the LNP-DOX sample than there is in the DOX sample.

In the flow cytometry results (Figure A.5), the LNP-DOX and LNP-DOX/GNP samples had no significant differences from the control and GNP samples at either time point, indicating that the LNP-DOX was not effective. In the cellular proliferation results (Figure A.6) the LNP-DOX and LNP-DOX/GNP samples do not show a significant difference from the control and GNP samples, respectively, at either 2 or 5 Gy of radiation. This supports the conclusion that the LNP-DOX was not effective at the given dose, as discussed.

In Figure A.7, the LNP-DOX samples did not have a significant difference in clonogenic growth from the control samples at 0 Gy ($p>0.05$). At 2 Gy, the LNP-DOX surviving fraction was (48±7)% lower than the 2 Gy control cells ($p<0.05$). At 5 Gy, the difference between control and LNP-DOX was (71±13)% ($p<0.05$). While these results indicate that the LNP-

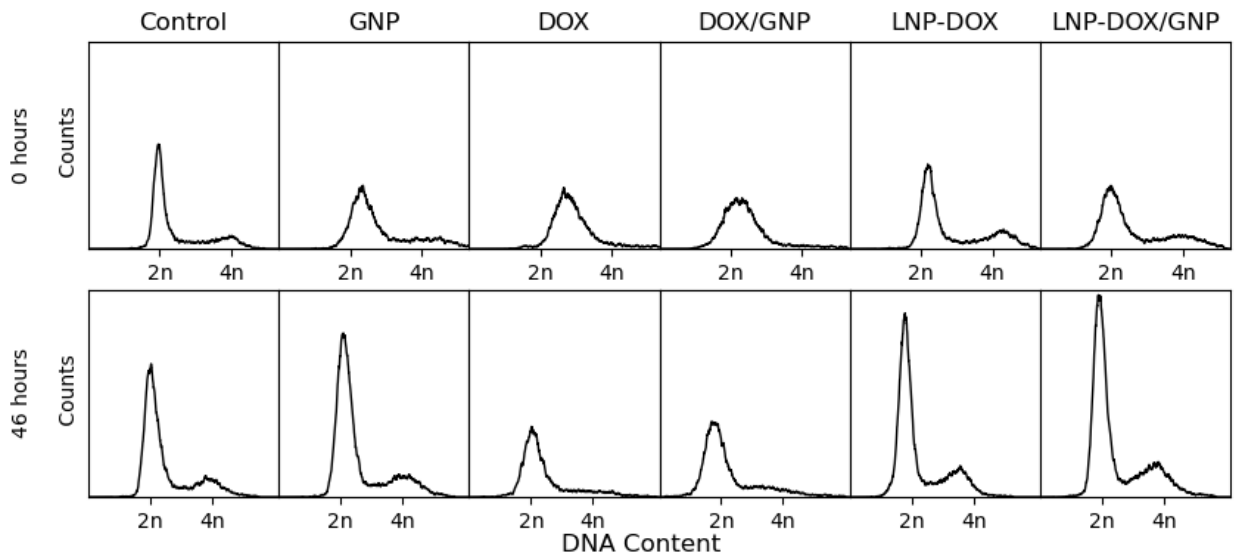

Figure A.5: Flow cytometry results for MDA-MB-231 cells incubated with DOX or LNP-DOX, and GNPs. Cells were unirradiated, and data was collected at two time points after removing the treated media, 0 hours and 46 hours. DNA content is based on the amount of propidium iodide measured by flow cytometry. 2n and 4n DNA content was labelled based on the locations of the peaks in the 0hr and 46hr control samples. 2n DNA indicates the G1 phase, and 4n indicates the G2/M phase.

DOX was having some effect in conjunction with the radiation, a Bliss independence test [164] was conducted to evaluate the synergy of the two treatments (see Section 3.2.4). In this case, the effect used was the clonogenic growth that was inhibited by LNP-DOX or the radiation. At 2 Gy, the combination index for LNP-DOX and radiation was 0.86±0.09, indicating there was a synergistic effect. At 5 Gy, the combination index was 0.99±0.07, indicating the effect was independent. Additionally, the LNP-DOX/GNP surviving fraction was 37% lower ($p<0.005$) than the LNP-DOX sample at 0 Gy. This trend did not continue through the irradiated LNP-DOX samples.

In Figure A.8 at 0 Gy, the LNP-DOX incubated cells exhibited twice as many foci per cell than the control and GNP samples ($p<0.05$). At 2 Gy, there was no significant difference in the number of foci between the samples. The increase in DNA damage with the LNP-DOX at 0 Gy indicates that sufficient doxorubicin is being released from within the liposomes to have some effect, albeit a weak one, which agrees with the clonogenic assay results in Figure A.7.

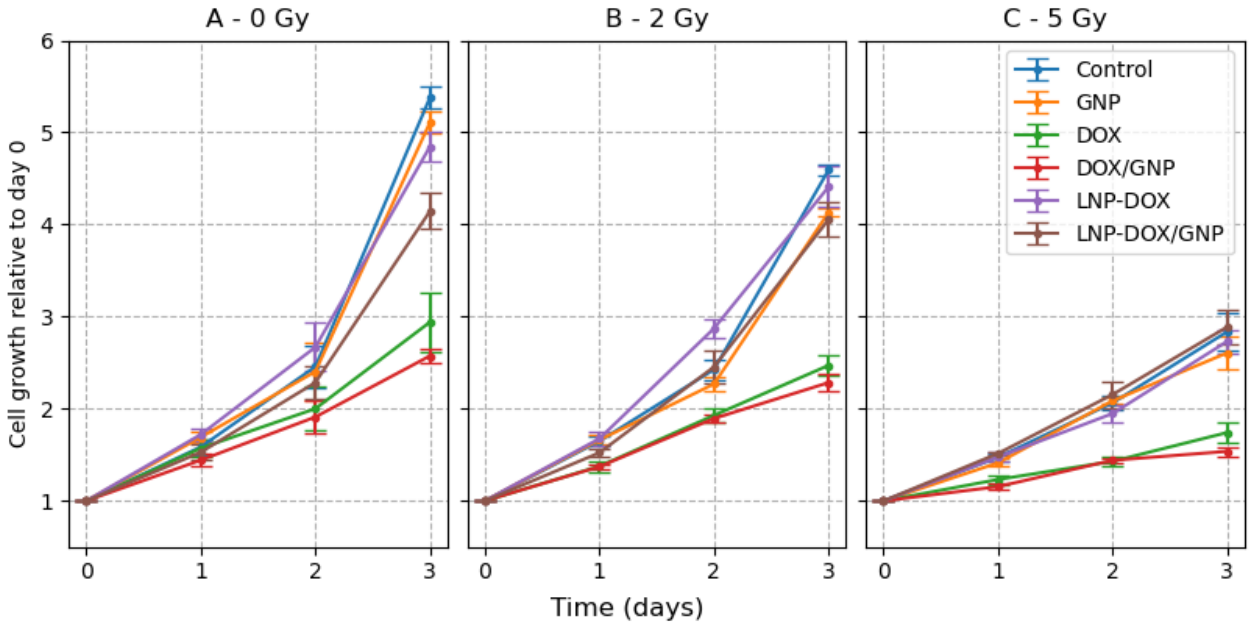

Figure A.6: Cellular proliferation of DOX, LNP-DOX, GNP, and radiotherapy treated MDA-MB-231 cells over three days. Cell growth is relative to the first set of measurements. The experiment was performed in triplicate with 6 wells per condition per plate per reading, for a total of 18 wells for each data point. Error bars represent the standard error.

A.4 Conclusions

Dosed at the same concentration as the free DOX, the cells showed a lack of response to LNP-DOX in the uptake, cell cycle, and proliferation results. It was not until the clonogenic and DNA double strand break assays that it had any effect, and in those it was slight. This is likely due to a combination of factors. First, the LNP-DOX is PEGylated, which reduces the uptake of the liposomes into the cells. Second, the liposomes can be slow to release the doxorubicin into the cell once they have been internalized, and they generally have reduced bioavailability. The clonogenic and DSB assay do show some toxicity from the LNP-DOX, and the clonogenic results show that it is synergistic with the radiation at 2 Gy. However this did not apply at 5 Gy, indicating the radiation was the dominant effect. The fact that a therapeutic benefit was seen at 2 Gy indicates future studies with higher doses of LNP-DOX may yield better results. It would be worthwhile to investigate this further as liposomal doxorubicin is already in clinical use in the form of Doxil or Caelyx, and a synergistic effect with radiation could be exploited for improved treatment outcomes. Liposomal doxorubicin had no significant effect in vitro at the given dose, however it did show evidence of radiosensitization which merits further investigation.

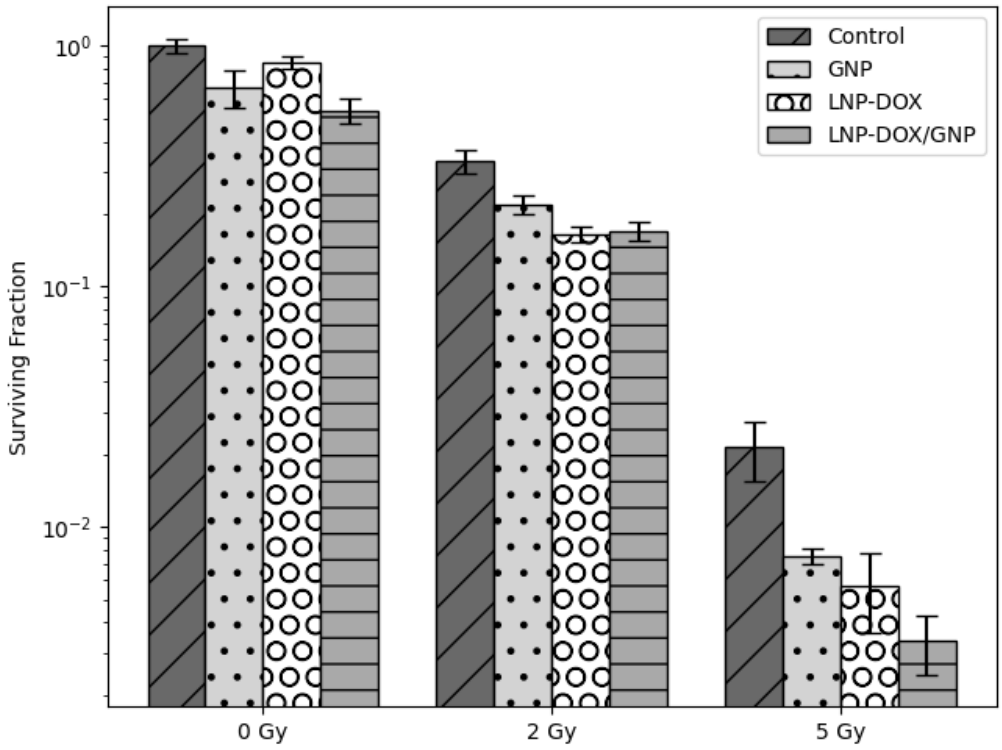

Figure A.7: Clonogenic assay results for MDA-MB-231 cells treated with LNP-DOX and/or GNPs. Error bars represent the standard error between all plates for a given condition, with at least three colony forming plates per condition.

A.5 Future Work

One study has already been conducted to assess the safety of concomitant LNP-DOX and radiotherapy, and found that it was feasible and has potential for further study [191]. A more recent study administered LNP-DOX in the form of Caelyx concomitantly with radiotherapy using a mouse model and found it to have a favourable therapeutic effect [192]. Future in vitro work should use a higher LNP-DOX than was used here, in order to better demonstrate any effect it may be having. Additionally, experiments could be performed using spheroids, which are increasingly being used for in vitro experiments to asses radiotherapy techniques [193]. They are better able to mimic the tumour microenvironment and may provide more accurate estimations of how the tumour will respond in vivo. However, given that LNP-DOX is already being used in a clinical setting, it may be advantageous to proceed directly to in vivo studies of combined chemoradiotherapy using LNP-DOX.

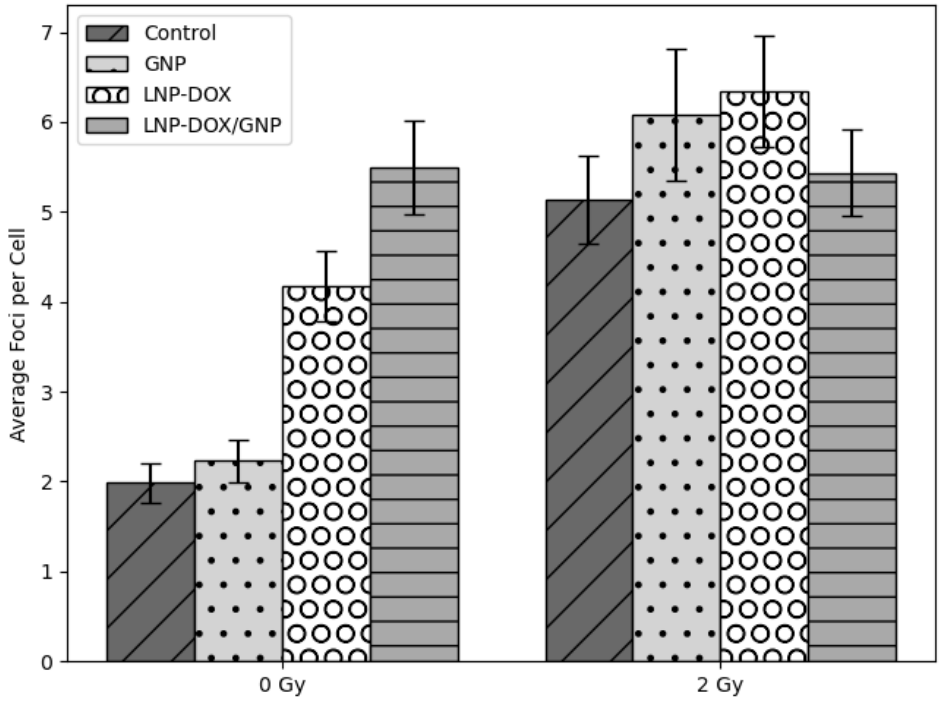

Figure A.8: Number of DNA repair foci, γH2AX and 53PB1, counted in MDA-MB-231 cells treated with LNP-DOX and/or GNPs. Multiple images were taken so that at least fifty unique nuclei were counted for each sample. Error bars represent the standard error amongst all of the nuclei counted for a sample.

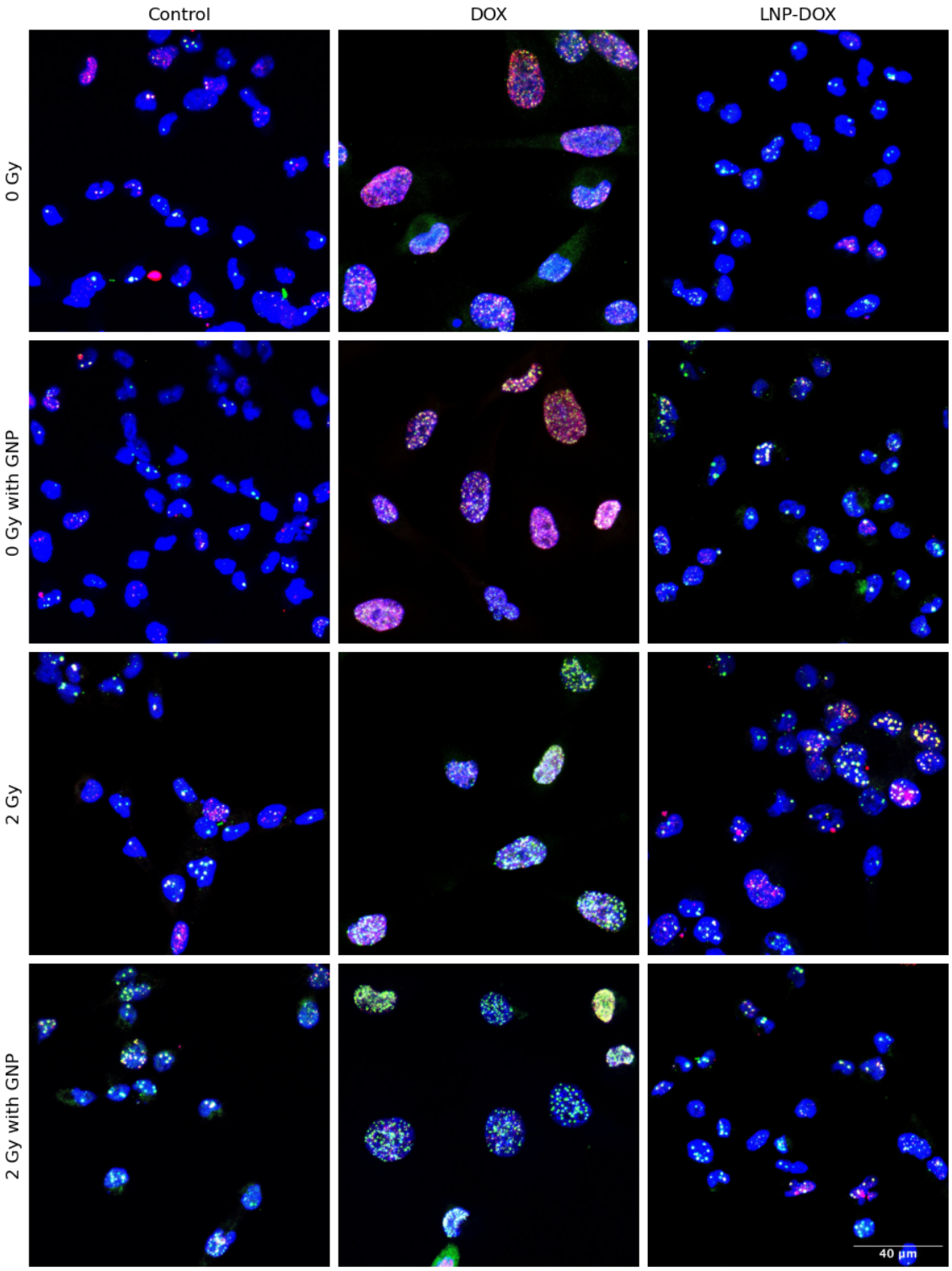

Figure A.9: Confocal imaging of DNA damage indicators in MDA-MB-231 cells containing either DOX or LNP-DOX, and GNPs. Blue is Hoechst 33342 used to stain the cell nucleus. Red is Alexa Fluor 647, used to label γH2AX. Green is Alex Fluor 488, used to label 53BP1.

Appendix B

Results for Prostate Cancer Cell Line LNCaP

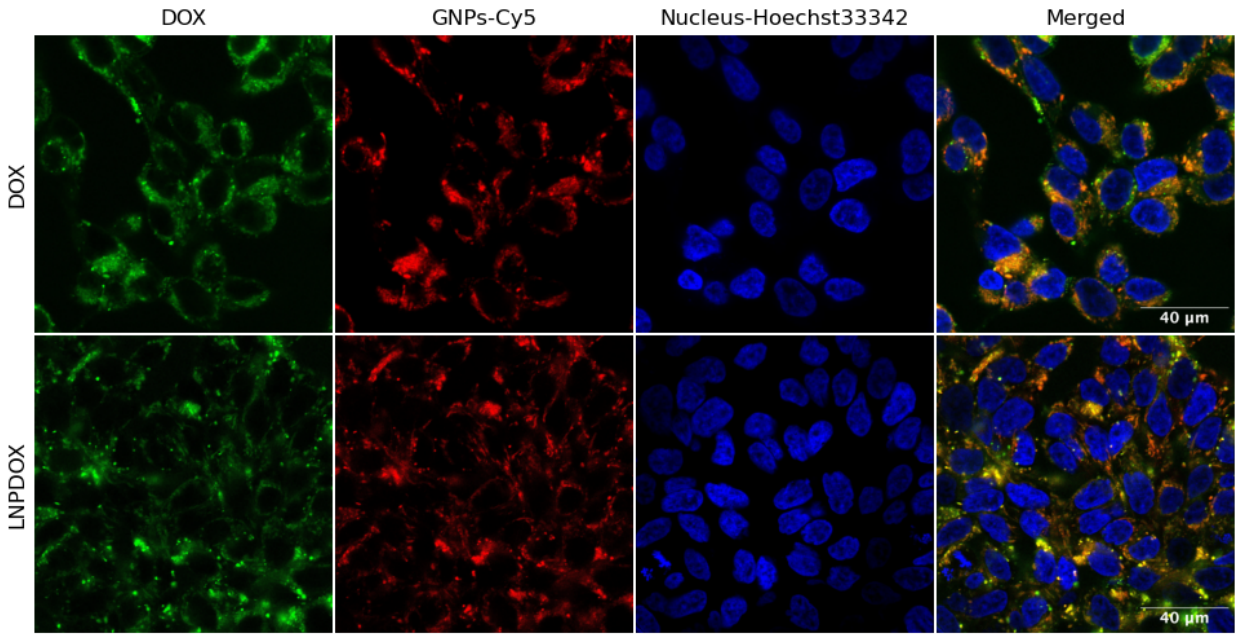

Figure B.1: Live cell confocal imaging of LNCaP cells containing either DOX or LNP-DOX (green channel) and GNPs functionalized with PEG-Cy5 (red channel). Cell nuclei are stained with NucBlue (Hoechst33342, blue channel). LNCaP is an androgen-sensitive cell line derived from cells taken from the lymph node of a patient with prostate cancer [194, 195]. It has been the subject of several studies examining how different compounds affect its sensitivity to DOX [196, 197]. As none of the treatments being examined showed an effect on the LNCaP cells in the initial experiments, cell cycle analysis, DNA double strand break assay, and clonogenic assay were not performed.

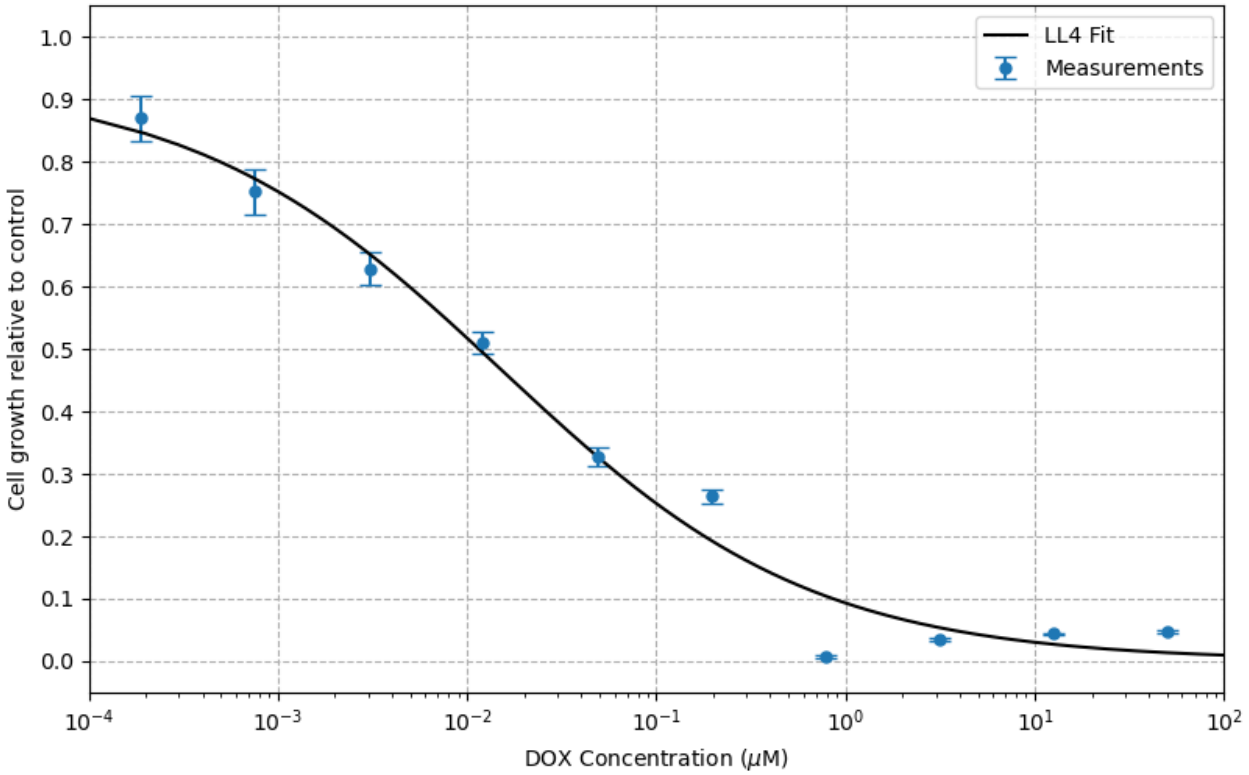

Figure B.2: Relative cell growth versus DOX concentration used to determine the IC50 of doxorubicin for LNCaP cells after 48 hour drug incubation time. The experiment was performed in triplicate and the error bars represent the standard error in the mean between the three plates. The IC50 of doxorubicin for LNCaP cells was determined to be 11.5 nM. This is the concentration at which DOX and LNP-DOX were dosed for all other experiments using LNCaP cells, and is consistent with other IC50 experiments measuring the sensitivity of LNCaP to DOX [198].

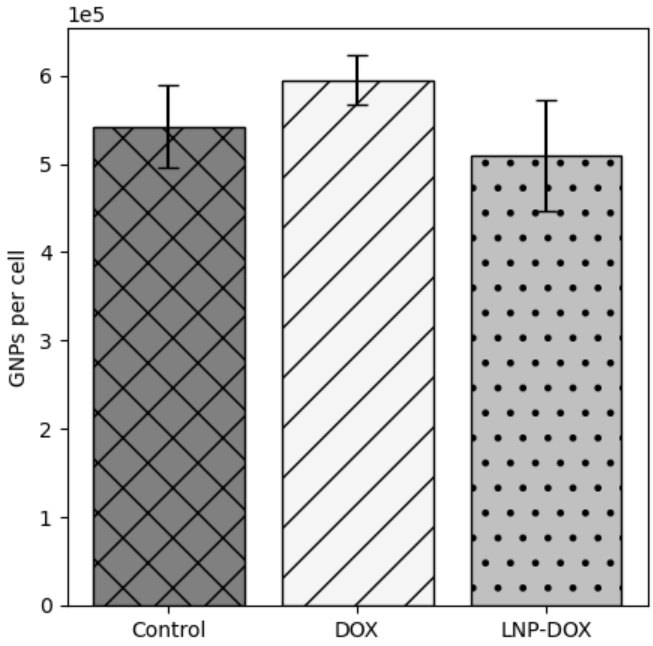

Figure B.3: Gold nanoparticle uptake by LNCaP cells. The experiment was performed in triplicate and the error bars represent standard error between wells. There was no significant difference in the amount of GNPs taken up by LNCaP in the presence of DOX or LNP-DOX.

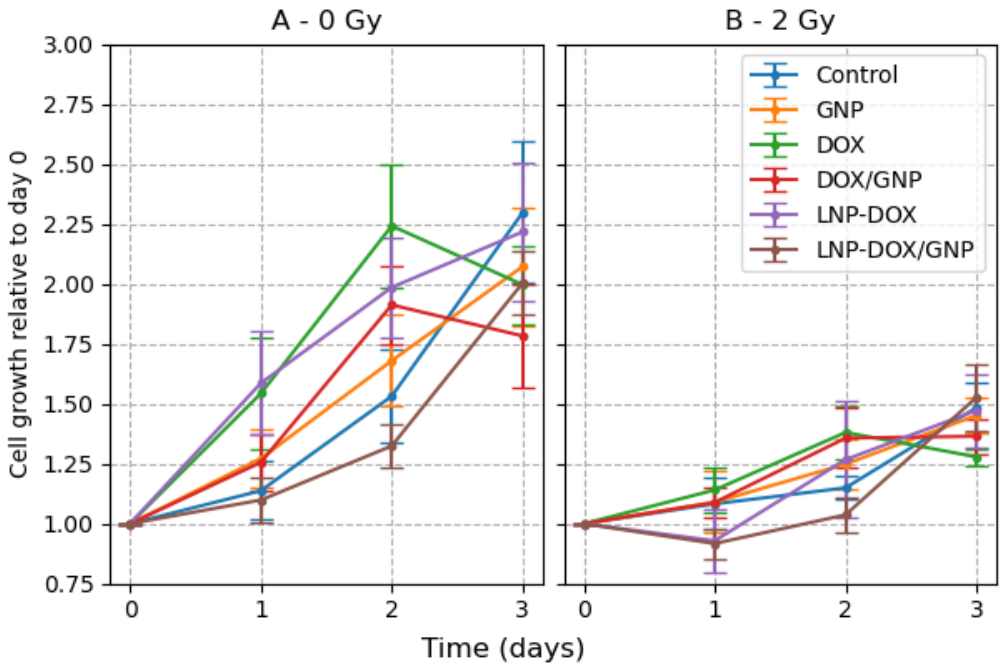

Figure B.4: Cellular proliferation of LNCaP cells over three days. Cell growth is relative to the first set of measurements. The experiment was performed in triplicate with 6 wells per condition per plate per reading, for a total of 18 wells for each data point. Error bars represent the standard error. While the 2 Gy samples showed growth inhibition as expected, neither DOX, nor LNP-DOX, nor GNPs made a significant difference in the amount of growth when compared to the control at either radiation dose.

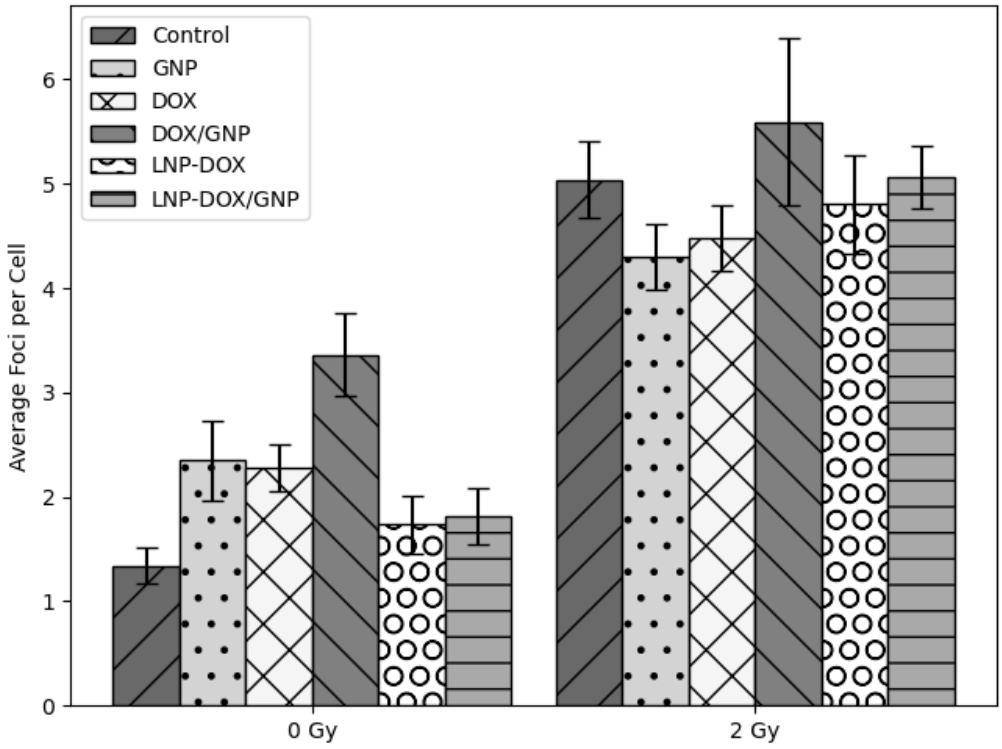

Figure B.5: Number of DNA repair foci, γH2AX and 53PB1, counted in LNCaP cells. Multiple images were taken so that at least fifty unique nuclei were counted for each sample. Error bars represent the standard error amongst all of the nuclei counted for a sample. The combination of DOX/GNPs showed higher average counts of foci in the 0 Gy samples, but no other significant differences were seen. This trend did not continue in the 2 Gy irradiated samples where there was no significant difference in foci counts between any of the treatments.

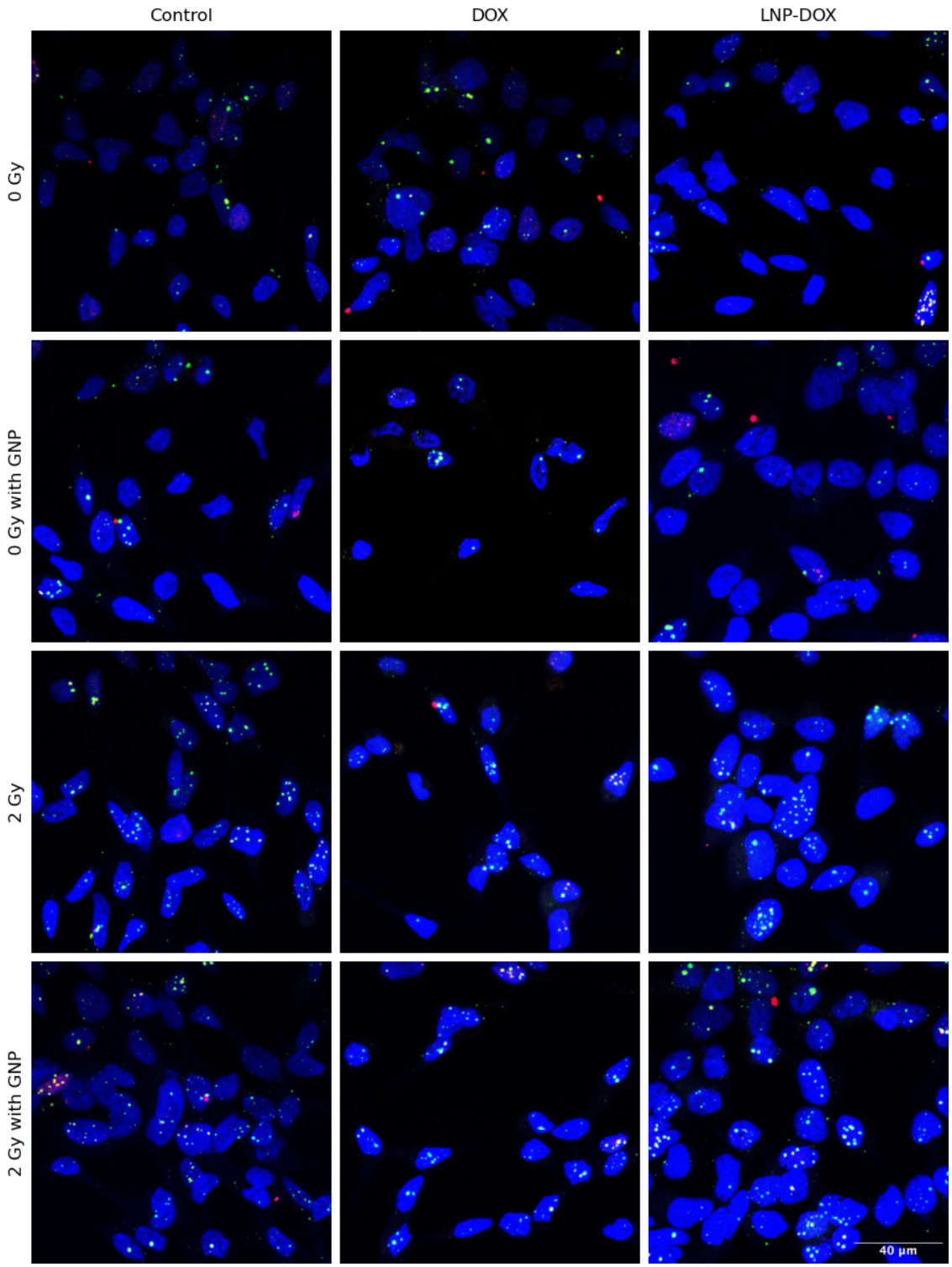

Figure B.6: Confocal imaging of DNA damage indicators in LNCaP cells containing either DOX or LNP-DOX and GNPs. Blue is Hoechst 33342 used to stain the cell nucleus. Red is Alexa Fluor 647, used to label γH2AX. Green is Alex Fluor 488, used to label 53BP1. Unlike in the MDA-MB-231 cells, no changes in morphology were observed.